Material Science and Technology Division

Propulsion Materials Program
Quarterly Progress Report for
January through March 2012

Allen Haynes
Technical Project Manager

Prepared for
U.S. Department of Energy
Assistant Secretary for Energy Efficiency and Renewable Energy
Office of Vehicle Technologies Program
VT 05 04 000

Prepared by the
OAK RIDGE NATIONAL LABORATORY
Oak Ridge, Tennessee 37831-6066
Managed by
UT-Battelle, LLC
for the Department of Energy
Under contract DE-AC05-00OR22725

CONTENTS

Project 18516 – Materials for Hybrid and Electric Drive Systems

Agreement 19201 – MBD Non-Rare Earth Magnetic Materials *(ORNL)*

Agreement 23278 - Low-Cost Direct Bonded Aluminum (DBA) Substrates *(ORNL)*

Agreement 23279 - Improved Organics for Power Electronics and Electric Motors *(ORNL)*

Project 18518 – Materials for High Efficiency Engines

Agreement 19202 – Titanium Friction and Wear *(ORNL)*

Agreement 23284 – Friction Reduction Through Surface Modification *(ORNL)*

Agreement 11752 – Materials for High Efficiency Engines *(ORNL)*

Agreement 13329 – Mechanical Reliability of Piezo-Stack Actuators *(ORNL)*

Agreement 17257 – Materials for Advanced Turbocharger Design *(ORNL)*

Agreement 18570 – Engine Materials Compatibility with Alternate Fuels *(ORNL)**

Agreement 18571 – Materials Issues Associated with EGR Systems *(ORNL)*

Project 18519 – Materials for Exhaust and Energy Recovery

Agreement 9130 – Catalyst Characterization *(ORNL)*

Agreement 10461 – Durability of Diesel Engine Particulate Filters *(ORNL)*

Agreement 10635 – Catalysts via First Principles *(ORNL)*

Agreement 19214 – Effects of Biodiesel Fuel on Diesel Particulate Filter Materials *(ORNL)*

Agreement 20091 – Electrically Assisted DPF Material *(ORNL)*

<u>Project 18865 – Application Specific Materials Simulation, Characterization and Synthesis</u>

Agreement 9105 – Characterization of Catalyst Microstructures *(ORNL)*

Agreement 14957 – High Temperature Thermoelectrics *(ORNL)*

Agreement 16308 – MBD Thermoelectrics Theory and Structure *(ORNL)*

_____

***No report this period.**

Agreement 19201: Non-Rare Earth Magnetic Materials

Michael A. McGuire, Nirmal J. Ghimire, David J. Singh
Oak Ridge National Laboratory

Objective/Scope

We will examine rare-earth-free chemical systems which hold promise for the discovery of new high-temperature ferromagnets with the large magnetic moments and strong anisotropies required for technologically useful permanent magnet materials. This research will focus on the development of new rare-earth free permanent magnet materials. Understudied chemical systems which are likely to contain materials with properties required for useful ferromagnets (large moments, high Curie temperatures, strong magnetic anisotropy) will be synthesized and characterized. First principle calculations will be performed to aid in the identification of promising target materials and to guide chemical tuning of magnetic properties through element substitutions and alloying. The focus will be on materials based on elements, such as Mn, Fe, Co and Cr, suitable for application in vehicles.

The primary challenge in this work is to obtain high magnetic anisotropy without rare-earth elements, while maintaining high saturation magnetization. The two main sources of anisotropy are magneto-crystalline anisotropy and shape anisotropy. Magneto-crystalline anisotropy is an intrinsic property determined by energy required to rotate a magnetic moment relative to the crystal lattice. Shape anisotropy is an extrinsic property related to the domain structure of individual crystallites. We are targeting intermetallic compounds with large magneto-crystalline anisotropy, which could then be further enhanced by materials processing to optimize magnetic domain configurations. To obtain anisotropic magnetic properties, heavy transition metal elements will be incorporated instead of rare earths.

Technical Highlights

Magnetism and Microstructure in ferromagnetic $Hf_2Co_{11}B$ ribbons.

In last quarter's report, we showed magnetic behavior of melt-spun $Hf_2Co_{11}B$ which appears amorphous by powder x-ray diffraction and how the behavior changed from very soft to hard upon annealing (crystallization) of the material. Figure 1 shows that data along with data from a sample annealed a lower temperature. Clearly a significant change in the magnetic behavior occurs for annealing temperatures between 500 and 600 C. Differential thermal analysis results for the amorphous ribbons are also shown in Figure 1. Two exothermic events are observed at 600 and 650 C. This is consistent with the magnetization results which show a strong difference between ribbons annealed at 500 C and those annealed at 600 C. Microstructural analysis of these samples was carried out in collaborations with Orlando Rios in the Materials Processing Group (Materials Science and Technology Division, ORNL) using a scanning electron microscope at ORNL. Backscattered electron images of as-spun and annealed ribbons are shown in Figure 1. The evolution of the microstructure correlates well with the observed magnetic behavior. The as-spun material shows a curious cellular structure

with the bright (Hf-rich) phase located at the boundaries. Annealing at 500 C had little effect on the microstructure. Annealing at 600 C shows a dramatic change, and clear indications of nano-scale precipitates are observed, while the matrix appears more uniform. We associate these precipitates with the hard magnetic behavior. Transmission electron microscopy experiments and chemical phase analysis for these and related samples is scheduled for May.

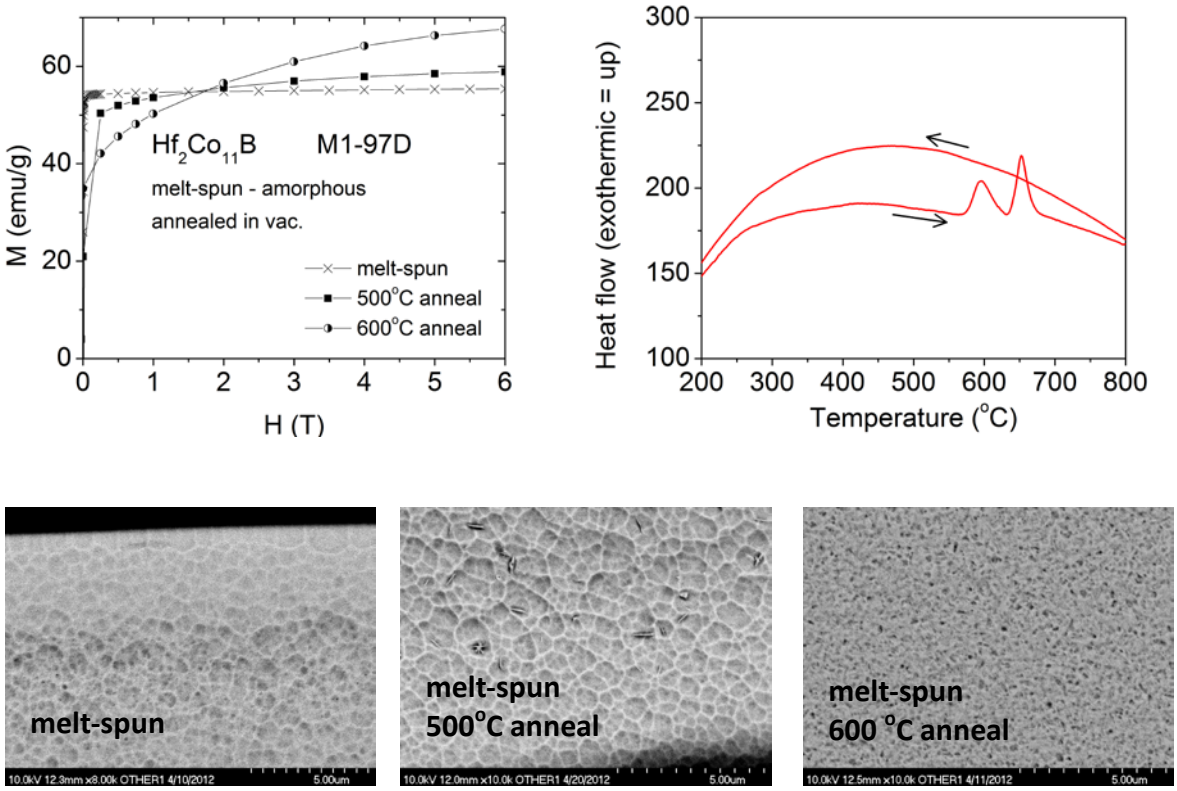

Figure 1. Analysis of amorphous melt-spun $Hf_2Co_{11}B$ and effects of annealing. Magnetization (M) is shown as a function of applied field (H) for the three samples. Thermal analysis shows exothermic events occurring at 600 and 650 C. Microstructure (SEM) analysis reveals precipitates forming as the hard magnetic properties evolve.

Magneto-thermal materials processing

ORNL has world leading capabilities in the field of materials processing under high magnetic field. Processing can be performed at fields as high as 9 Tesla, over a wide range of temperatures, and on an idustrial scale. Figure 2 shows two of the large-bore superconducting magnets operated by the Materials Processing Group led by Bill Peter. Application of high magnetic field can have a strong influence on the thermodynamics, kenitics, and microstructure of materials, and has great promise in tailoring behaviors of permanent magnet materials. We have begun studying the effects of magnetothermal processing on ferromagnets.

Some results for our $Hf_2Co_{11}B$ ribbons are shown in Figure 3. Significantly different and interesting microstructures are obtained in high magnetic fields (compare to Figure 1). Variation of temperature, field strength, and field orientation should allow fine control of microstructures and resulting magnetic properties. Phase analysis and crystallographic and magnetic studies of these magnetothermally processed samples are underway.

Figure 2. Two 9 Tesla superconducting magnets in the Materials Processing Group at ORNL. The horizontal magnet has a 5 inch bore and the vertical magnet has a 9 inch bore. The research-scale experiments performed for this program are conducted in the horizontal magnet.

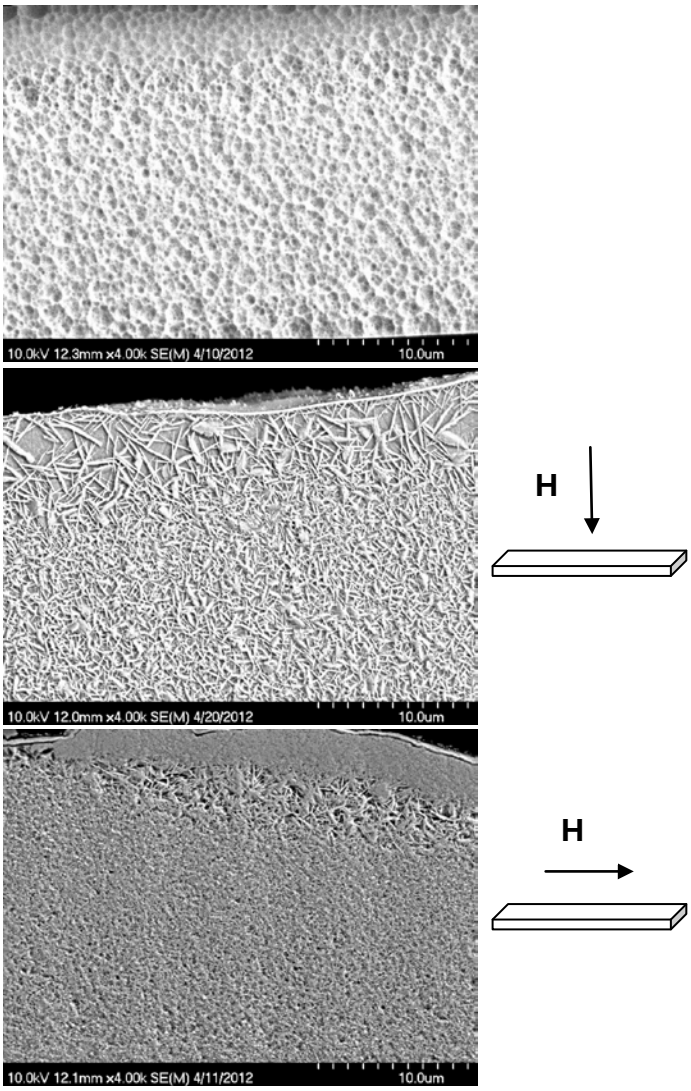

Figure 3.Microstructure of $Hf_2Co_{11}B$ amorphous melt-spun ribbon before (top) and after (middle and bottom) annealing at 600 C for 2 hours in a magnetic field of 9 Tesla. The direction of the field with respect to the ribbons are shown, and the images are from a cross section in the plane of the page. The magnetic field direction has a large effect on the resulting microstructure. These images should also be compared to Figure 1 which shows the result of annealing at the same temperature and for the same time but with no applied magnetic field.

We are currently selecting and synthesizing samples in simpler model systems to determine the kinds of effects possible with magnetothermal processing techniques. In particular, preferential stabilization of anisotropic magnetic phases is being explored.

Nitriding with Ammonia Gas

Reactivity of the ferromagnetic Laves phase $HfFe_2$ with ammonia was examined. We found that even dilute ammonia mixtures and low reaction temperatures result in complete decomposition in to Fe_2N + Hf. Continuing experiments are examining more ionic compounds as starting materials which should limit the rapid decompositions observed thus far in purely intermetallic compounds. These experiments are being conducted through collaboration with the Materials Chemistry Group in the Chemical Sciences Division at ONRL (Craig Bridges, Parans Paranthaman). This group has a sophisticated system in place for reacting materials in controlled atmospheres

composed of various gases and gas mixtures (including ammonia) at elevated temperatures. Arrangements have been made to continue using this setup for this project and will save time and money that would be required to install a duplicate apparatus. Continuing nitride formation experiments are underway.

Status of FY 2012 Milestones

(1) Determine usefulness of metal flux synthesis technique for producing crystals of new ternary phosphides with transition metal concentrations approaching and exceeding 70 %, anisotropic structures, and Curie temperatures in excess of 300 °C. Results will be summarized in a report and, if appropriate, a manuscript for publication in the scientific literature. (09/2012)

Specific ternary compounds (primarily phosphides) are being targeted in parallel using this approach and more traditional powder-metallurgy techniques. Solubility of refractory metals and iron continues to present challenges.

(2) Develop capabilities to produce sub-nitrides using flowing ammonia gas, and examine effects of mild nitriding conditions on magnetic intermetallic compounds, with the aim of enhancing Curie temperature to values above 300 °C and increasing their magnetic anisotropy, a requirement to produce energy products competitive with RE magnets (~ 30 MG Oe). Results will be summarized in a report and, if appropriate, a manuscript for publication in the scientific literature. (09/2012)

Arrangements have been made to conduct nitriding experiments in the Materials Chemistry Group in the Chemistry Division at ORNL. These facilities will be used by the project for the remainder of FY2012.

Communications/Visits/Travel

None to report.

Problems Encountered

None to report.

Publications/Presentations/Awards

Results of our study into the structural and magnetic properties of μ-phases were reported at the March Meeting of the American Physical Society in Boston, MA by UT graduate student Nirmal Ghimire.

References

None to report.

Agreement 23278: Low-Cost Direct Bonded Aluminum (DBA) Substrates

H. -T. Lin, A. A. Wereszczak, and Shirley Waters
Oak Ridge National Laboratory

Objective/Scope

This project seeks to develop low-cost, high quality, and thermomechanically robust direct-bonded aluminum (DBA) substrates. Low-cost DBA substrates will lessen the cost of the inverter insulated gate bipolar transistor (IGBT) power modules while concomitantly sustaining or improving thermal management and improving thermomechanical reliability. Compared to copper and DBC substrates, aluminum has a lower elastic modulus so it imparts a lower stress on the ceramic substrate it sandwiches, and this contributes to improved mechanical reliability of the entire substrate. Wire and ribbon for bonding in power electronic modules tends to be aluminum, so the apparent coefficient of thermal expansion of DBAs is compatible with them unlike DBCs. The use of a DBA substrate will also lessen the weight up to 50% compared to presently used DBC substrates, and this would contribute to the weight reduction goals of the inverter and converter in the APEEM program as well.

Technical Highlights

The Scanning Acoustic Microscopy (SAM), as shown in Fig. 1, was employed as a nondestructive tool to detect the presence of defects (e.g., voids, cracks, or delamination) in the as-received commercially available direct-bonded aluminum (DBA) and direct bonded copper (DBC) substrates and also these substrates after the thermal cycle testing. The system has the ability to create images by generating a pulse of ultrasound, which is focused to a pinpoint spot. The pulse is sent into a sample, which is immersed in the water, and reflected off of interfaces. The frequency of the pulse and design of the lens are chosen to optimize spot size resolution and depth penetration for each application. In the reflection mode of operation the same transducer, which scans over a 2D surface of samples, is used to send and receive the ultrasonic pulse. Return echoes arrive at different times based upon the depth of the reflecting feature and the velocity of sound in the materials. The operator positions an electronic gate to capture the depth of interest. The amount of ultrasound reflected at the interface is based on the differences in the materials at the interface. The more different the materials the more ultrasound reflected. The time gating is then used to select specific region to examine. A schematic of the probe and substrate is also illustrated in Fig. 2. The echoes from each scan position are typically displayed as a brightness (echo amplitude) line. Time-Of-Flight (TOF) information, which is also collected, can be used to estimate speed of sound within the material. If density of materials is known, the elastic modulus can also be calculated as well.

Figure 3 shows the SAM images of two commercial DBA substrates (designated as DBA-A and DAB-B) with AlN ceramic. Note that the scratch line appeared in Gate 4 (rear surface) was intentionally introduced for identification purpose. In general the as-received commercial DBA-A exhibited no apparent defects within the resolution of this SAM system, while the commercial DBA-B showed white strips present at Gate 2, which

might suggest some kind of defects or secondary phase that existed at the aluminum and AlN interface after processing. The previously reported SEM analysis of a metallographic polished cross section of as-received DBA-B sample indicated that there was a thin layer of Al-Si 2nd phase present at the interface, which might correspond to the observed white strips image. In addition, the SAM images of DBC substrate with Al_2O_3 and AlN are shown in Fig. 4a and Fig 4b, respectively. Results also showed that no apparent defects were detected at these interfacial layers, which suggested these two DBC substrates exhibited good coherent interfacial bonding and quality. The SAM results of these DBC substrates are consistent with the SEM observations of polished cross section samples, and suggest that the SAM technique could be used as a useful tool to detect the possible defects present before and/or after thermal cycle tests.

Detailed electronic microscopy analysis of a commercial DBC with silicon nitride ceramics was performed during this reporting period as well. The SEM micrograph of this commercial DBC was shown in Fig. 5. It is apparent that the active metal brazing paste containing Ti and Ag was used for the joining process, as clearly shown in the EDAX element maps in Fig. 6. The Ti-based active brazing paste has been widely used to join silicon nitride to other metallic alloys [Refs]. Note the presence of Mg came from the sintering addition of silicon nitride ceramic, and the carbon most likely resulted from the coating. SEM observations suggest that there is a coherent and sound interface between silicon nitride ceramic and Cu. Note electronic substrates with silicon nitride ceramic have been developed for the higher temperature and voltage application conditions due to the much better mechanical performance (fracture strength and toughness) compared to Al_2O_3 and AlN.

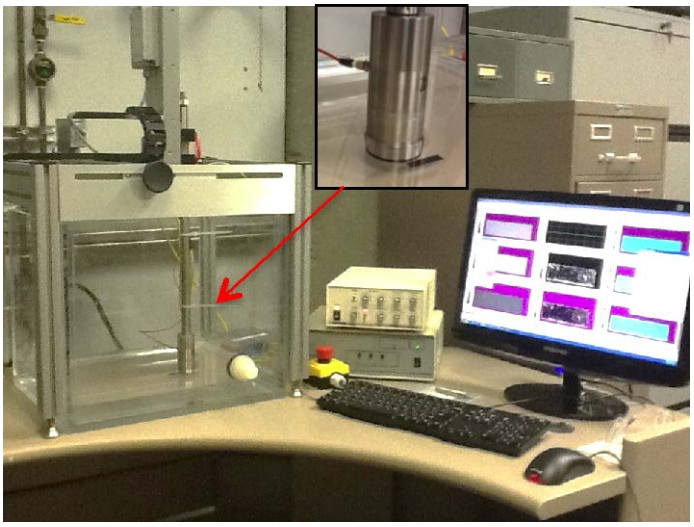

Figure 1. Photo of scanning acoustic microscopy system. The arrow indicates the probe with the enlarged photo inserted.

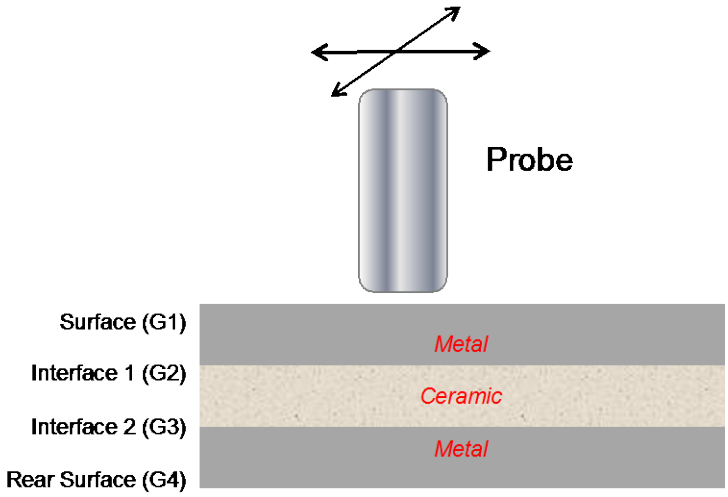

Figure 2. Schematic of SAM probe with gate designations for a DBA or DBC type substrate.

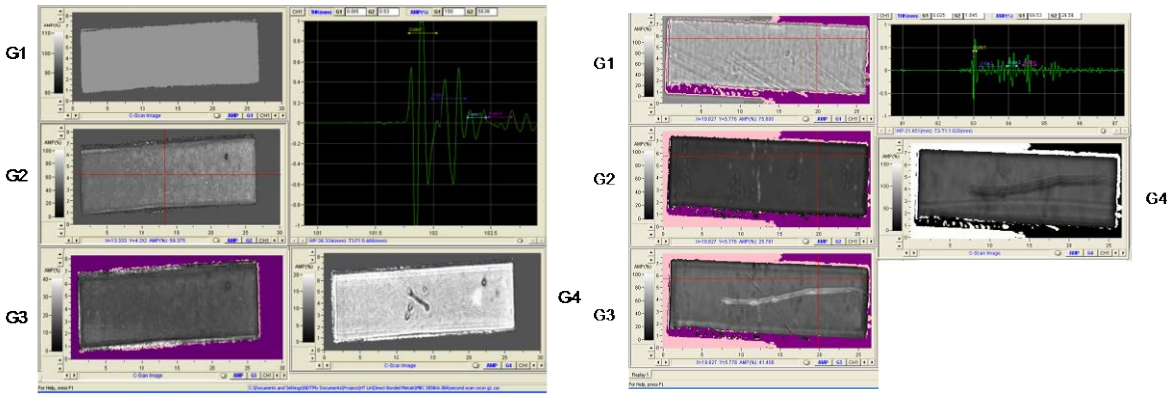

Figure 3. SAM images of commercial DBA-A (LHS) and DBA-B (RHS).

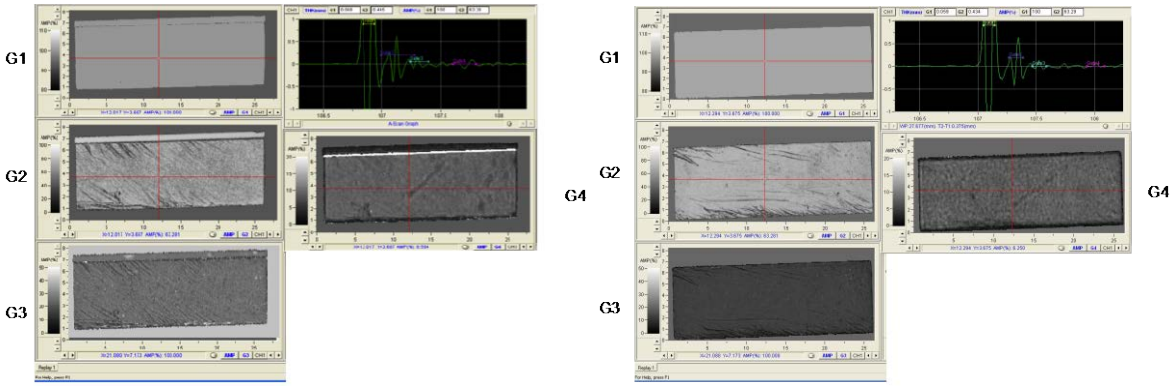

Figure 4. SAM images of commercial DBC with AlN (LHS) and DBC with Al_2O_3 ceramic (RHS).

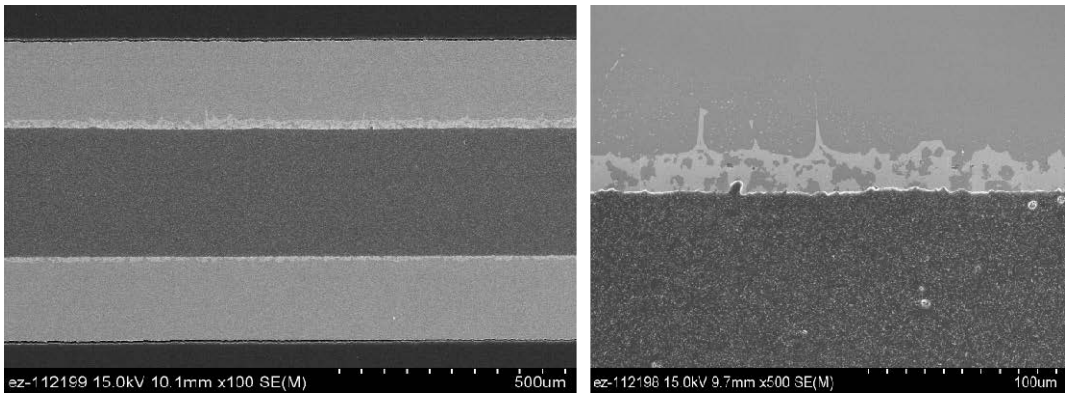

Figure 5. SEM micrograph of a commercial DBC with silicon nitride ceramic.

Status of FY 2012 Milestones

(1) Complete characterization of microstructure, and physical (coefficient of thermal expansion and thermal conductivity) and mechanical strength of commercially available DBA substrates up to 200°C. (09/2012) – On schedule.

(2) Complete fabrication of DBA substrates manufactured via new ORNL processing method and compare thermal cycling response between –40°C and +150°C in air against that of commercial DBA substrates. (09/2012) – On schedule.

Communications/Visits/Travel

- Several discussions have occurred with ORNL/NTRC, USCAR EETT, General Motors, and NREL staff members about the research and benchmarking plans for this project.

Problems Encountered

The vacuum pump system did not function properly and, thus, a proper vacuum could not be achieved in the furnace, which caused minor delay in the processing of DBA substrates.

Publications/Presentations/Awards

Poster on this project was presented at DOE Advanced Power Electronics and Electric Motors R&D FY12 Kickoff Meeting, Nov. 3, 2011

References

1. Zhuravlev VS, Prokopenko AA, Kostyuk BD, Gab II, Naidich YV. “Joining of Si3N4 with Ti-active Cu–Ga and Cu–Sn filler alloys.” p. 299–305, in Eustathopoulos N, Sobczak N, editors. Proc. Int. Conf. High-Temperature Capillarity, 1997.

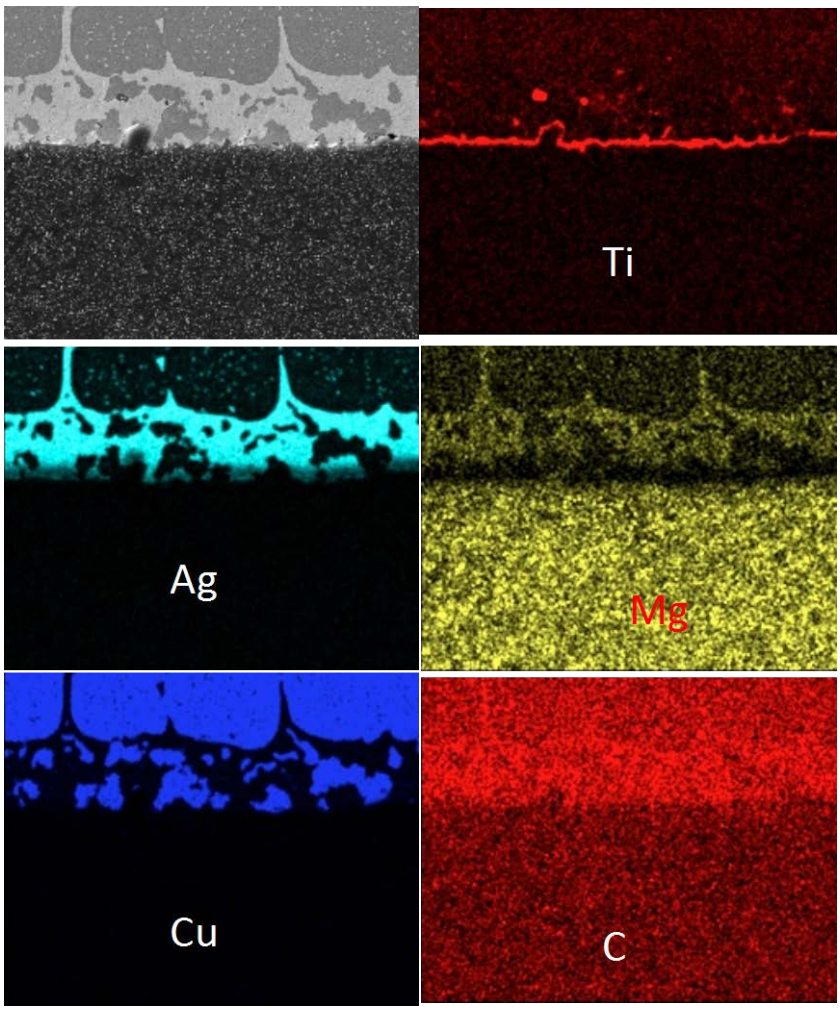

Figure 6. EDAX element map of a commercial DBC with silicon nitride ceramic (as shown in Fig. 5).

Agreement 23279: Improved Organics for Power Electronics and Electric Motors

A. A. Wereszczak, T. G. Morrissey, H. Wang, H. -T. Lin, and M. K. Ferber
Oak Ridge National Laboratory

Objective/Scope

Identify lower-cost and better-performing organic compounds for dielectric and thermal management applications in power electronics and electric motors. Candidate and new organic compounds (e.g., epoxy molded compounds or EMCs) will be characterized and developed to promote low-cost fabrication, volume reduction, mechanically resilience, and improved and alternative thermal management exploitation. They include compounds presently used in dielectrics in power electronic devices, potting compounds used with capacitors, and pottings used in motors. For dielectrics, improved performance represents a higher-temperature capability and the sustainment of dielectric and gel-like mechanical damping properties under thermal cycling and vibratory conditions. For potting compounds used with capacitors or motors, interest exists to identify alternatives that have higher thermal conductivity (or that enhance the thermal conductivity of existing compounds) or that benefit structural or damping performance without compromising thermal performance.

Technical Highlights

A meeting was held with an epoxy molding compound (EMC) manufacturer (SolEpoxy) to discuss the use of MgO as a filler material as well as a high-temperature-capable epoxy in future EMC processing trials. A powder supplier (Ube) provided MgO powder and SolEpoxy will fabricate EMC coupons for thermal property testing at ORNL. Receipt of the MgO-filled EMCs shall occur in early Q3. John Miller, a PI at the National Transportation Research Center who is funded by the VTP PEEM program, wishes to consider this MgO-filler EMC in his developmental work for improved thermal management of motor components.

A model EMC was made using monosized 1-mm diameter stainless steel spheres to enable fundamental study, measurement, and modeling of thermal conductivity, coefficient of thermal expansion, and elastic properties. An image of the "composite" disk is shown in Fig. 1. Those properties are being measured as of this writing and will be reported on in Q3.

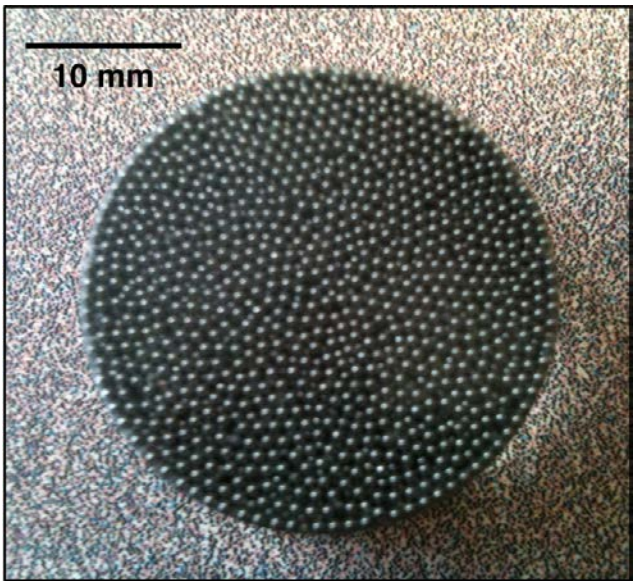

Figure 1. Image of a monosized filled (1-mm-diameter stainless steel spheres) epoxy molding compound. This simple system will allow for the fundamental measurement and modeling of thermal and elastic properties in this composite structure.

Status of FY 2012 Milestones

Model, design, and fabricate filler-containing-EMC having 10x thermal conductivity increase over monolithic epoxy. [Sep12] *On schedule.*

Communications/Visits/Travel:

Robert Groele and Barry Goodin visited ORNL on 31 January 2012 to discuss future collaborative plans for developing thermally conductivity EMCs.

Problems Encountered

None.

Publications/Presentations/Awards

Wereszczak gave an invited presentation entitled "ORNL Materials Work" to the USCAR EE Tech Team Group, Southfield, MI, on 22 March 2012. Audience members were from the US DOE EERE VTP, Chrysler, Ford, General Motors, NREL, and ORNL.

References

None.

Agreement 19202: Titanium Friction and Wear (Surface Engineering of Bearing Components)

Peter Blau and Dinesh Bansal
Oak Ridge National Laboratory

Objective/Scope

The energy efficiency of internal combustion engines (ICEs), whether fueled by conventional or alternative fuels, benefits from the use of lightweight materials. Examples include polymer composites and alloys of aluminum, magnesium, and titanium. While such materials offer attractive efficiency gains, their use also presents technical and economic challenges. One class of ICE applications involves tribological aspects: that is, those which concern friction, wear, and lubrication. Studies in the United States, Japan, and the United Kingdom have shown that mechanical losses comprise about fifteen percent of the energy dissipation from fuel in a typical ICE, and that of those, energy losses by friction comprise about eighty percent. The two major subsystems, in terms of engine frictional losses, are the piston ring/cylinder interface and the crankshaft bearings, including those on the connecting rods. The current project which began in FY 2010 not only addresses the potential use of lightweight alloys in connecting rod bearings, but it also investigates the degree to which surface engineering and coating technologies could benefit other friction- and wear-critical applications as well.

The objective of this project is to *enable the use of strong, lightweight titanium (Ti) alloys for wear and friction-sensitive engine components like connecting rods (CRs) and crankshafts.* The goal is to identify the most promising surface engineering methods, whether commercialized or experimental, to reduce friction and wear of Ti alloys under lubricated, engine-like conditions. This work compliments recent developments in Ti processing technology that are aimed at reducing raw materials cost. It utilizes the experience of ORNL tribology staff to effect changes in surface-critical properties via a variety of potential treatments and combinations of treatments. The phases of this three-year effort that began in FY 2010 are: 1) *Friction and wear screening* of multiple surface treatments and coatings for titanium using ASTM standard coupon tests to down-select leading performers, 2) *Design and construction of a computer-controlled, variable load bearing tester* (VLBT) to simulate the contact pressure and lubricant regime excursions experienced by connecting rod bearings, and 3) to present a realistic assessment of which *surface engineering methods may be most beneficially applied to Ti alloys for use in diesel engine connecting rods.* The latter is to be based upon experimental results from this project.

Technical Highlights

Effects of cold-working combined with diffusion treatments. In the previous quarterly, a set of reciprocating ball-on-flat friction and wear experiments was described in which the potential benefits of mechanical cold-working plus diffusion treatments on a titanium alloy were explored. These involved the following:

- Bare titanium (Ti-6Al-4V) alloy (as the baseline)
- Shot-peening
- Planishing (repetitive hammering)
- Nitriding plus shot peening
- Oxygen diffusion plus shot peening

Note that in the latter, duplex treatments, mechanical working was performed last because the diffusion treatments involve heating the material, which could diminish the effects of cold working. Recognizing that adhesive transfer of material from one surface to another during sliding can exacerbate friction and wear, tests of the foregoing surface treatments were conducted using both bearing steel and ceramic sliding counterfaces, the latter having a reduced propensity to transfer. In tests run in fresh 15W40 diesel oil, it was found that there was no benefit of mechanical working by itself on the friction and wear of the alloy; however, when it was preceded by diffusion treatments (nitriding, oxygen diffusion) the low friction and wear period at the beginning of the runs was lengthened. An example of this is shown in Figure 1 for two sliding materials against nitrided then shot-peened Ti-6Al-4V alloy. Note that the horizontal axis is a log scale in order to emphasize the early stages of sliding. Clearly, there is a low friction period for both slider materials, but that for the ceramic ball transitions earlier to a high friction level of over 0.4. This shortened transition period is thought to be due to an earlier wear-through of the nitrided layer by the harder ceramic ball. Note also how similar the shapes of the friction versus log distance curves are, indicating that the contact surfaces experience a similar progression of damage modes once the nitride layer becomes compromised. The results of this work on combined mechanical treatment and diffusion treatments will be submitted to the International Conference on Wear of Materials (WOM 2013).

Design and construction of variable load bearing tester (VLBT). The final design configuration includes a metering system to dispense droplets of oil. A program in LabVIEW™ was created by Dr. Bansal to control the test rig while simultaneously acquiring normal force, friction force and speed data. It is shown schematically in Figure 2. The compound load application arm was added to reduce signal cross-talk between normal and tangential force sensors. A precision lubricant application system was also installed to provide as little as one drop of oil every 30 s.

A series of tribo-tests with lubricated bronze against steel was conducted on the VLBT to measure the differences in friction and wear that result from constant load versus variable (spectrum) loading conditions. This work is aimed at developing an ability to predict friction and wear behavior of bearings that operate at time-varying contact conditions, like those in many practical mechanical systems, including the large and small end bearings on connecting rods. Once such effects are determined on baseline materials, work on surface treatments will continue under spectrum loading conditions using the down-selected candidate surface treatments.

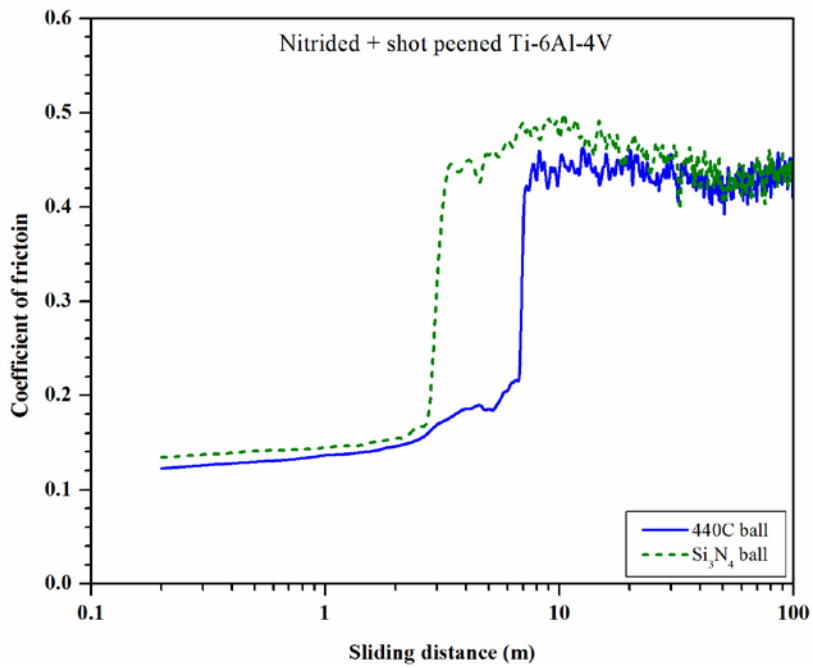

Figure 1. Effects of duplex treatments and slider material on the length of the pre-transition period from mild to severe adhesive wear and to higher friction.

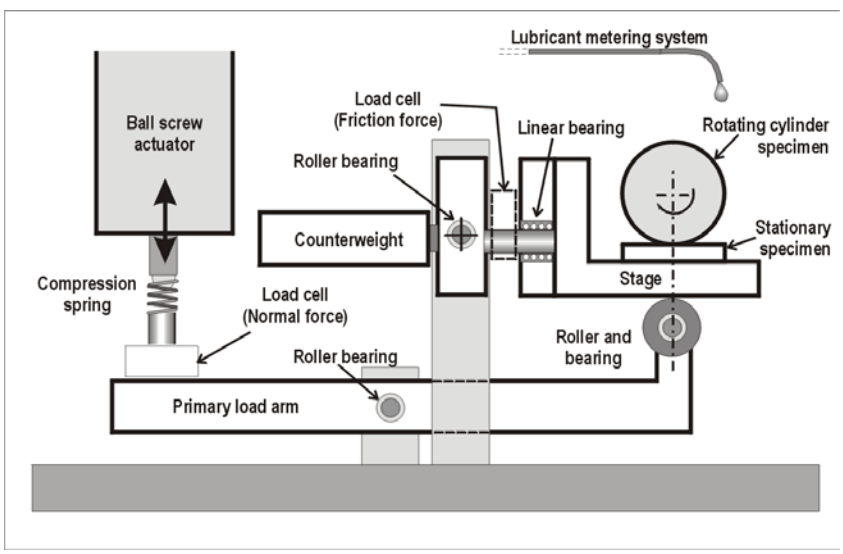

Figure 2. Mechanical configuration of the VLBT. The loading system has been isolated from the specimen holder pivot to avoid cross-talk between the normal force and friction force.

Figure 3. K. Cooley (left), ORNL tribology technician, and D. Bansal (right), post-doctoral associate, make final adjustments in preparation for a VLBT run.

Dinesh Bansal joins Cummins Engine Company. Dinesh Bansal, a post-doctoral researcher and contributor to this project for two years, has accepted a position at Cummins Engine Company in Columbus, Indiana (see Figure 3 above). With an M.S. from Purdue University and a PhD. from Georgia Tech, both in mechanical engineering, Dr. Bansal worked on the procurement and testing of titanium surface treatments as well as leading the design and construction of the VLBT. We wish him well in his new position and look forward to additional collaborations with Cummins in the area of engine tribology.

Future Plans.

- Complete the analysis of the near-surface residual stresses (by X-ray methods) on diffusion-treated and work-hardened Ti-alloy surfaces.

- Continue work on characterizing the effects of spectrum loading on the friction and wear of different surface treatments using variable load bearing tester (VLBT))

- Begin work on the final report to evaluate the use of surface engineered titanium as a sliding bearing surface in a connecting rod large-end bearing.

Status of Milestones

1) Complete tests of candidate coatings and multiple surface treatments using the variable-load bearing test system (VLBT)**. (09/11)** *Postponed until 06/2012 to make improvements in the VLBT fixtures, electronic motor controls, and data acquisition program.*

2) Complete analysis of VLBT test surfaces and prepare a final report summarizing the work on this effort that culminates in a design concept for Ti-alloy connecting rods with integral bearing surfaces. (09/12)

Communications/Visits/Travel

None this quarter.

Problems Encountered

The VLBT was not performing as expected based upon the original design concept, so changes had to be made in both mechanical and electronic controls systems. This delayed the start of screening tests under variable-load conditions, but the system is now operational.

References

None

Publications and Presentations

A paper is in preparation for the 19th International Conference on Wear of Materials (WOM 2013).

Agreement 23284: Friction Reduction Through Surface Modification

Peter J. Blau
Oak Ridge National Laboratory
and
Stephen M. Hsu
George Washington University

Objective/Scope

The primary objective of this two-year effort is to improve the fuel efficiency of diesel-powered vehicles by employing carefully designed patterns of micro-scale features to reduce the friction of contacting surfaces. These features function in two ways: (1) by increasing the thickness of the lubricant film in order to separate bearing surfaces, and (2) by trapping harmful wear debris particles in depressions below the contact surface. One bearing surface of particular interest is that between the piston ring and cylinder liner, although other frictional surfaces in engines, like those of bucket lifters and cam lobes are also of interest.

The scope of this effort includes the preparation and testing of textured bearings produced by various surface engineering methods. During FY 2011, ORNL prepared indentation-textured surfaces on bearing materials, and investigated the effects of on wear and friction as a function of sliding time. Changes in the morphology of the surfaces during the running-in stages were correlated with the friction coefficient versus time sliding history. Understanding the running-in period is key to separating the contributions of as-finished surface roughness, wear-in, and lubricant conditioning as the bearing system approaches its longer-term, steady-state condition. A subcontract with George Washington University complements in-house efforts by developing and demonstrating a new masking technology to enable the surface patterning of curved surfaces like those on piston rings and cylinder bores.

Technical Highlights

Compression Texturing. As mentioned in the last quarterly report, experiments were conducted to investigate the effects of indentation array texturing (ITx) on friction of bearing bronze (CDA 932) and titanium alloy (Ti-6Al-4V). After producing patterned arrays of over 3000 impressions and measuring their friction during sliding, it was found that for counterformal contacts (ball-on-flat), the polish on the flat surface has a greater effect on friction reduction in the boundary lubrication regime than does ITx. Furthermore, ITx worked better on the bronze because, despite its lower hardness, the bronze is more wear-compatible with the steel than was the Ti-6Al-4V.

This quarter, we established the feasibility of creating textures on bearing surfaces by using impressed patterns. The approach, which we shall call surface compression texturing (CTx), was applied to the bronze bearing alloy in order to create a complex pattern whose feature shapes and depths can be controlled based on the compression force applied and the pattern of a hard grid that is used to indent the surface. Working with D. Erdman of ORNL's Polymer Matrix Composites Group, P. Blau was able to produce patterns such as those shown in Figure 1. During the next quarter, further

tests will be performed to study how the geometry and depth of the pattern can be controlled by adjusting the compression force. In addition, friction tests will be conducted on these patterned surfaces using a variable load bearing tester in order to determine the extent to which they can, but channeling lubricant flow through the contact during sliding, lower friction under diesel oil-lubricated conditions.

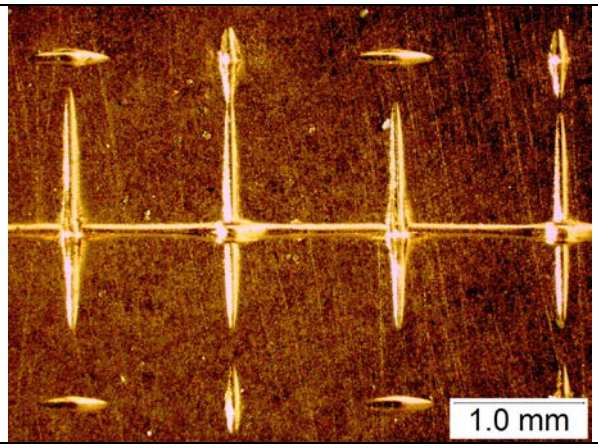	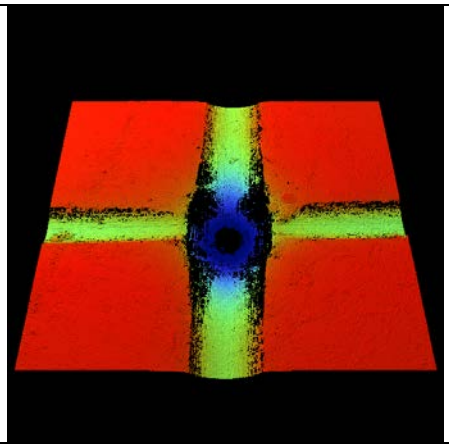
Coarse pattern spacing in a bearing bronze alloy	CTx pattern intersecting channels and a deeper dimple (about 55 □m deep)at the intersection point

Figure 1. Textures on a bearing bronze alloy (CDA 932) produced by CTx. (a) light optical micrograph, and (b) vertical scanning interferomety image showing the deepest (blue) area at a groove crossing point.

Progress at George Washington University (subcontract). Due to changes in the funding profile, it was necessary to modify the milestones in the GWU subcontract. These are reflected in the "Status of FY 2012 Milestones" section below. These changes also affect the ORNL milestones because ORNL was depending on GWU for test specimens and the provision of those specimens will now be delayed.

<u>Status of FY 2012 Milestones</u>

1) (GWU subcontract) Submit report on the Cameron-Plint test procedure and the associated data for friction reduction under various conditions (12/31/2011). *Status: completed on schedule*.

2) (GWU subcontract) Develop a test procedure using an Atomic Force Microscope to measure the influence of nanoclay particles on the global mechanical properties of the clay infiltrated nanocomposites. Submit report containing an AFM test procedure in an ASTM standard format (1/31/ 2012). *Status: completed on schedule*.

3) (ORNL) Conduct lubricated friction tests using ASTM G181, and curved specimens with patterns found to offer the most promise for friction reduction and present a

report on the results (6/30/12). *Status: awaiting specimens from GWU in order to begin testing.*

4) (ORNL) Working with a U.S. diesel engine manufacturer and George Washington University, develop a guideline report for applying textured surfaces to pistons and other promising components to affect fuel savings (9/30/12). *Status: this milestone may need to be postponed until 2013 due to a pending modification of the GWU subcontract*.

Communications/Visits/Travel

None.

Problems Encountered

Initial plans included the provision of test specimens of textured surfaces to ORNL for testing in the spring of 2012; however, the GWU subcontract was first signed in mid-year 2011 and the production of test specimens is about six months behind schedule based on an earlier start. This may impact FY 2012 milestone 3.

Publications/Presentations/Awards

P. J. Blau (2012) "Use of Textured Surfaces to Mitigate Sliding Friction and Wear of Lubricated and Non-Lubricated Contacts – An annotated literature review," ORNL Technical Report ORNL/TM-2012/20, 19 pp. Printed and available through DOE/OSTI.

References

None

Agreement 11752: Materials for High Efficiency Engines

Govindarajan Muralidharan and Bruce G. Bunting
Oak Ridge National Laboratory

Objective/Scope

To identify and catalog the materials operating conditions in the HCCI engines and utilize computational design concepts to develop advanced materials for such applications.

Technical Highlights

In this quarter, work was continued on Ni-based alloys for valve applications. As reported earlier, using thermodynamic modeling, microstructure evaluation, and mechanical property evaluation, high temperature fatigue was identified as a property of critical interest in Ni-based alloy valve materials for the next generation automotive engines. In order to develop relationships between the microstructures of the alloys and their mechanical properties, high-temperature fatigue property data were obtained on all down-selected alloys as a part of the project. Using the approximate correlation between the fatigue lives obtained using the rotating beam and fully reversed fatigue testing techniques several alloys with required microstructures have been identified as candidates for high temperature valve applications.

Using the microstructures of these alloys as a guide, computational thermodynamics was used to identify additional alloys with microstructure similar to the commercial alloys with desirable properties. In contrast to the commercially available alloys with high Nickel contents (> 75%), the Ni-content in these alloys ranges from about 30 wt. % to 45 wt. % with the potential to achieve comparable properties. This implies that the alloys will be of lower cost but comparable mechanical properties.

Results from the fatigue tests on newly developed alloys HCCI-9 and HCCI-16 showed that new alloys with greater strength levels were required to perform at 870°C and stress levels of 35 Ksi. Work continued in designing and fabricating new alloys aimed at increasing the strength levels. These alloys were vacuum arc cast into billets of size 1”x1”x3”, rolled, heat-treated, Table 1 shows the newly developed alloys and their measured yield strengths at 870°C in the aged condition. It was concluded that further effort was required to achieve yield strengths of >75 Ksi.

This quarter several new alloys were designed with a slightly modified design strategy. These alloys are modified versions of HCCI41M reported in earlier reports in this project. Table 1 shows a significant improvement has been achieved in the yield strength of the alloys developed using the new design strategy. Note that an improvement of 25-40% has been achieved over the properties of previous versions of these alloys. **These are some of the highest strength levels that have been achieved in this project**.

Alloy Designation	**Yield Strength at 870°C (Ksi)**
Quarter 1, 2012	
HCCI-490-1	65.4
HCCI-490-2	68.8
HCCI-490-3	66.7
HCCI-490-4	66.6
HCCI-490-5	63.5
HCCI-490-6	62.0
Quarter 2, 2012	
HCCI-41M3	**78.5**
HCCI-41M4	**70.4**
Previous Results	
HCCI-41M	56.3

In this quarter, a larger batch of HCCI-41M3 will be prepared for fatigue tests.

Status of FY 2012 Milestones

(1) Complete rotating beam fatigue tests on at least two new alloys at 870°C, and stress greater than 25Ksi. (9/2012) On Track

(2) Demonstrate a lifetime of >100 million cycles to failure at a stress level greater than 25 Ksi. (9/2012) On Track

Communications/Visits/Travel

Problems Encountered

Publications/Presentations/Awards

References

Agreement 13329: Mechanical Reliability of Piezo-Stack Actuators

H.-T. Lin, H. Wang, F.W. Zeng, A. A. Wereszczak
Oak Ridge National Laboratory

R. Stafford and D. Memering
Cummins Inc.

Objective/Scope

Enable confident utilization of piezo stack actuator in fuel injectors for heavy vehicle diesel engines. The use of such actuators in diesel fuel injectors has the potential to reduce injector response time, provide greater precision and control of the fuel injection event, and increase fuel efficiency. Though piezoelectric function is the obvious primary function of lead zirconate titanate (PZT) ceramic stacks for fuel injectors, their mechanical reliability can be a performance and life limiter because PZT ceramic is intrinsically brittle, lacks high mechanical strength, and is susceptible to fatigue. However, that brittleness, relatively low strength, and fatigue susceptibility can be overcome with the use of appropriate structural ceramic probabilistic design and reliability methods.

Technical Highlights

1. Testing and Characterization of PZT Ceramics

Effect of humidity on flexural strength of PZT - Lead zirconate titanate (PZT) ceramic specimens acquired from Piezo Systems, Inc. (PSI) was studied in this quarter with an emphasis on the effect of humidity and time of aging. Particularly, PSI 5A4E was used because this material had the piezoelectric properties equivalent to those of EPCOS PZT stacks currently considered for the fuel injectors in heavy duty diesel engine. Preparation of PZT specimens, specimen dimensions, and ball-on-ring (BoR) test conditions, including electric mechanical and electric loading, all were same as reported before.[1,2] The study on the humidity effect was accomplished through pre-treating the PZT specimen in a chamber in a specified period of time. The chamber environment was controlled using potassium bromide solution at 81% R.H. (relative humidity) and 22°C. There were some minor weight gains after the pre-determined exposure of humidity treatment. For example, after aging of 10 days, the maximum weight gain among the groups of 12 specimens reached 6 mg. However, under all of the tested electric conditions (OC, +1.2kV/mm, -1.2kV/mm), the effect of humidity treatment up to 10 days or one month on the flexural strength was not shown to be statistically significant. The confidence ratio rings of flexural strength based on BoR test is given in Fig. 1. Therefore, results indicate that the performance of PZT was quite stable under the level of humility and aging time employed in the current study. The further treatment with longer period up to one year is undergoing, and results will be reported in the future.

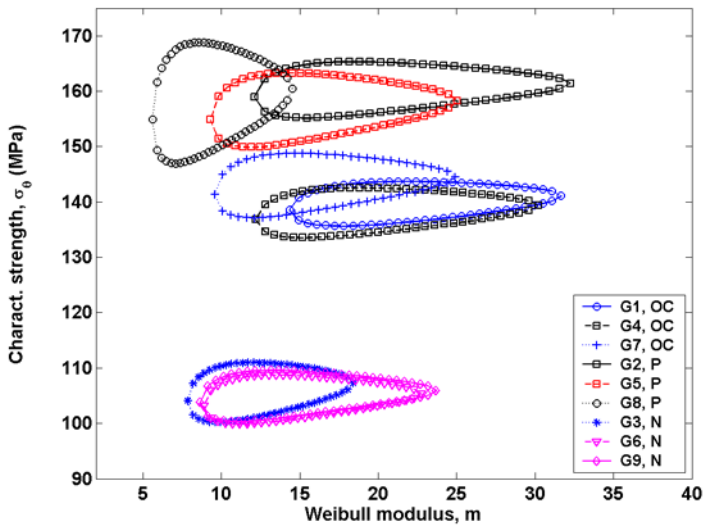

Fig. 1. Confidence ratio rings of mechanical strength of PSI 5A4E specimens in 95% confidence level. The results were obtained using BoR test. Data set G1, G2, G3: no humidity exposure (baseline data); G4, G5, G6: 10 days of 85% R.H. exposure; G7, G8, G9 1 month of 85% R.H. exposure. Each data set consisted of 12 tests. OC: open circuit; P: electric field is along poling, 1.2kV/mm; N: electric field is against poling, -1.2kV/mm.

2. Testing and Characterization of PZT Stacks

2.1 Uncapsulated EPCOS stacks - Uncapsulated EPCOS stacks (12mm × 12mm × 54mm, 16.15 μF, rated voltage 160 V) were screened. The stack that still has good electric resistance was selected and prepared for the cycling test. The piezo stack fatigue setup built for the small EPCOS stacks (6.8mm × 6.8mm × 30mm) was modified, including the transmitting rod, guiding rods, and target rods. The initial run using an uncapsulated EPCOS stack with electric loading of 160V, 20Hz resulted in surface dielectric breakdown. The breakdown was localized to the middle lateral area of the stack, but caused the immediate degradation of performance. Therefore, the procedure is needed to control the dielectric breakdown in the next step.

2.2 Low-profile NOLIAC stacks using piezodilatometer - The alternative is being pursued to test low-profile PZT stacks using piezodilatometer. The aged (> 3 years) 10-layer PZT plates, NOLIAC CMAP07 (5mm × 5mm × 2mm, 10nF, rated voltage 200 V), were tested at first under a controlled electric loading. However, such stack size was not found to properly fit into the test stage and provide a reliable reading on the displacement output.

NOLIAC stacks with larger lateral dimensions; i.e., CMA09 (10mm × 10mm × 2mm, 440nF, rated voltage 200V), were thus used. Driving such size of stacks was enabled in the high electric field for the designed accelerating fatigue test because the current piezodilatometer was equipped with a Trek PZD 2000A that has a current capacity of ± 400 mA.

Measurements and cycling procedures mostly followed those established for single layer PZT,[3] but with some modification with respect to the testing of large size stacks.[4,5] Five electric cycle tests using 6kV/mm at 100Hz were completed. One of the stacks passed 10^6 cycles, whilst the rest stopped near 2.8×10^5 to 3.9×10^5 cycles. All of the stacks were found to be entirely breakdown and not functional any more. So, the electric fatigue of the stacks has been accelerated by using high electric field driving. Both the as-received and failed stacks were imaged using scanning acoustic microscopy (SAM). Cracking and delamination were clearly revealed across the stacks as shown in Fig. 2.

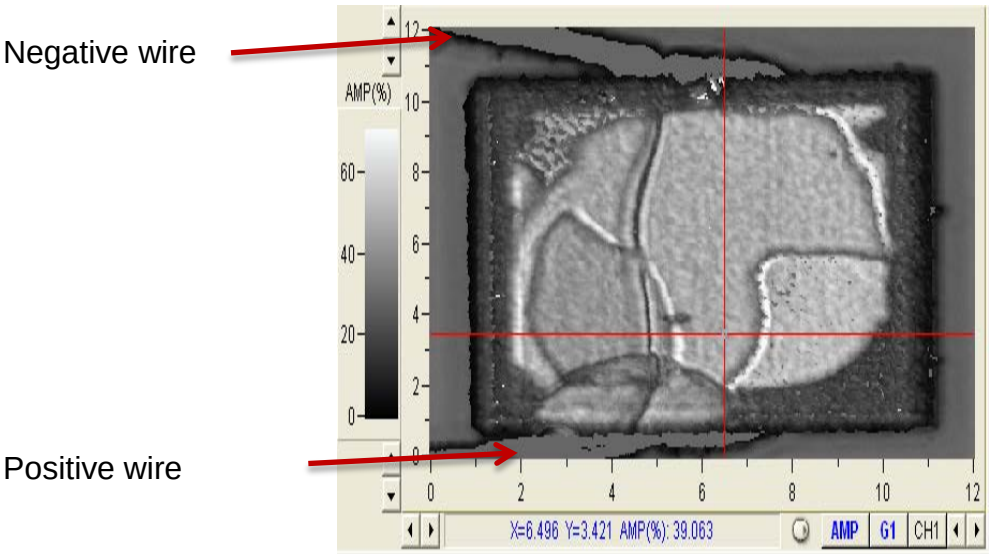

Fig. 2 Image of failed stack SCMA09 #01, based on scanning acoustic microscopy.[6]

The failed stack was subsequently sectioned between the positive and negative wires and metallurgically polished. The extensive cracks were indeed observed to be across the PZT layers and extended to the inactive zones and regions as shown in Fig. 3.

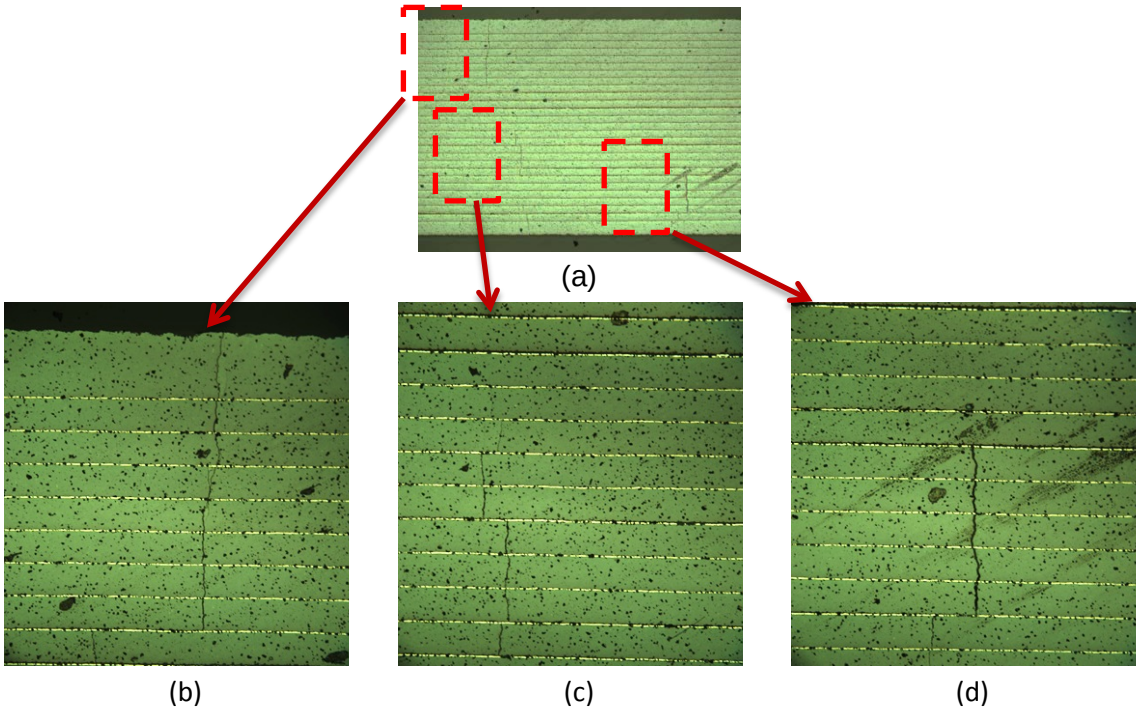

Fig. 3. Optical images of (a) part of cross section of the same PZT stack as in Fig. 2, and (b), (c), (d) enlarged areas.

Status of FY 2012 Milestones

Measure and compare reliability of competing commercially available piezoactuators under consideration for use in diesel fuel injectors, *on schedule*.

Communications/Visits/Travel

Communications with Cummins, Inc. were maintained on CRADA update.

Publications/Presentations/Awards

1. Wang, H., Matsunaga, T., Lin, H.-T., and Mottern, A. M., "Piezoelectric and Dielectric Performance of Poled Lead Zirconate Titanate in Electric Cyclic Fatigue," *Smart Mater. Struct.*, 21 (2), 2012, 025009.
2. Zhang, K., Wang, H., and Lin, H.-T., "Strength Properties of Aged Poled Lead Zirconate Titanate Subjected to Electromechanical Loadings," *J. Am. Cera. Soc.* submitted.

References

1. Wang, H., Lin, H.-T., and Wereszczak, A. A., Strength properties of poled lead zirconate titanate subjected to biaxial flexural loading in high electric field, J. Am. Ceram. Soc., 93 (9), 2010, 2843-2849.

2. Wang, H. and Wereszczak, A. A., Effects of electric field and biaxial flexure on the failure of poled lead zirconate titanate, IEEE Trans. Ultras. Ferroelec. Freq. Contr., 55 (12), 2008, 2559-2570.
3. Wang, H., Matsunaga, T., Lin, H.-T., and Mottern, A. M., Piezoelectric and dielectric performance of poled lead zirconate titanate in electric cyclic fatigue, Start Materials and Structures, Smart Mater. Struct., 21 (2), 2012, 025009.
4. Wang, H., Cooper, T. A., Lin, H.-T., and Wereszczak, A. A., Fatigue responses of lead zirconate titanate stacks under semi-bipolar electric cycling with mechanical preload, J. Appl. Phys., 108 (8), 2010, 084107.
5. Wang, H., Wereszczak, A. A., and Lin, H.-T., Fatigue response of a PZT multilayer actuator under high-field electric cycling with mechanical preload, J. Appl. Phys., 105 (1), 2009, 014112.
6. Ferber, M. K., 2012, unpublished.

Agreement 17257: Materials for Advanced Turbocharger Designs

P.J. Maziasz and A. Shyam
Oak Ridge National Laboratory
and
K. Pattabiraman
Honeywell Turbo Technologies

Objective/Scope

This ORNL CRADA project with Honeywell, NFE-08-01671 (DOE/EERE/OVT Agreement 17257) began last year, and is scheduled to last for about 3 years. This CRADA project addresses the limitations of lifetime or use-temperature for the various components (casing, wheel, shaft, bearings) of both the turbine and compressor parts of the turbocharger system. As exhaust temperatures increase, to provide higher engine efficiency and lower emissions, turbocharger component temperatures also increase, so the need for more heat-resistant materials must be addressed. Requests for more detailed information on this CRADA project should be directed to Honeywell, Inc.

Highlights

Neutron-scattering experiments at ORNL to measure residual-stresses in critical locations of wheel/shaft assemblies and turbine housings were completed last quarter. Long-term creep-testing of cast CF8C-Plus austenitic stainless steel at 600°C continued this quarter, and aged specimen became available for testing this quarter. Assessments of the oxidation-resistance of CF8C-Plus steel relative to other exhaust component cast-irons and steels continued this quarter.

Technical Progress, 2nd Quarter, FY2012

Background

This CRADA project began last year, and will extend for 3 years, and covers several different tasks. The first task was to assess and prioritize the various components that need or would most benefit from materials upgrades to increase temperature capability and performance, as well as durability and reliability. The next tasks examine current performance and degradation modes of wheel/shaft assemblies for turbines and compressors, housings for turbines and compressors. These tasks may then obtain and test new materials with upgraded performance, and provide the results to Honeywell for designing advanced turbocharger systems, or for manufacturing of new prototype components for testing and evaluation.

Approach

This CRADA project began early last year. This project is comprised of six tasks, which will span the next 36 month period. Activity began with ORNL and Honeywell discussing the priority of the various turbocharger components for materials upgrades. A turbocharger system includes the hot (turbine) end, driven by exhaust gas from the engine, a cold (compressor) end to increase air pressure into the combustion changer, and a transition region that connects these two ends. The turbine and compressor wheels are connected to a common shaft, supported by bearings. For the first task, the turbine wheel-shaft assembly was chosen as the first component for consideration, with analysis focused on residual stresses near the weld-joint of the Ni-based superalloy wheel to the steel shaft, which can upset balance during service. Another task of this new CRADA project continues previous work between ORNL and Honeywell on testing of the new CF8C-Plus cast stainless steel as a significant performance upgrade for the turbine housings relative to standard SiMo or Ni-resist cast irons. This CRADA project for turbine housings covers a broad range of other high temperature properties, including creep and fatigue strength, and includes turbine housing applications for passenger vehicle gasoline engines.

Technical Progress

For Task 1, Honeywell identified neutron-scattering experiments to measure residual stresses in welded wheel/shaft assemblies as one of their highest priority items. For Task 2, these experiments were defined, and neutron scattering experiments at the HFIR Residual Stress User- Facility began previously. Figure 1 shows a typical Honeywell wheel/shaft assembly. Preliminary neutron-scattering experiments for diffraction analysis of the steel shaft began previously, and additional experiments on wheel/shaft assemblies with variations in processing parameters continued and were completed last quarter. The results show asymmetric tensile hoop stresses in the as-welded condition.

For Task 3, ORNL continued long-term creep-rupture tests at 600°C of the cast CF8C-Plus stainless steel this quarter, with one test at a higher stress rupturing after 7,300 h, and another test at a lower stress continuing beyond about 15,700 h. ORNL completed aging of as-cast CF8C-Plus tensile/creep specimens at 700 and 800°C to 2500 h previously, and mechanical properties testing of the aged specimens began last quarter and continued this quarter. ORNL also completed additional longer-term creep-rupture testing at 700-850°C that have been added to previous creep-rupture data on CF8C-Plus and HK30-Nb steels. Honeywell is addressing the next steps necessary to commercially produce some prototype turbocharger housing using CF8C-Plus steel for the Ford 3.5L V-6 Ecoboost engine used in light trucks. This is the next step required so that new housings can be evaluated and tested on engines.

Figure 1 – Honeywell turbocharger wheel/shaft assembly used for neutron-scattering experiments, consisting of a Ni-based superalloy turbine wheel welded to a steel shaft.

Oxidation experiments to assess the oxidation-resistance of cast CF8C-Plus relative to several cast-irons used for conventional turbochargers and exhaust system components began previously, and continued this quarter.

Communications/Visits/Travel

Periodic conference calls are held between ORNL and Honeywell Turbo Technologies, and email communications help to coordinate the work.

Status of Milestones (ORNL for DOE)

The FY2012 milestone to complete creep testing of the aged CF8C-Plus (04/2012) is complete and the milestone to extend the CRADA (08/2012) is on-track.

Publications/Presentations/Awards

None

Agreement 18571: Materials Issues Associated with Exhaust Gas Recirculation Systems

M. J. Lance, C. S. Sluder, M. K. Ferber and J. M. E. Storey
Oak Ridge National Laboratory

Objective/Scope

Provide information to industry specialists about fouling deposit properties so as to enable improved models and potential design improvements to reduce fouling and its impact on the performance of EGR (exhaust gas recirculation) coolers.

Technical Highlights

A bench-top tube reactor is being used to age deposits formed with our GM 1.9L engine. This tube reactor showed in Figure 1 was redesigned to enhance our control and to reduce leaks in the following ways:

1. The bench-flow reactor was shortened to allow both the inlet gas and the chamber to be swaged to the tube. This allowed us to remove the Marmon cap from the design which greatly reduces the heat loss between the furnace and the tube.
2. The system was sealed much better and there were no measured leaks.
3. A water pump is now being used to inject steam into the tube. This pump is far better than the bubbler system which could not maintain flow at the levels required for this experiment.

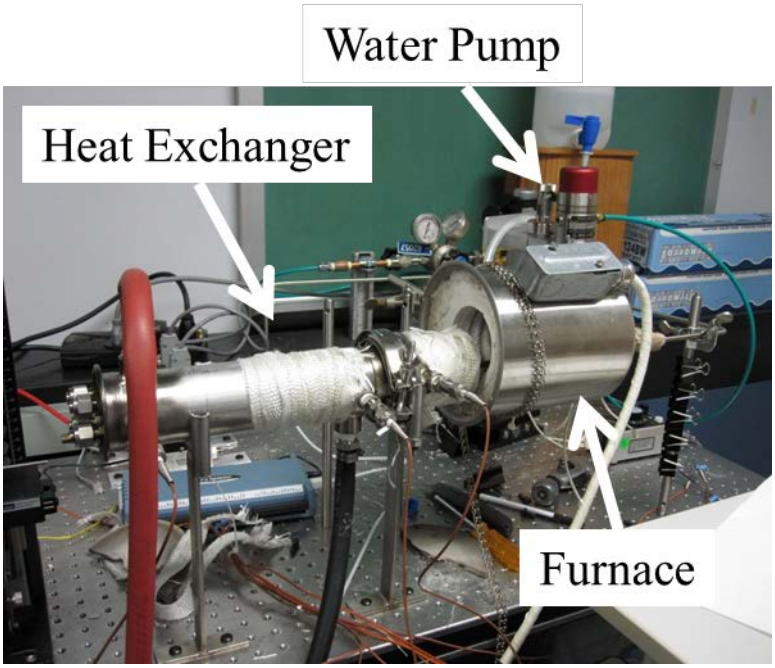

Figure 1. Bench-top tube reactor.

The effectiveness of the heat exchanger during a water condensation experiment is shown in Fig. 2. The effectiveness is equal to the temperature difference in the gas at the inlet and the outlet over the temperature difference between the inlet gas and the coolant. One-hundred percent effectiveness would mean that the heat exchanger was completely cooling the inlet gas to the coolant temperature. Here, the effectiveness starts at ~80% but after injecting 10% water, it increases to ~85%. This change is due to the water in the gas condensing on the cold metal wall (which was cooled to 10°C) and collapsing the soot porosity, thereby increasing its thermal conductivity. This experiment proves our principle that water condensation can be used as a method to refresh the EGR cooler during use by altering the deposit thermal properties.

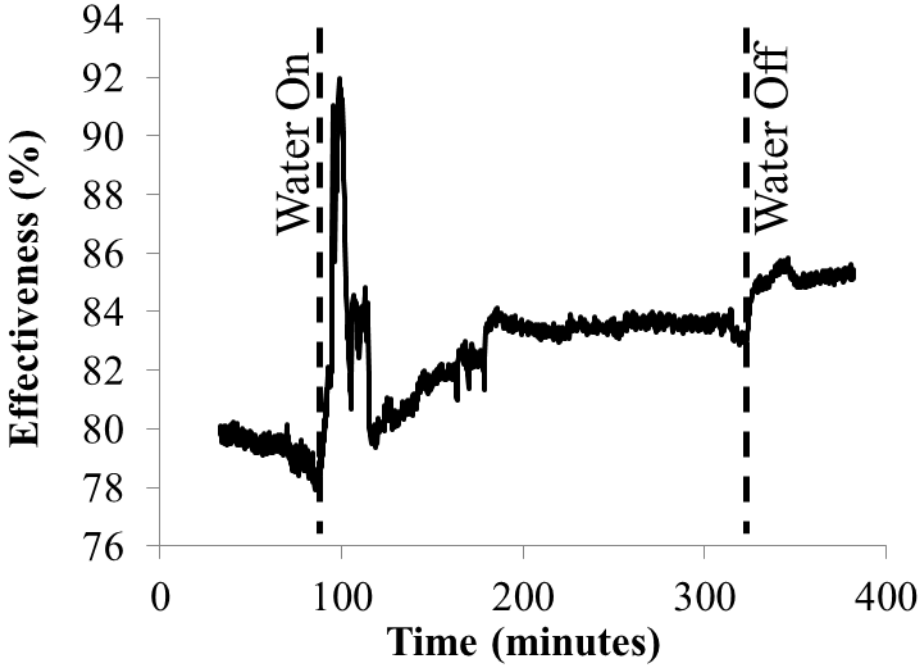

Figure 2. The effectiveness of a fouled tube during a water condensation experiment. At the end of the test, the heat transfer increased due to the removal and/or densification of the deposit.

Parallel to the controlled laboratory aging of deposits, seven coolers have arrived for the second round of forensic deposit analysis from the industry consortium of EGR technicians. Figure 3 shows the weight of the deposit relative to the surface area for both the first and second round of coolers. For the second round, more information was requested about cooler origins. These coolers tended to show the plugging failure mode from applications requiring long idling times; school buses, delivery trucks, etc. This is reflected in Fig. 3 by heavier deposit masses compared to the first round of coolers. The chemistry of microstructure of these coolers are being analyzed to better understand the operating conditions that produced these deposits, and how to prevent their formation in the future.

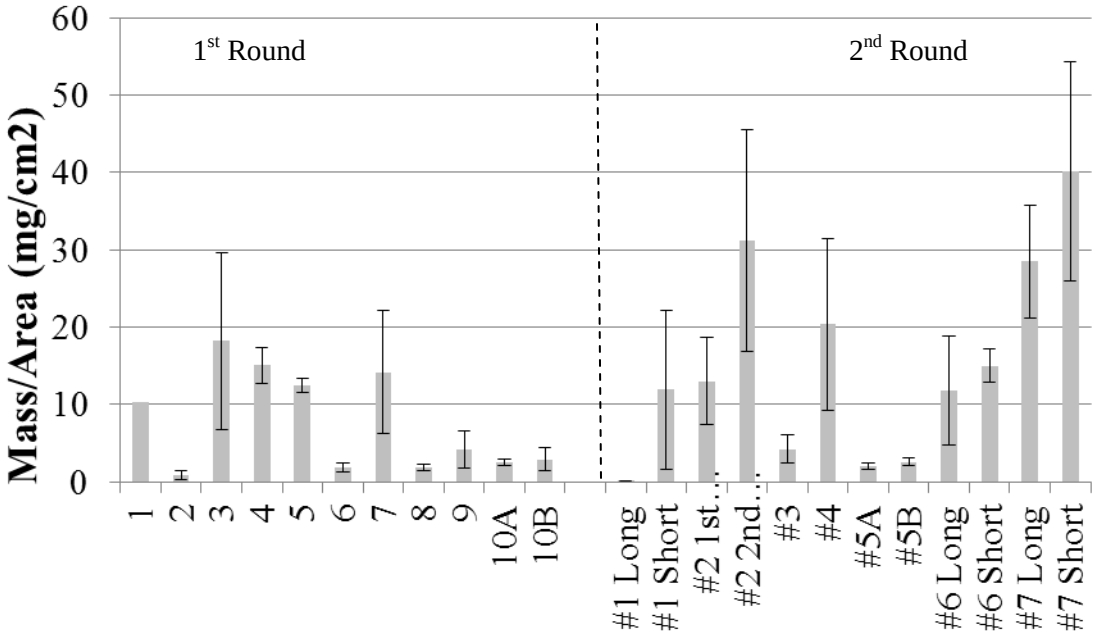

Figure 3. Mass per unit area of the industry-provided coolers. The first round of coolers is on the left and the second round is on the right.

Status of FY2012 Milestones

1. Using facilities at the High Temperature Materials Laboratory, complete forensic analysis of industry-provided EGR cooler deposits in order to enable better understanding of fouling deposits properties for specific applications (i.e., an idling school bus) so as to meet Tier 4 emission standards of 0.40 g NO_x/kWh with no efficiency penalty. **(09/12)** *On Schedule*
2. Age laboratory-generated deposits (heavy-duty and light-duty) in controlled environments to investigate changes in deposit properties with the aim of increasing the baseline thermal conductivity of 0.04 W/mK to 0.2 W/mK by condensing water and/or HC on the deposit. **(09/12)** *On Schedule.*

Communications/Visits/Travel

None

Problems Encountered

None

Publications/Presentations/Awards

Michael J. Lance, C. Scott Sluder, Matt K. Ferber, John M.E. Storey and Hassina Bilheux, "Materials Issues Associated with EGR Systems," Advanced Engine Cross-cut Team Meeting, March 15, 2012.

References

None

Agreement 9130: Catalyst Characterization

Thomas Watkins, Larry Allard, Michael Lance, Harry Meyer
Oak Ridge National Laboratory

Krishna Kamasamudram, Alex Yezerets
Cummins Inc.

Objective

The objective of this effort is to produce a quantitative understanding of the process/product interdependence leading to catalyst systems with improved final product quality, resulting in diesel emission levels that meet the prevailing emission requirements.

Goals, Barriers, Relevance & Integration

In the study area of OVT's Materials Technology subprogram, the Propulsion Materials Technology activity provides materials R&D expertise to enable advanced materials and supports the goals of several OVT subprograms.[1] Within the Advanced Combustion Engine subprogram-Combustion and Emission Control R&D activity, one primary R&D direction is to: Develop aftertreatment technologies integrated with combustion strategies for emissions compliance and minimization of an efficiency penalty. [1] Correspondingly, one *goal* is to: by 2015, improve the fuel economy of light-duty gasoline vehicles by 25 percent and of light-duty diesel vehicles by 40 percent, compared to the baseline 2009 gasoline vehicle. In support of these, this project addresses four *barriers* [1] related to the Emission Control: Lack of fundamental knowledge of advanced engine combustion regimes, improving durability and improving market perception. This project is *relevant* to this goal as the understanding of materials changes underlying the Ammonia Oxidation (AMOX) catalyst performance degradation with age increases, efficient and durable AMOX with higher NOx conversion efficiencies can be attained. This minimizes constraints on engine-out NOx emissions and allowing engines to be tuned for optimal fuel efficiency, cost and durability. This project also addresses three *barriers* [1] related to the Propulsion Materials Technology activity itself: Changing internal combustion engine combustion regimes, long lead times for materials commercialization and costly precious metal content. This project supports clean diesel, which increases acceptance by the public. Larger acceptance, in turn, results in larger percentages of conversion to diesel, with the resulting reduction in petroleum usage/dependency upon foreign oil. This project is *integrated* within Vehicle Technologies program as it utilizes characterization tools acquired and maintained by the High Temperature Materials Laboratory (HTML) Program.

Technical Highlights

The main focus in FY2012 is to begin to characterize the ammonia oxidation (AMOX) catalyst characterization of a practically-relevant zeolite catalyst, in-situ, subjected to hydrothermal aging for lifetime prediction model input. The technical approach will be as before: experimentally characterize materials, supplied by Cummins, from all stages of the catalyst's lifecycle: fresh, de-greened, aged, regenerated, on-engine and off-engine,

etc. Determinations include: crystal structure, morphology, phase distribution, particle size, surface species of catalytically active materials, atomic mechanisms and chemistry of adsorption and regeneration processes. Ultimately, an understanding of the thermal and hydrothermal aging processes and other degradation mechanisms is sought throughout the lifecycle of the catalytic material. {Acronyms are used liberally through out this report and are defined in Table I.}

New samples were hydrothermally aged for 1 and 2 h at 600, 650, 700, 800, 900°C in air with 7% H_2O to study accelerated aging. The brown zeolite and washcoat was easily separated from the cordierite substrate. A small section was collected from each sample, placed on a zero background plate and examined using XRD. Figure 1 shows a brown catalyst section from a 900°C – 2-h sample, completely separated from the cordierite substrate. A slight grey film appeared on the back side where it was attached to the cordierite substrate, while the bulk of the section has the same brown color as the outer/top surface.

Figures 2 and 3 show 3-D overlays of all the 1-h and 2-h XRD patterns, respectively. Within each figure the x-ray patterns were nearly identical and therefore appear to be independent of temperature. This suggests the material aged quite quickly above 600°C. When these data are plotted together, there was distinct difference in the two sets of patterns as seen in Figures 4 and 5, respectively. A shift in the low angle peak after 2 hours, the appearance of two new peaks and the reduction in intensity of the major peak between 23° to 24° 2θ are observed. Given their similarities independent of temperature, Figure 6 is a summation of all of the 1-h and all of the 2-h scans to assist in peak identification. The new peak near 28.5° 2θ is located where the major peak of silicon is observed, and the new peak near 24° 2θ, is located where a peak for hematite (Fe_2O_3) is observed. It is speculated that the changes in the peaks at 7.8 and 22.5° 2θ are due to dealumination of the zeolite structure. A crude Rietveld refinement of the two zeolite-beta phases was undertaken using HighScore Plus.[2] The quantitative estimates can be seen in Figures 7 and 8. Table II lists the unit cell parameters for the 1-h and 2-h summation scans in Figure 6.

Microanalysis of Cu-Zeolite SCR Catalyst Materials

Advanced electron microscopy methods are being used to characterize the structure, morphology and microchemistry of a new series of commercial copper-based zeolite selective-catalytic-reduction (SCR) catalyst materials provided by Cummins. The catalysts were provided typically as wash-coated monoliths in an as-coated or fresh condition (i.e. the monoliths had not been used or treated in any way). Six different zeolite SCR catalysts are being studied; typical results from characterization of one of the as-prepared materials, identified as “Cu-F” are given as follows. Effects of hydrothermal aging treatments at various times and temperatures on the remaining fresh materials are also being characterized and will be reported later, as appropriate.

Samples were prepared for observation in the ORNL JEOL 2200FS aberration-corrected electron microscope (ACEM), which is equipped with a Bruker-AXS silicon-drift energy-dispersive spectrometer (EDS) for analysis of the chemistry of phases

observed with scanning transmission dark-field and bright-field images. Powder was scraped from the inner surfaces of channels in a fractured section of monolith, ground and dry-dispersed onto a holey carbon film which was supported on a Be TEM grid (to minimize the contribution of Cu, an element of interest, in the EDS spectra collected). Images in the ACEM were recorded simultaneously using a high-angle annular dark-field (HAADF) detector and a bright-field (BF) detector. The HAADF images show contrast related primarily to atomic number, where the high atomic number (Z) species are brighter in contrast, with the contrast related roughly to Z^2.

Figure 9 shows HAADF-BF images of the general morphology of the Cu-F zeolite sample. There are two distinctly different characteristics of the powder: one component is composed of rounded, equiaxed particles 50-150nm in size with generally smooth surfaces, such as the area shown in the inset box A, and the second major component is a very fine-grained aggregation of nanoparticles such as the area shown in the inset box B. This area was used to generate a “hypermap” of EDS data for further compositional analysis. The hypermap generates individual spectra, pixel by pixel, so that any area of the hypermap selected, after its accumulation, will show the sum of all the spectra within the area. This allows *a posteriori* determination of the elemental distributions in chosen areas. The hypermap data for a selected group of elements is shown in Figure 10. General inspection of the individual elemental maps suggests that the rounded particles are primarily an alumino-silicate composition, and the fine powder contains Zr as well as Al and Si. These results are consistent also with the spectra generated from the areas A and B in Figure 9, and shown in Fig. 11a and 11b. The high Si-O peaks in area B likely are contributed to some extent by excitation of the nearby bulkier aluminosilicate particles, but there is also the potential that some fraction of the fine particulate, likely ZrO_2, phase also has a silica component. Mo in the spectrum is a system contaminant, probably from Mo in the collimator of the silicon drift detector system. The Cu hypermap suggests an overall distribution of Cu in the aluminosilicate particles, but this might also originate from spurious x-rays generated by electron scattering onto Cu-bearing components of the microscope. To test this, we used the same specimen holder and a Be grid with SiO_2 particles, and collected the spectrum shown in Figure 11c. The spectrum was collected from 1-10 keV in energy, and so is adjusted relative to the spectra from areas A and B to match the energy scales. It also shows a small Cu peak, the height of which relative to Si is lower than the Cu peak from area B, but about the same as the Cu peak from Area A. This suggests that there is a component of Cu, likely Cu oxide, also in the fine powder material. But since the hypermap of Cu shown in Figure 10 indicates the possible presence of Cu in (or on) the bulk aluminosilicate particles, another powder area was analyzed.

Figure 12 shows a HAADF-BF image pair of a nearly “clean” aluminosilicate particle. Several bright spots clearly seen in profile on the surface are indicated by arrows, indicating heavy metal species. Two of the bright spots are labeled Cu, as they match the hypermap data shown in Figure 13, which indicates a non-uniform concentration of both Zr and Cu on (or in) the particle. The Cu concentrations on the surface corresponding to those labeled in Figure 12 are also shown by arrows on the ADF

image and Cu map of Figure 13. Since the fine powder phase is primarily Zr-based, it is logical that the Zr distribution shown in Figure 13 on the aluminosilicate particle is primarily on the surface. Cu is not in a uniform dispersion throughout the particle, and it is reasonable to presume that Cu is present as an oxide species also primarily on the surface of the zeolite, particularly since Cu species can be positively identified on the surface as per Figure 13. These results are an example of the kinds of information available on the structure, chemistry and morphologies seen in the set of commercial zeolite SCR catalysts presently being analyzed on the CRADA project.

Status of FY 2012 Milestones

In the reporting period, the ORNL team continued characterizing an ammonia oxidation (AMOX) catalyst characterization of a practically-relevant zeolite catalyst subjected to hydrothermal aging for lifetime prediction model input. We will begin in-situ ammonia oxidation (AMOX) catalyst characterization of a practically-relevant *zeolite catalyst* subjected to hydrothermal aging at elevated temperatures for lifetime prediction model input using x-ray diffraction or piezospectroscopy (09/2012).

Communication/Visits/Travel

Email and telephone conversations as needed.

Publications/Presentations/Awards

None.

References

1. Vehicle Technologies Program, Multi-Year Program Plan 2011-2015, Dec 2010, pp. 2.3-1, 2 ; 2.5-8.
2. High Score Plus (2009). High Score Plus, version 3.0 (computer software), PANalytical B.V., Amelo, The Netherlands.

Table I. Acronyms

AMOX	ammonia oxidation
BF	bright-field
EDS	Energy dispersive spectroscopy
HA-ADF	high-angle annular dark-field
HTML	High Temperature Materials Laboratory
NOx	Nitrogen and Oxygen containing compounds
ORNL	Oak Ridge National Laboratory
STEM	Scanning Transmission Electron Microscopy
XPS	X-ray photoelectron spectroscopy
XRD	X-Ray Diffraction

Table II. A list the refined unit cell parameters for the 1-h and 2-h scans.

Sample	Compound	Wt %	Space Group	a	b	c
				α	β	γ
Summation of 1-h Scans	Zeolite beta Monoclinic	52	Monoclinic	17.606	17.656	14.336
			C 1 2/c 1 (15)	90	113.84	90
	Zeolite beta Tetragonal	48	Tetragonal	12.464	12.464	26.223
			P 41 2 2 (91)	90	90	90
Summation of 2-h Scans	Zeolite beta Monoclinic	38	Monoclinic	17.547	17.620	14.369
			C 1 2/c 1 (15)	90	113.76	90
	Zeolite beta Tetragonal	40	Tetragonal	12.438	12.438	26.166
			P 41 2 2 (91)	90	90	90
	Hematite Fe_2O_3	10	Rhobohedral	5.029	5.029	13.79
			R -3 c (167)	90	90	90
	Silicon	12	Cubic	5.429	5.429	5.429
			F d -3 m (227))	90	90	90

Figure 1 – The brown catalyst section separated from the cordierite surface for sample AMOX2 900°C – 2 h and was collected for XRD examination. The slight grey on the brown scale is where it was attached to the cordierite surface, while the brown surface is the outer surface as seen when attached to the tan cordierite substrate.

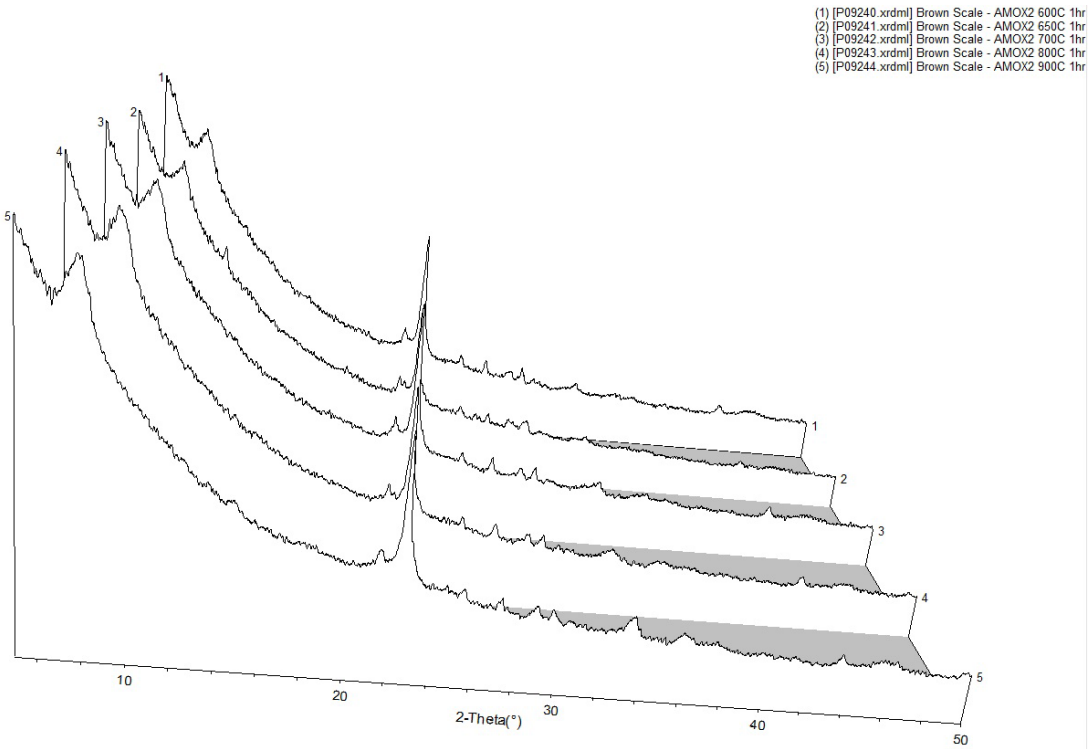

Figure 2 – A 3-D overlay of all the one hour XRD patterns sorted by temperature as seen in the key at top right.

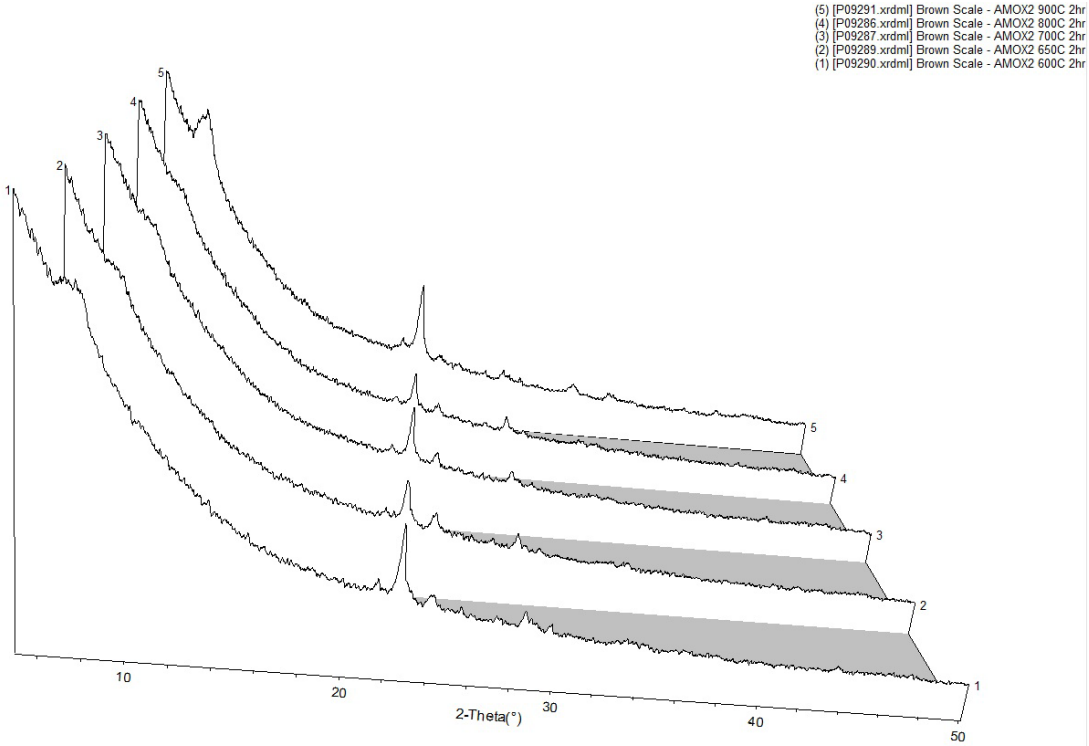

Figure 3. A 3-D overlay of all the two hour XRD patterns sorted by temperature as seen in the key at top right.

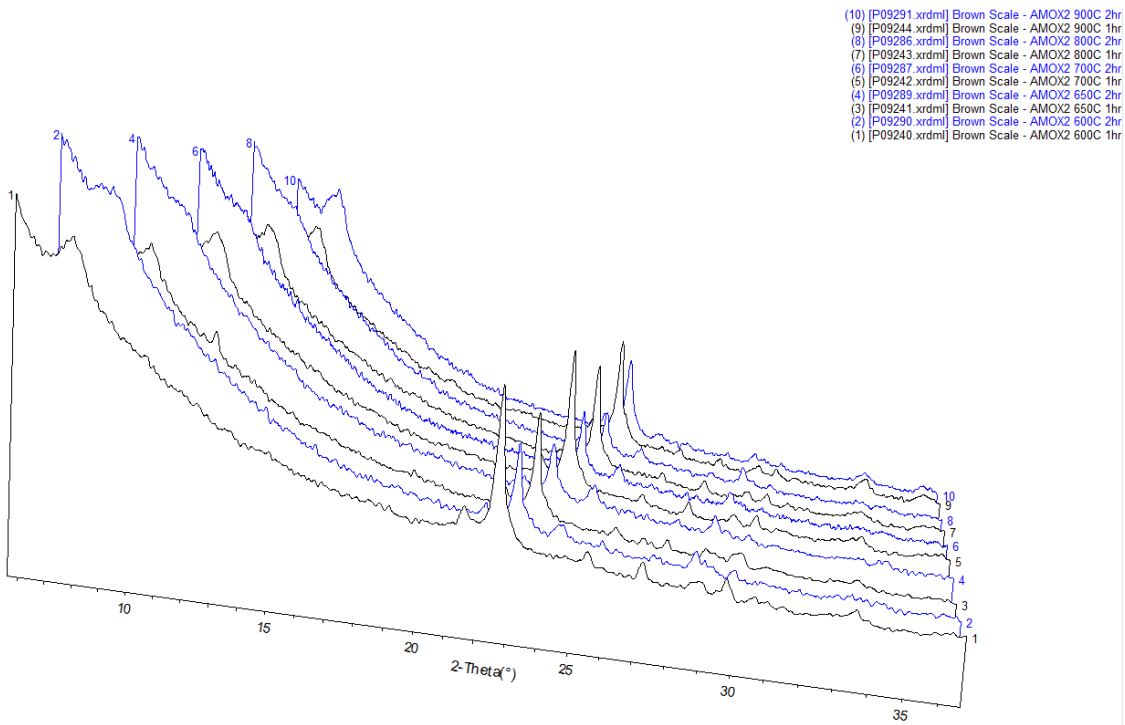

Figure 4. A 3-D overlay of all the XRD patterns sorted by time (one hour black and two hour blue) and temperature as seen in the key at top right.

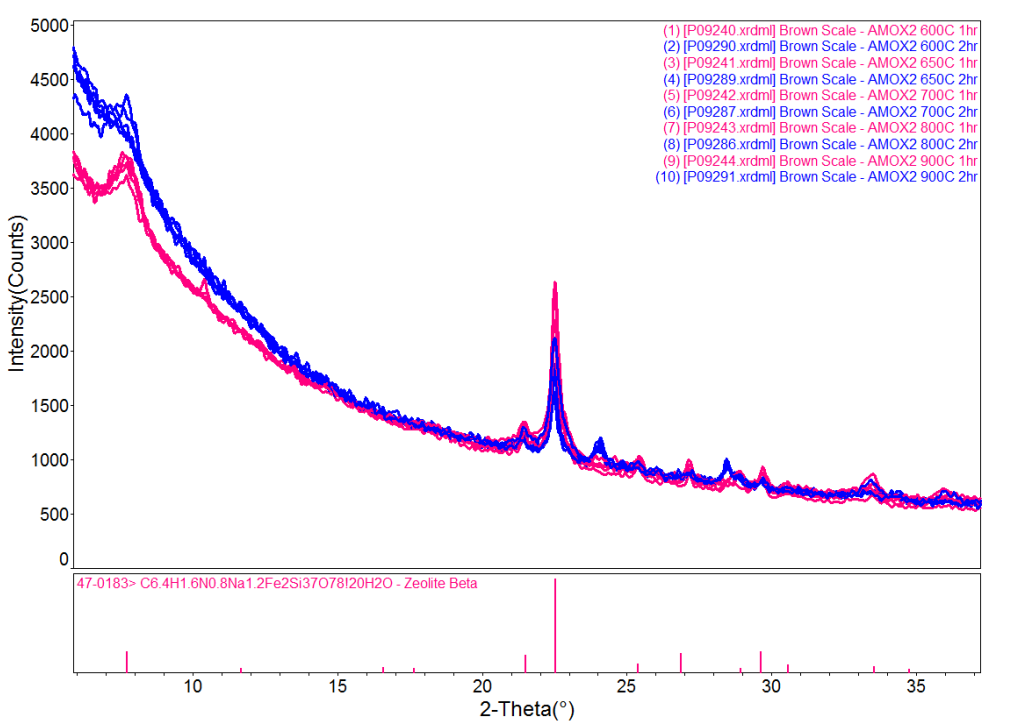

Figure 5. All the XRD patterns were plotted together with the location and intensity for Zeolite-beta. The 1-h patterns (red) and the 2-h patterns (blue) highlight the similarity of the 1-h and 2-h patterns to each other while a slight difference between the sets can be seen.

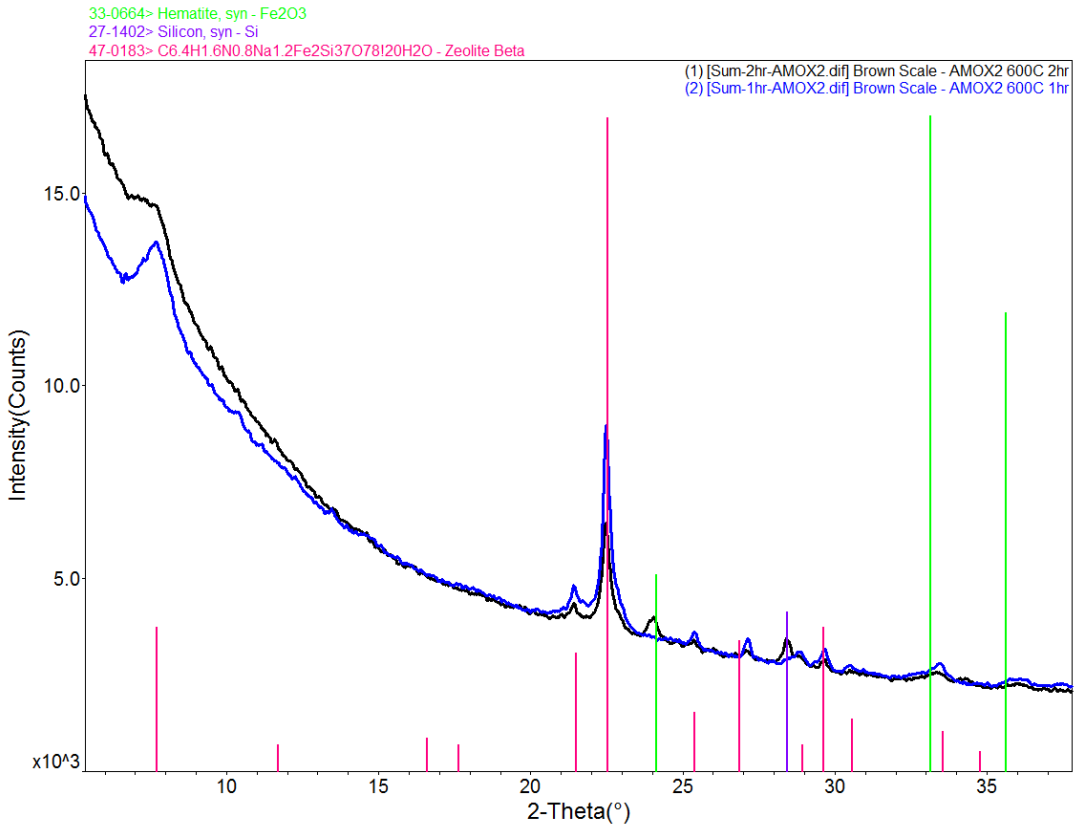

Figure 6. The location and intensity for Zeolite-beta (red), silicon (purple) and hematite (green) are superimposed on a plot of summations of the 1-h (blue) and the 2-h (black) scans. The changes between the one and two hour sets can be seen to correspond with the location of major peaks of silicon, a peak of hematite and zeolite-beta.

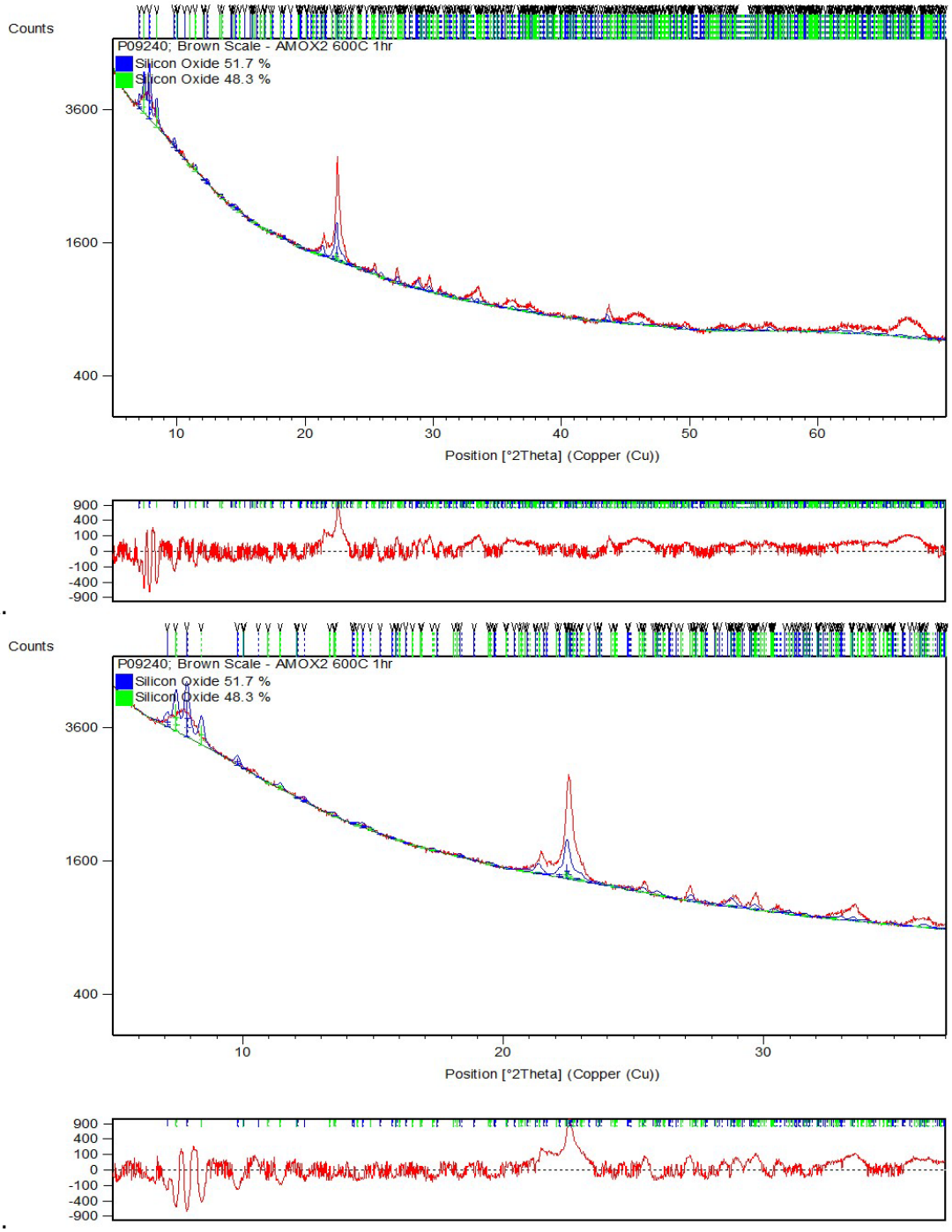

A.

B.

Figure 7 – A. For the summation of the 1-h scans, the calculated structure refinement (blue line – calculated pattern) is plotted along with the observed XRD data (red) in the top section. In addition, the location of the refined peak position is marked with the same colored lines as noted in the color key. The difference between the observed and calculated patterns (red) is plotted in the bottom portion of the figure. B. An enlargement of A in the low 2θ region.

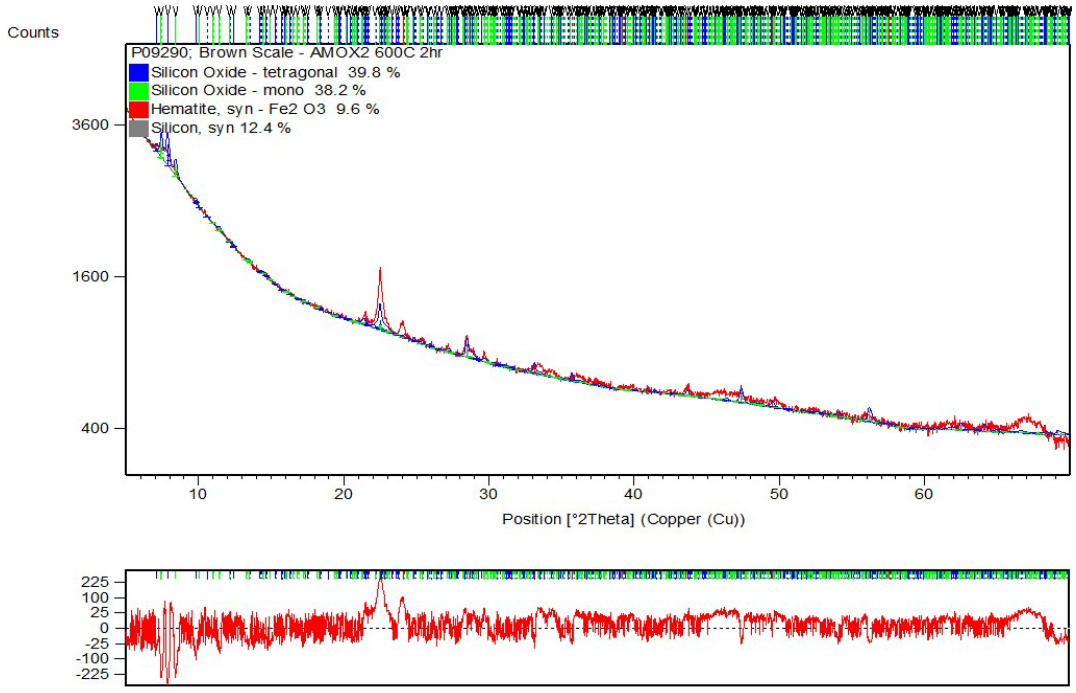

A.

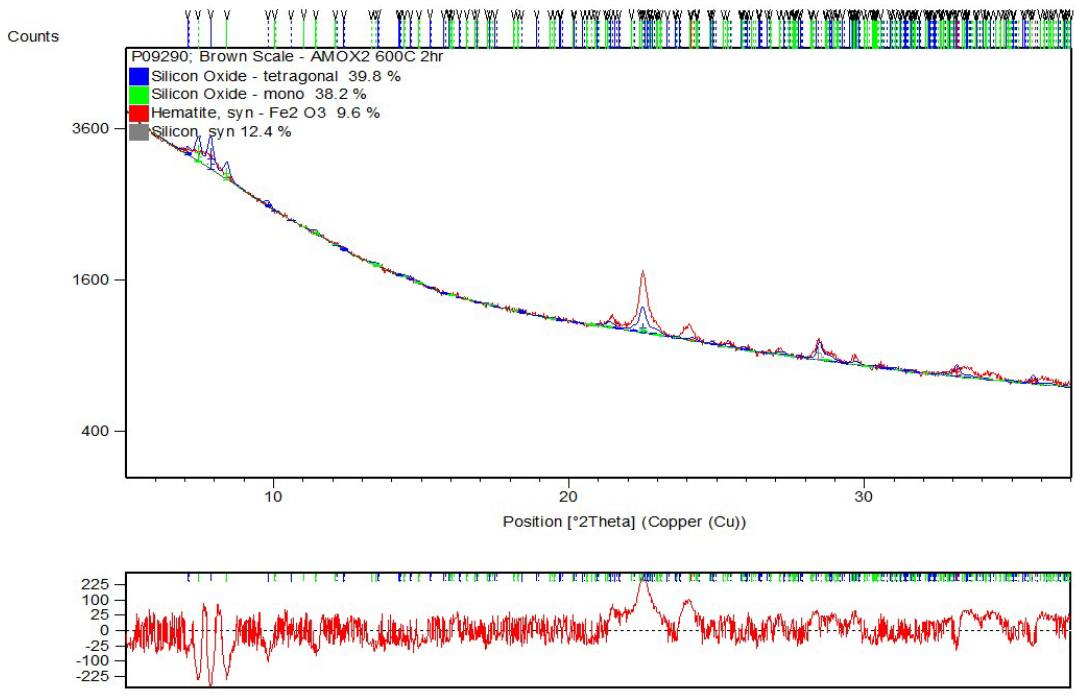

B.

Figure 8 – A. For the summation of the 2-h scans, the calculated structure refinement (blue line – calculated pattern) is plotted along with the observed XRD data (red) in the top section. In addition, the location of the refined peak position is marked with the same colored lines as noted in the color key. The difference between the observed and calculated patterns (red) is plotted in the bottom portion of the figure. B. An enlargement of A in the low 2θ region.

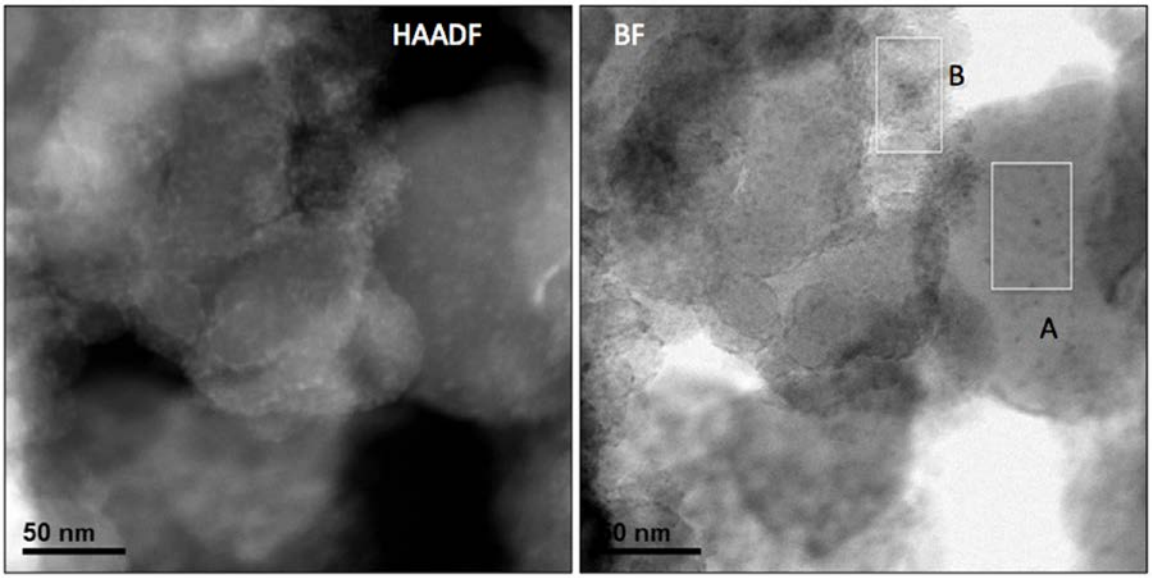

Figure 9 – HAADF-BF image pair showing general morphology of the Cu-F zeolite SCR catalyst. Smooth, equiaxed particles and a very fine-grained particulate aggregate are indicated in areas A and B, respectively. These areas were used to generate the spectra shown in Figure 11, acquired from the hypermap of this area shown in Figure 10.

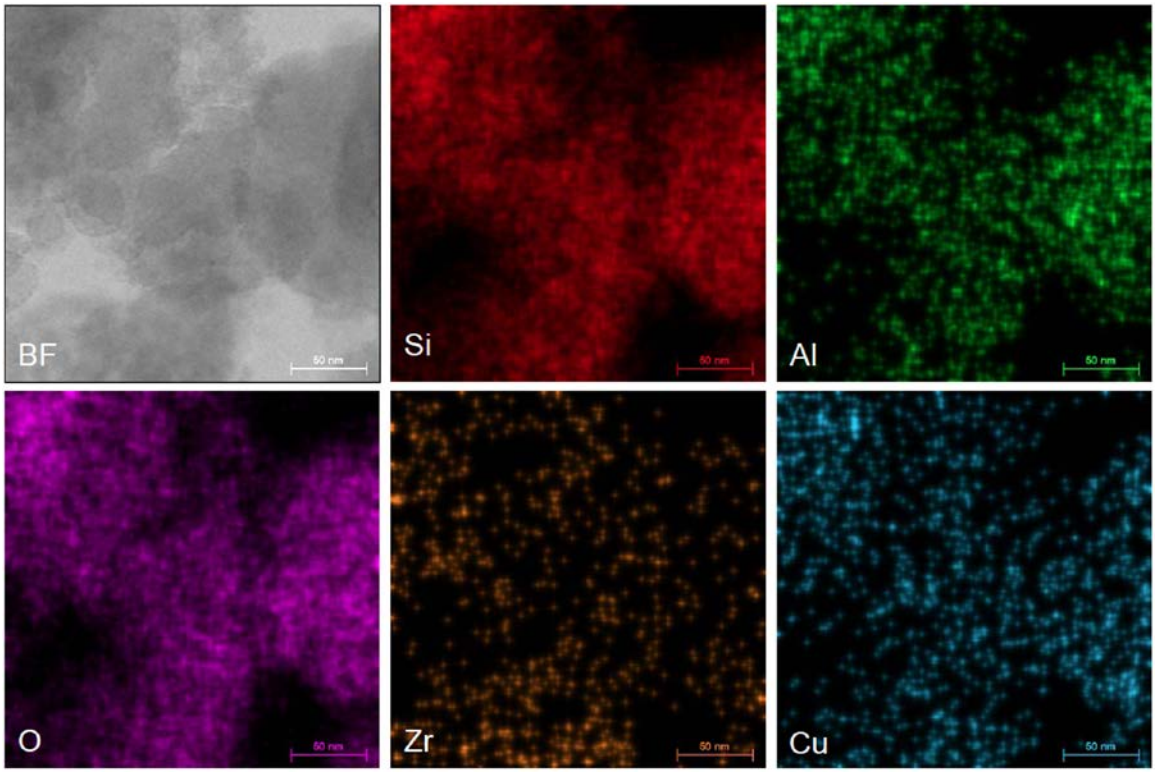

Figure 10 – Hypermap data from the area of the Cu-F catalyst shown in Figure 9. Spectra shown in Figure 11 were generated from analysis areas A and B, representing the two distinctive morphologies in this catalyst.

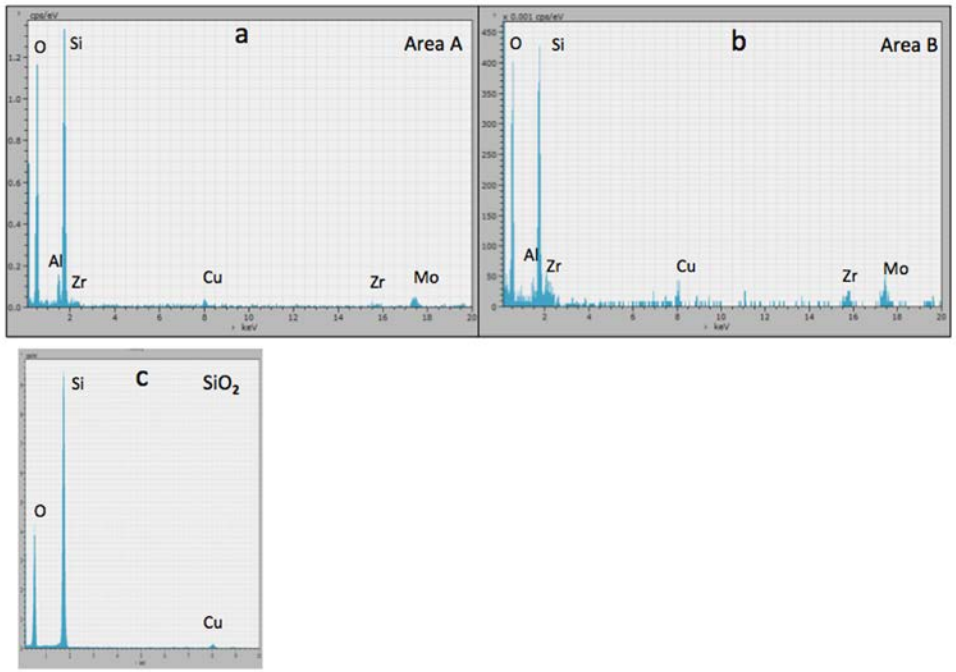

Figure 11 – a) and b) represent spectra generated from the inset areas A and B, respectively, in Figure 10. c) is a spectrum from a particle of SiO_2, and shows the residual Cu peak that is due to excitation of microscope column components. Area B shows significant Zr relative to the smooth aluminosilicate particle of area A, and some Cu apparent also. Additional data on the distribution of Cu and Zr is shown in the next figures.

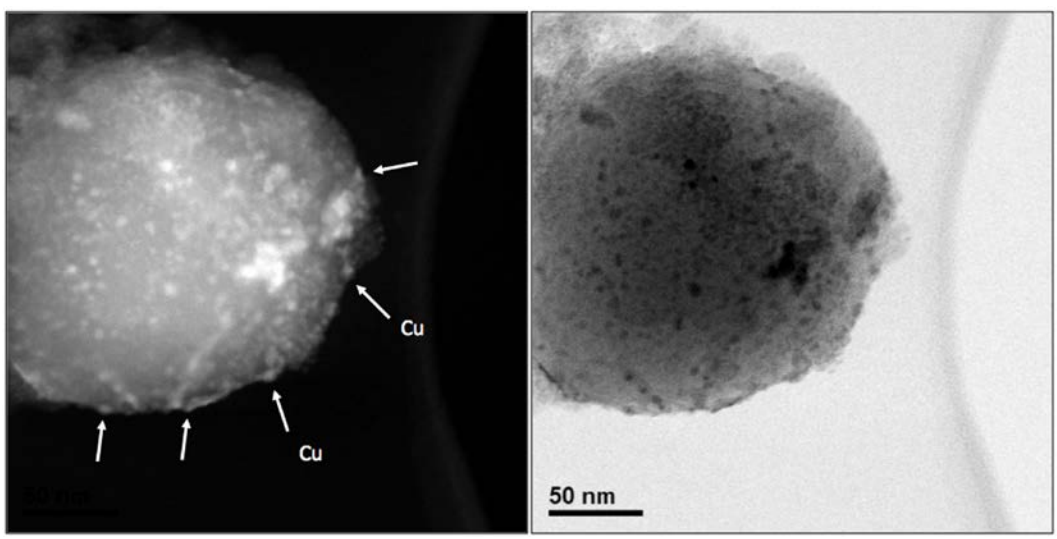

Figure 12 – HAADF-BF images of an isolated aluminosilicate particle, showing heavy metal species in bright contrast in the HAADF image. In the transmitted electron image, only species on the edge of the particle and seen in profile, such as at the arrows, can conclusively be determined to be on the surface of the particle. The hypermap shown in Figure 13 allows identification of Cu on the surface in the spots labeled.

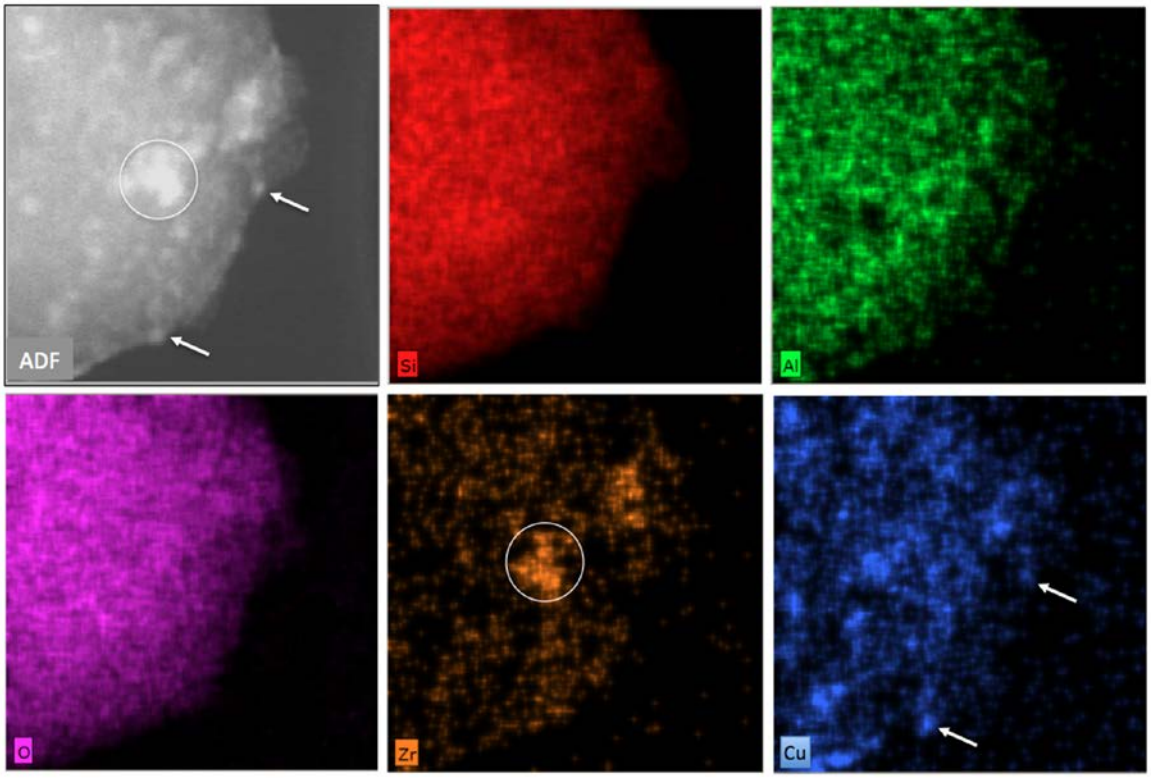

Figure 13 – Hypermap data from the particle of Figure 12. The non-homogeneous distribution of Zr and Cu on the surface is evident. Arrows locate at least two Cu-rich particles on the surface, and the circles show significant Zr present, likely also on the surface.

Agreement 10461: Durability of Diesel Engine Particulate Filters

Thomas R. Watkins, Amit Shyam, Hua-Tay Lin, Edgar Lara-Curzio
Oak Ridge National Laboratory

Randall J. Stafford
Cummins, Inc.

Objective

The objective of this effort is to identify and implement test techniques to characterize the physical and mechanical properties of ceramic diesel particulate filters (DPFs), to identify the mechanisms responsible for the degradation and failure of DPFs and to develop analysis tools for predicting their reliability and durability.

Goals, Barriers, Relevance & Integration

In the study area of OVT's Materials Technology subprogram, the Propulsion Materials Technology activity provides materials R&D expertise to enable advanced materials and supports the goals of several OVT subprograms.[1] Within the Advanced Combustion Engine subprogram-Combustion and Emission Control R&D activity, one *goal* is to: by 2015, develop materials, materials processing, and filter regeneration techniques that reduce the fuel economy penalty of particle filter regeneration by at least 25 percent relative to the 2008 baseline. This project addresses five *barriers* [1] related to the Emission Control: Lack of cost-effective emission control, improving durability and improving market perception. This project also addresses two *barriers* [1] related to the Propulsion Materials Technology activity itself: Changing internal combustion engine combustion regimes and costly precious metal content. This project is *relevant* to the above goal as the understanding of the relationships of the material properties for the filter (and catalyst) substrates enables optimization of porosity, strength, elastic modulus, thermal conductivity, thermal expansion, etc. leading to improved materials processing and models and optimized regeneration strategies that improve fuel economy and increase DPF life. This project supports clean diesel, which increases acceptance by the public. Larger acceptance, in turn, results in larger percentages of conversion to diesel, with the resulting reduction in petroleum usage/dependency upon foreign oil. This project is *integrated* within Vehicle Technologies program as it utilizes characterization tools acquired and maintained by the High Temperature Materials Laboratory (HTML) Program.

Technical Highlights

In the reporting period, the ORNL team continued characterizing a new SiC-based DPF material. The DPF honeycomb monoliths were sectioned, and samples were machined as before.[2] The x-ray diffraction pattern of powder from a crushed piece of the SiC-based material shows four phases present: 6H-SiC, 15R-SiC, free Si, and cristobalite (a tetragonal form of SiO_2, see Figure 1). A quantitative XRD analysis was performed using the Reitveld method (see Table I). Since ~20 v% of the solid (excluding porosity) is silicon (8.3 v% Si if porosity is included), this material can be considered a siliconized silicon carbide (Si/SiC) or a reaction-bonded silicon carbide (RBSC).

The measured properties of this SiC-based material is listed and compared to literature references in Table II. The skeletal densities are all within 13% of the dense literature reference values, indicating that there is at most 13 % closed porosity. The skeletal density of the SiC based material will obviously vary with free Si content and is comparable to values for reaction-bonded silicon carbide (RBSC). In Table II, the Young's moduli are quite low relative to the values for dense materials, which is directly related to the high porosity. There is some variability (factors 2-4X) of Young's moduli values amongst the available measurement techniques: load deflection, resonant ultrasound spectroscopy (RUS), pulse echo and dynamic mechanical analysis (DMA, reported here). Understanding this variability is the subject of an on-going study.

Double torsion fracture toughness testing was performed at RT, 300, 500, 800 and 900 °C as described elsewhere.[2] The double torsion plate samples were sectioned from larger monoliths (see Figure 2) and were 40 x 20 mm (L x W) in size. The sample thicknesses were governed by the starting wall thickness of the honeycomb monoliths; after machining, typical double torsion sample thicknesses was ~0.28 mm for the SiC-based materials. Figure 3 shows the experimental set-up of the double torsion testing. The sample is carefully mounted in the double torsion jig; the jig with sample is then gingerly lowered into position within the furnace. The tube and much of the insulation is in place prior to the required precracking. Needless to say, some dexterity is required in performing this work. A successfully fractured test specimen is defined as one where the crack propagates to the opposite/far end of the sample and is displayed in Figure 4. The fracture surfaces of successfully tested double torsion samples were examined using the SEM (see Figures 5-7). In examining these micrographs, it is often difficult to discern pre-fracture/pre-existing surfaces from post-failure fracture-related surface features. During sample machining, the samples were held with a vacuum chuck for dry grinding which likely pulls in grinding debris. As such, a lack of debris highlights fracture sites on internal ligaments/struts. The fracture features of Figures 5-7 do not look appreciably different; the Si/SiC is fracturing transgranularly without any ligamentation. Unlike the double torsion fracture surfaces of the cordierite and AT-based materials, which possessed numerous microcracks, the SiC-based material had only an occasional microcrack. These are thought to originate from the fracture process itself. Oxidation/glass formation is evident at the highest temperatures, particularly in the BSE images (see Figure 7). The total testing time above 100°C varies for each sample and temperature but is somewhere between 3-8 hours.

Figure 8A shows typical the fracture behavior in the double torsion experiments. The double torsion method was selected to measure apparent fracture toughness as crack length not needed for determination.[12] This is important given the large amount of engineered porosity and honeycomb structure as well as microcracks in the DPF materials. Here, the maximum load was used to calculate K_{IC}. The non-zero start-finish of K_I is due to weight of the double torsion jig top, which pre-loads the sample, and is included in the K_{IC} calculation. The slopes in Figure 8A suggest that the moduli are the same or slightly lower at elevated temperature. In Figure 8B, the average fracture toughnesses, K_{IC}, are shown to increase with testing temperature. It can be seen that there is a significant difference between the RT value and the 800 or 900°C

values. In contrast, the increase in temperature had a negligible effect on the fracture toughness of cordierite and AT-based DPF materials. It is speculated that the mechanism for this increase in toughness is due to increased ductility of the free Si nodules.

In the RBSC and Si/SiC literature, reports of strength and toughness increasing with temperature are common for dense materials with volume fractions of free silicon ranging from 8 to 49 v% tested at temperatures greater than 1000°C. For example, Huang and Zhu[6] observed increases in strength and fracture toughness of RBSC starting at 1000°C and continuing to 1330°C. They observed that the material was transitioning from transgranular to intergranular failure and speculated that this was due to a change in the bond strength between the Si and SiC grains. Various toughening mechanisms have been attributed to the observed strength and toughness increases with temperature, but all ultimately originate in the plastic/softening behavior of free Si. These mechanisms include crack tip blunting or healing,[13,14] stress redistribution due to grain cluster movement,[13-18] grain boundary softening or sliding,[6,15-17,19,20] creep cavitation (hard to see in highly porous DPF materials),[13-17] oxidation and/or possibly glass formation to close or fill in cracks/flaws.[6,21] These behaviors are dependent upon volume fraction of Si, temperature, time at temperature and stress level.[13,14,22]

In a simple experiment, half of a double torsion specimen was dead loaded, heated up to 900°C for 24 hours then furnace cooled. Upon removal from the furnace the sample was permanently bent, confirming some sort of creep or deformation had occurred. Subsequent SEM work did not find any definitive surface features (e.g. ligamentaion nor stretched Si nodules) suggesting a toughening mechanism. Likewise, XRD pattern did not display any evidence of a glassy phase. In the absence of significant amounts of a glassy phase and the fact that SiC is a refractory material, it would appear that the permanent deformation, and perhaps the toughness increase, is related to the free silicon.

Dynamic fatigue testing was also conducted on the SiC-based DPF material. In static fatigue, samples are simply loaded with a constant stress (e.g., dead weight) and monitored for time to failure (see Figure 10). Dynamic fatigue provides an accelerated means, relative to static fatigue, to evaluate the mechanical reliability of ceramics[23-25] and is shown schematically in Figure 10. Fast fracture is considered to be inert as there is not enough time for strength degradation mechanisms to occur. As the loading/stressing rate slows, environmental factors, such as stress assisted corrosion cracking, can occur resulting in slow crack growth (SCG). As such, dynamic fatigue is used to evaluate time and environmentally dependent mechanisms, such as SCG, strength degradation, creep effects, oxidation effects as well as checking repeatability. Figure 11 schematically shows a dynamic fatigue curve plotting the natural log of the failure strength as a function of the stressing rate. The slope of this line is equivalent to 1/(N+1). When N is large, the material does not exhibit susceptibility to SCG. As N decreases, the SCG susceptibility of the material increases. N can be use to estimate the static fatigue lifetime, t_{est_df}, as follows:

$$t_{df} = \frac{\sigma_f}{\dot{\sigma}} \ .$$

Substituting N and t_{df} into:

$$t_{est_sf} = \frac{t_{df}}{(N+1)} \ .$$

The dynamic fatigue curves for the SiC-based material are shown in Figure 12 for two different specimen cross-sections/sizes: 4 cells (6.5 mm) x 3 cells (4.8 mm) x 50 mm and 6 cells (9.5 mm) x 3 cells (4.8 mm) x 50 mm. Above 800°C, an apparent stressing rate affect is evident as the fracture strength increases approximately 35-45% when tested at 0.003 MPa/s relative to the faster rate of 3 MPa/s. This is atypical. Normally, the strength either remains constant (no environmental effect) or decreases with slower stressing rates due to the extra time allowing environmentally assisted mechanism to occur. Further when tested at 0.003 MPa/s, the strength data at 800 and 900°C are consistently stronger than the 600°C data suggesting some sort of thermally activated strengthening mechanism. In support of this observation, Figure 13 is taken from an extensive study of ceramic turbine materials by Larsen and Adams,[19] which shows the fracture strength of Si/SiC increasing with testing temperature up to ~1200°C. Other researchers[6,13,14,18,20,21] have observed this as well and attributed to varied strengthening mechanisms as discussed above. No specimen size affect was observed for the cross-sections examined. Figures 14 and 15 show the fracture surface microstructures of the samples tested at 600 and 900°C with a stressing rate of 0.003 MPa/s. As before with the double torsion samples, the surfaces look similar showing the engineered porosity and free Si nodules. However, a glassy or glazed appearance of the fracture surface from the sample tested at 900°C, 0.003 MPa/s indicates that extensive oxidation has occurred. Some of the glass appears to have cracked. The high magnification view in Figure 14 indicates that a small amount of oxidation has occurred. As discussed above for fracture toughness, the crack blunting due to the plastic behavior of the free Si metal and/or oxidation of the Si and SiC is thought to be the root mechanism for the observed strength increase with testing temperature.

Status of FY 2011 Milestones

In the reporting period, the ORNL team continued the determination of strength, fracture toughness, density/porosity/microstructure, and thermal expansion of uncoated DPFs as a function of time at elevated temperatures of 300, 500, 800 and 900°C for a second alternate substrate DPF material (SiC). Dynamic fatigue of samples tested at 0.000003 MPa/s will be conducted soon.

Travel

ORNL and Cummins personnel traveled to Daytona Beach, FL for a meeting of the ASTM C28.01 Mechanical Properties and Reliability committee on January 22, 2012, which, in part, provides standards for the DPF community. On the same trip, an *invited* technical talk was presented by T.R. Watkins at the 36th International Conference on Advanced Ceramics and Composites Meeting, Daytona Beach, FL, January 24, 2012.

Presentations

Invited Presentation: T.R. Watkins, K.J. Wright, A. Shyam, H.T. Lin, M.K. Ferber, R. Stafford, “Fracture Toughness and Dynamic Fatigue of Porous SiC at Elevated Temperature,” presented at the 36th International Conference on Advanced Ceramics and Composites Meeting held in Daytona Beach, FL, January 24, 2012.

RELATED Presentation**: R. J. Stafford, K. Golovin, A. Dickinson, T. R. Watkins, A. Shyam, “Elastic Modulus of Porous Cordierite by the Flexure Test Method Compared to Sonic/Resonance Test Methods,” presented at the 36th International Conference on Advanced Ceramics and Composites Meeting held in Daytona Beach, FL, January 24, 2011. **(Work funded by the HTML User Program).

References:

1. Vehicle Technologies Program, Multi-Year Program Plan 2011-2015, Dec 2010, pp. 2.3-4, -5, -8; 2.5-7, -8, -9, -10.
2. A. Shyam, E. Lara-Curzio, T. R. Watkins and R. J. Parten, “Mechanical Characterization of Diesel Particulate Filter Substrates,” *J. Am. Ceram. Soc.*, **91** [6] 1995–2001 (2008).
3. ASTM D3766, Standard Terminology Relating to Catalysts and Catalysis, ASTM International, West Conshohocken, PA 2008.
4. CRC Handbook of Chemistry and Physics, Edited by R. C. Weast, CRC Press, Inc., Boca Raton, FL 33431, p. B-121.
5. S. Aroati, M. Cafri, H. Dilman, M.P. Dariel, N. Frage, “Preparation of reaction bonded silicon carbide (RBSC) using boron carbide as an alternative source of carbon,” J. Euro. Ceram. Soc. 31 841–845 (2011).
6. Q-W. Huang and L-H. Zhu, "High-temperature strength and toughness behaviors for reaction-bonded SiC ceramics below 1400 °C," Mat. Let. **59** 1732–5 (2005).
7. T. R. Watkins, D. J. Green, and E. Ryba, "Determination of Young's Modulus in Chemically-Vapor-Deposited SiC Coatings," *J. Am. Ceram. Soc.*. **76** [8] 1965-68 (1993).
8. P. G. Karandikar, G. Evans, S. Wong S, M. K. Aghajanian, M. Sennett, "A Review of Ceramics for Armor Applications," pp. 163-175 in Advances in Ceramic Armor IV, Ceramic Engineering and Science Proceedings, V. 29 [6]. Edited by L.P. Franks, T. Ohji, A. Wereszczak, Wiley, Hoboken, NJ 2009.
9. T. R. Watkins and D. J. Green, "Fracture Behavior of Chemically-Vapor-Deposited SiC-Coated Graphite: I, Experimental Results," *J. Am. Ceram. Soc*. **76** [12] 3066-72 (1993).
10. P. Columbo, V. Sglavo, E. Pippel, J. Woltersdorf, "Joining of Reaction-Bonded Silicon Carbide Using a Preceramic Polymer," J. MAT. SCI. **33** 2405-2412 (1998).
11. C.J. Luis, I. Puertas, G. Villa, "Material Removal Rate and Electrode Wear Study on the EDM of Silicon Carbide," J. Mat. Proc. Tech. **164–165** 889–896 (2005).

12. A. Shyam and E. Lara-Curzio, “The Double-Torsion Testing Technique for Determination of Fracture Toughness and Slow Crack Growth Behavior of Materials: A Review,” J. Mater. Sci **41** 4093–4104 (2006).
13. D. F. Carroll and R. E. Tressler, “Time-Dependent Strength of Siliconized Silicon Carbide under Stress at 1000° and 1100°C,” *J. Am. Ceram. Soc.,* **68** [3] 143-146 (1985).
14. T. Darroudi, R. E. Tressler and M. R. Kasprzyk, “Low-Cost Melt-Formed Siliconized Silicon Carbide Radiant Tube Materials,” *J. Am. Ceram. Soc.*, **76** [1] 173–79 (1993).
15. S. M. Wiederhorn, D. E. Roberts, T-J. Chuang and L. Chuck, “ Damage-Enhanced Creep in a Siliconized Silicon Carbide: Phenomenology,” *J. Am. Ceram. Soc.*, **71** [7] 602-608 (1988).
16. B. J. Hockey and S. M. Wiederhorn, “Effect of Microstructure on the Creep of Siliconized Silicon Carbide,” *J. Am. Ceram. Soc.,* **75** [7] 1822-30 (1992).
17. B. A. Fields and S. M. Wiederhorn, “Creep Cavitation of a Siliconized Silicon Carbide Tested in Tension and Flexure,” *J. Am. Ceram. Soc.,* **79** [4] 977-86 (1996).
18. K. Breder, “Time-Dependent Strength Degradation of a Siliconized Silicon Carbide Determined by Dynamic Fatigue,” *J. Am. Ceram. Soc.*, **78** [10] 2680-84 (1995).
19. D. C. Larsen and J. W. Adams, “Property Screening and Evaluation of Ceramic Turbine Engine Materials,” Technical Report AFWAL-TR-83-4141, Materials Laboratory, Wright-Patterson AFB, Ohio, (1983).
20. D. C. Larsen, “Property Screening and Evaluation of Ceramic Turbine Engine Materials,” Technical Report AFML-TR-79-4188, Air Force Materials Laboratory, Wright-Patterson AFB, Ohio (1979).
21. W. J. Tomlinson, S. Khela, C. A. Jasper and S. J. Matthews, “Flexural Strength of Lapped and Oxidized Siliconized Silicon Carbide,” *J. Mat. Sci.,* **27** 3372-78 (1992).
22. O. P. Chakrabarti and P. K. Das, “High Temperature Load-Deflection Behaviour of Reaction Bonded SiC (RBSC),” *Ceram. Int.,* **27** 559-63 (2001).
23. ASTM Standard C 1368 entitled “Standard Test Method of Determnication of Slow Crack Growth Parameters of Advanced Ceramics by Constant Stress-Rate Flexural Testing at Ambient Temperature,” ASTM International, 2006.
24. A. A. Wereszczak, H. -T. Lin, T. P. Kirkland, M. J. Andrews, and S. K. Lee “Strength and Dynamic Fatigue of Silicon Nitride at Intermediate Temperatures,” *J. Mater. Sci.* **37** 2669-2684 (2002).
25. H. T. Lin, M. K. Ferber, T. P. Kirkland, and S. M. Zemskova, “Dynamic Fatigue of CVD-Mullite Coated SN88 Silicon Nitride,” ASME GT2003-38919, published in the Proceedings of at 2003 ASME TURBO EXPO: Power for Land, Sea & Air 2002, June 16-19, Atlanta, GA.

Table I – Quantitative x-ray diffraction and porosity measurements.

Phase	XRD Wt %	XRD Vol %	Total Vol %
SiC-6H	68.2	61.8	25.8
SiC-15R	4.7	4.3	1.8
Silicon	16.0	20.0	8.3
Cristobalite	11.1	13.9	5.8
Porosity	---	---	58.3

* Geometric volume: includes solids plus all open and closed porosity of plate samples, i.e., no channels
** () values = standard deviation
[¥] He pycnometry: volume includes solids plus all closed porosity
[Ø] Relative density (ρ_{bulk}/ ρ_{skel} *100)

Table II – Young's modulus, thermal expansion coefficient, room temperature strength, fracture toughness and various measures of density of the SiC DPF material studied. Density definitions are given in ASTM D3766.[3]

Property/Material	SiC
Literature density (g/cc)	3.217 [§,4], 2.85-3.10 [§§,5], 3.11 [§§§,6], 2.98 [§§§§,6]
Bulk (g/cc)*	1.18(0.03) **
Skeletal (g/cc)[¥]	2.83(0.05)
Relative ρ (%)[Ø]	41.7
Porosity (%)	58.3
Literature polycrystalline Young's Modulus for dense material (GPa)	420 [∞,7], 320-340 [∞∞,5], 359-407 [8]
Young's Modulus (GPa)***	20(2.5)
Literature polycrystalline CTE for dense material ($x10^{-6}$ 1/°C)	4.85 [∞,9], 4.5 [10], 4.3-4.6 [11]
CTE parallel[¢] ($x10^{-6}$ 1/°C)	5.00(0.04)
CTE perpendicular[¢¢] ($x10^{-6}$ 1/°C)	5.10(0.08)
Strength (MPa) @ RT[¥¥]	19.5(0.63)
K_{IC} (MPa√m) @ RT	0.42(0.05)

* Geometric volume: includes solids plus all open and closed porosity of plate samples, i.e., no channels
** () values = standard deviation
[¥] He pycnometry: volume includes solids plus all closed porosity
[Ø] Relative density (ρ_{bulk}/ ρ_{skel} *100)
[§] 0 v% free Si; [§§] 15-35 v% free Si; [§§§] 12 v% free Si; [§§§§] 26 v% free Si in RBSC
*** Dynamic Mechanical Analysis (DMA); MOI corrected; 2-5 samples, Each remounted >5 X
Linear coefficient of thermal expansion [¢]parallel and [¢¢]perpendicular to the extrusion direction; RT -1000°C
[¥¥] MOI corrected
[∞] CVD β-SiC, no free Si, [∞∞] 15-35 v% free Si

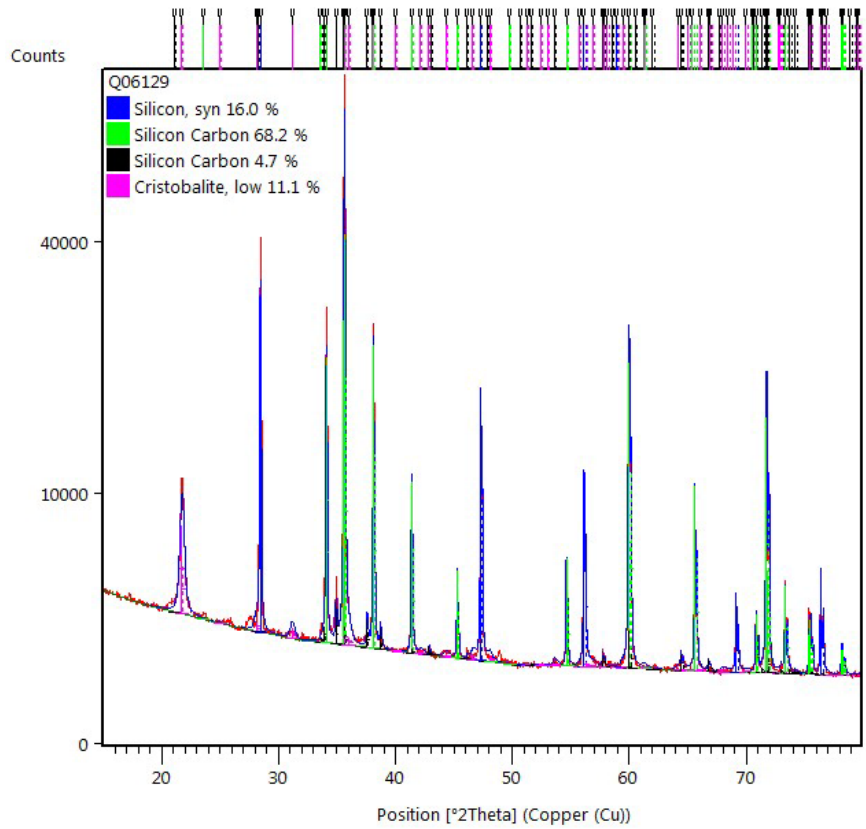

Figure 1 – The x-ray diffraction pattern the SiC-based DPF material. Quantitative x-ray diffraction revealed that there is about 16 wt % Si, 73 wt % SiC and 11 wt % Cristobalite (SiO_2) in the solid, excluding porosity.

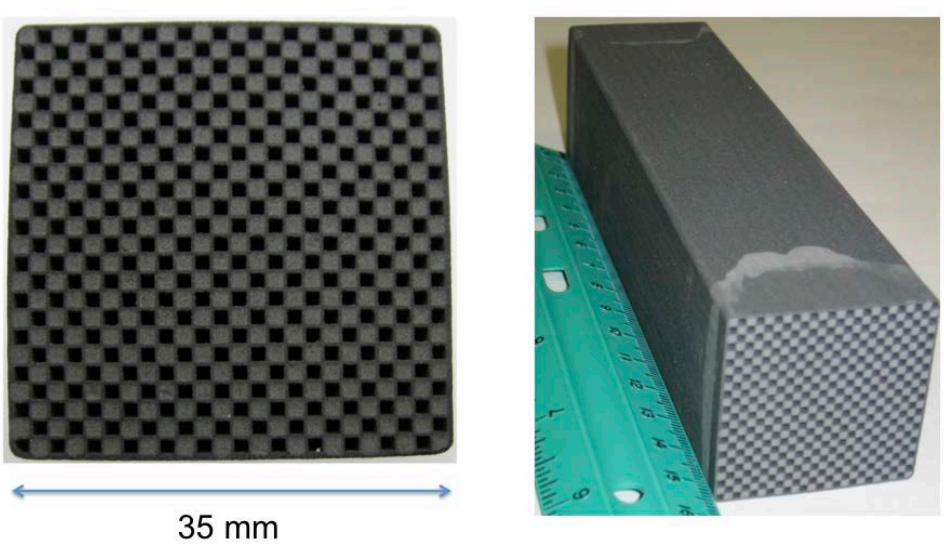

Figure 2 – The SiC-based DPF material comes in segments (35 X 35 x 153 mm) that may be joined together to form a larger DPF. The cell size is roughly 1.1 square with nominal wall thickness of 400 microns.

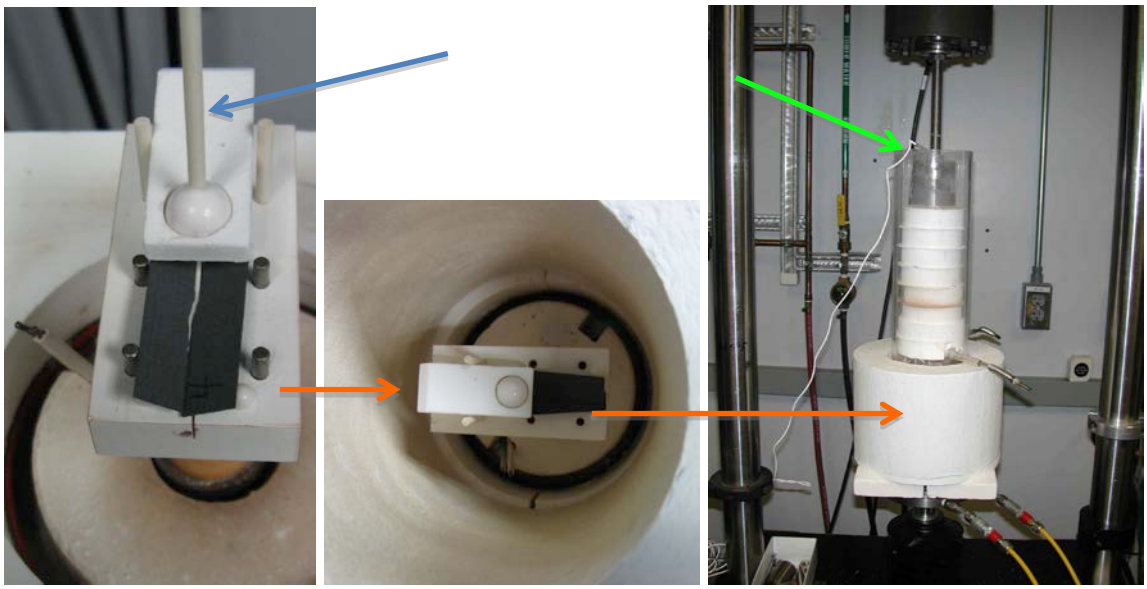

A. B. C.

Figure 3 – The high temperature double torsion experimental set-up. A.) Failed sample and jig without furnace. A thermocouple is seen to the left and blue arrow highlights the Al_2O_3 push rod. B.) A "successfully" fractured double torsion SiC-based sample within furnace. C.) The exterior view of the high temperature double torsion experimental set-up. The green arrow points to the small load cell connected to the Al_2O_3 push-rod.

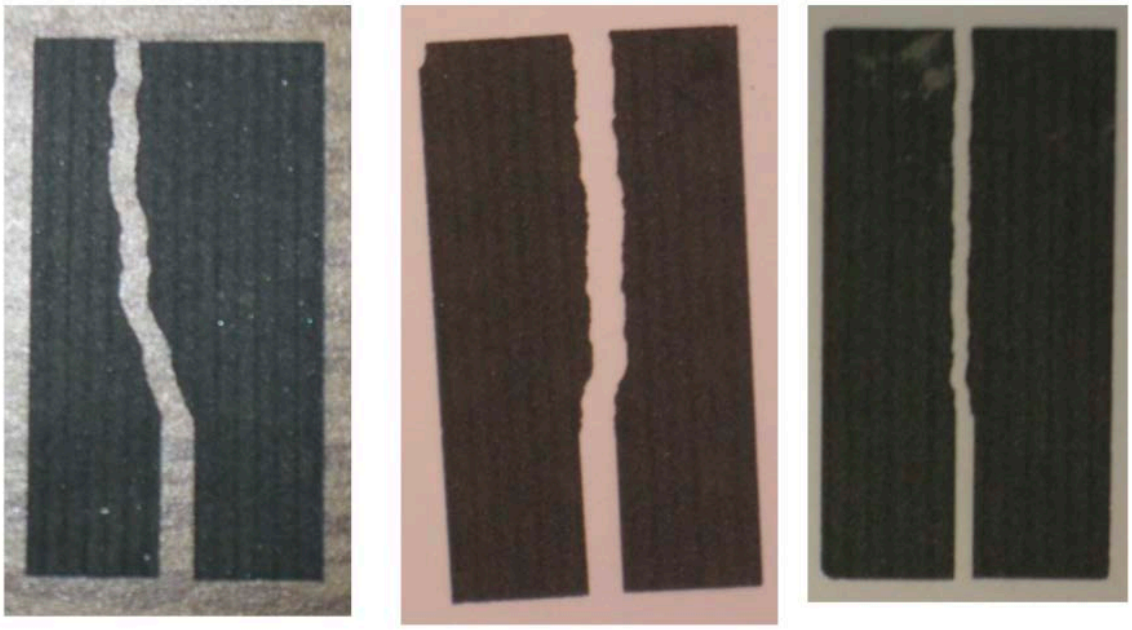

Figure 4 – Examples of successful and accepted tests. That is when the crack propagates from the precracked notch tip (bottom) to the far side (top).

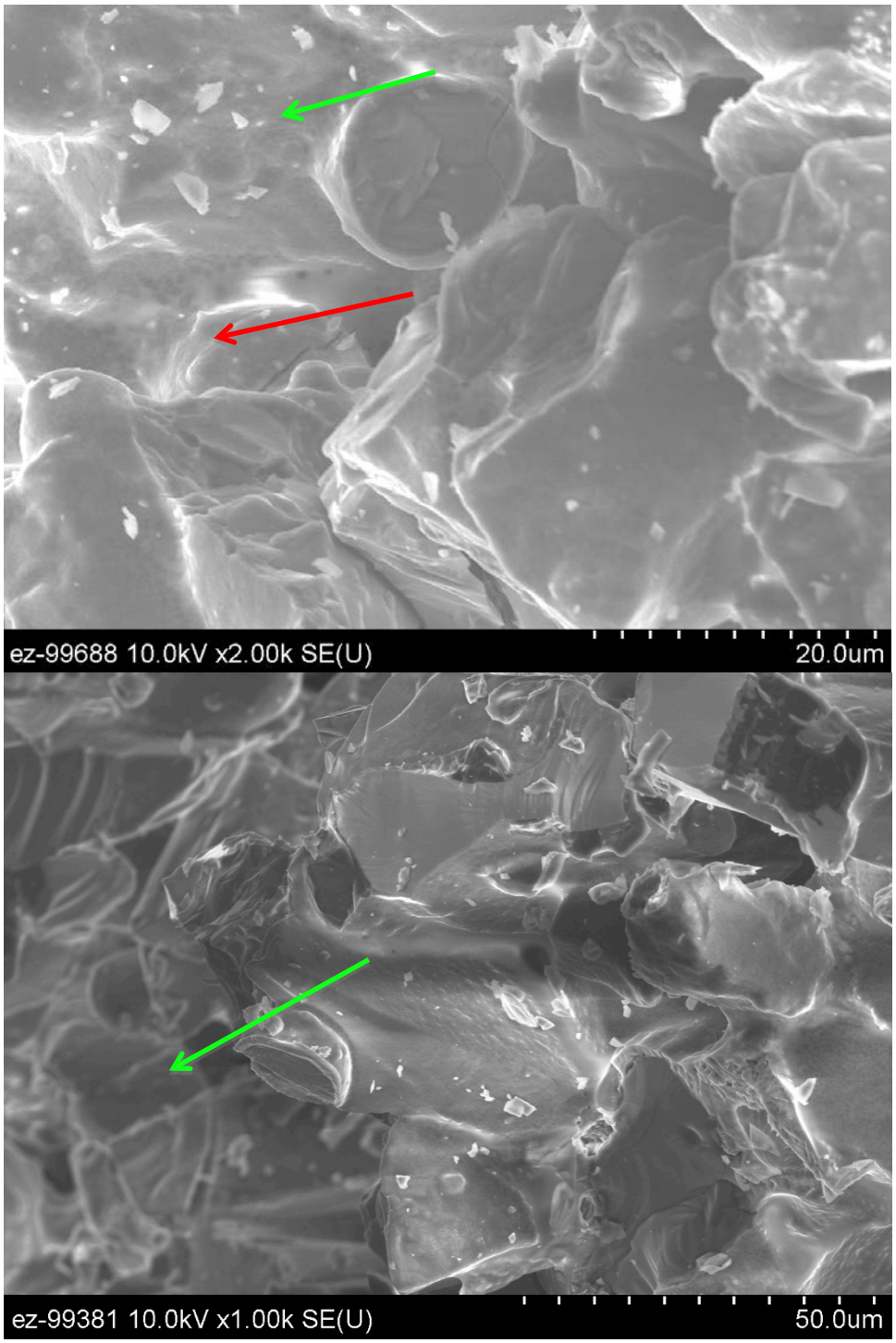

Figure 5 – SEM micrograph of a double torsion fracture surface of a SiC-based DPF material tested at room temperature. The green arrows indicate Si-rich nodules (per EDS) when the red arrow indicates a microcrack.

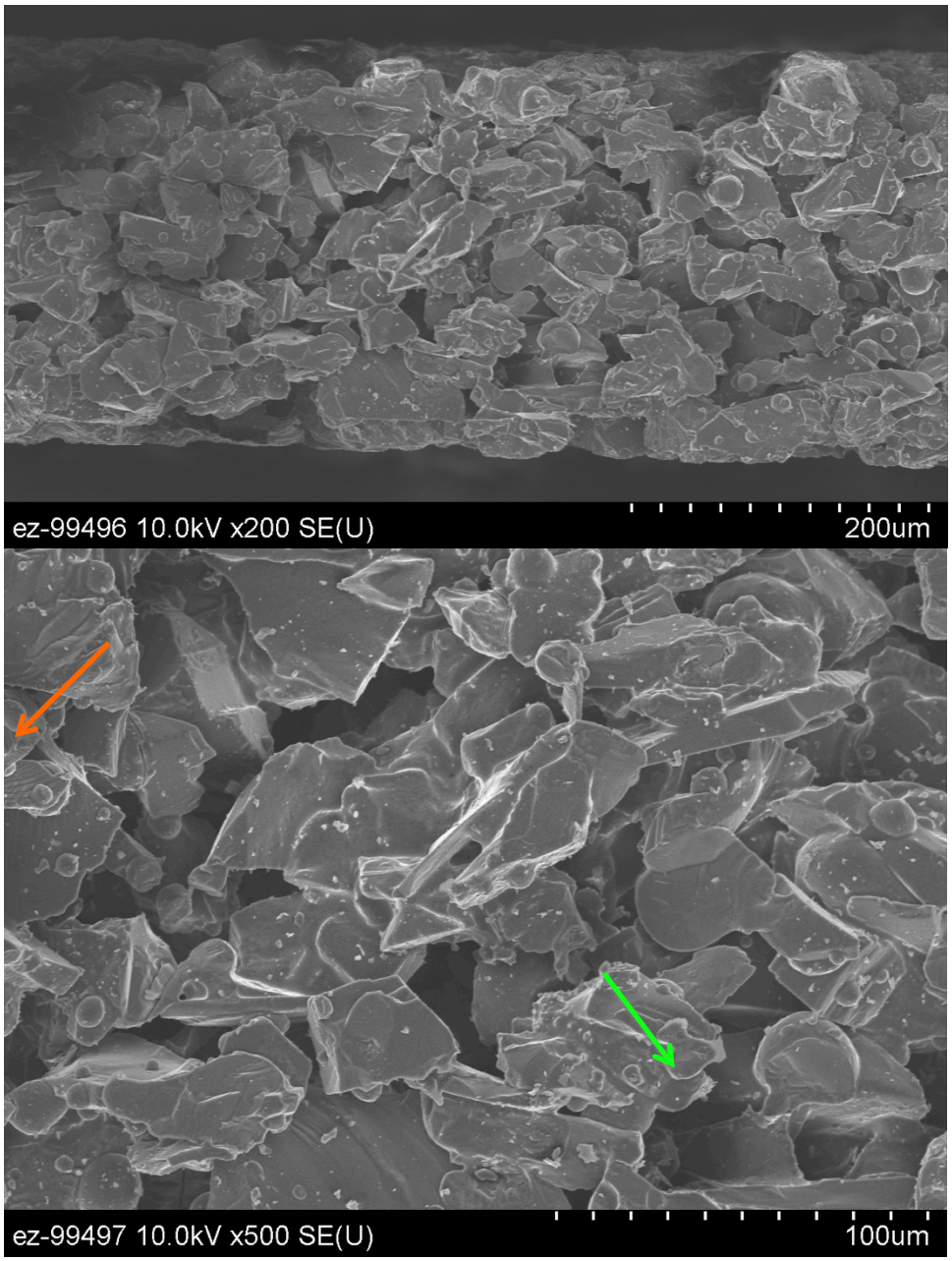

Figure 6 – SEM micrographs of the double torsion fracture surface of a SiC-based DPF material tested at 500°C. The upper micrograph covers the entire thickness. Note the numerous pores and abundant grinding debris (white particles); the grain size ranges from 10-50 μm. One microcrack is indicated by the red arrow.

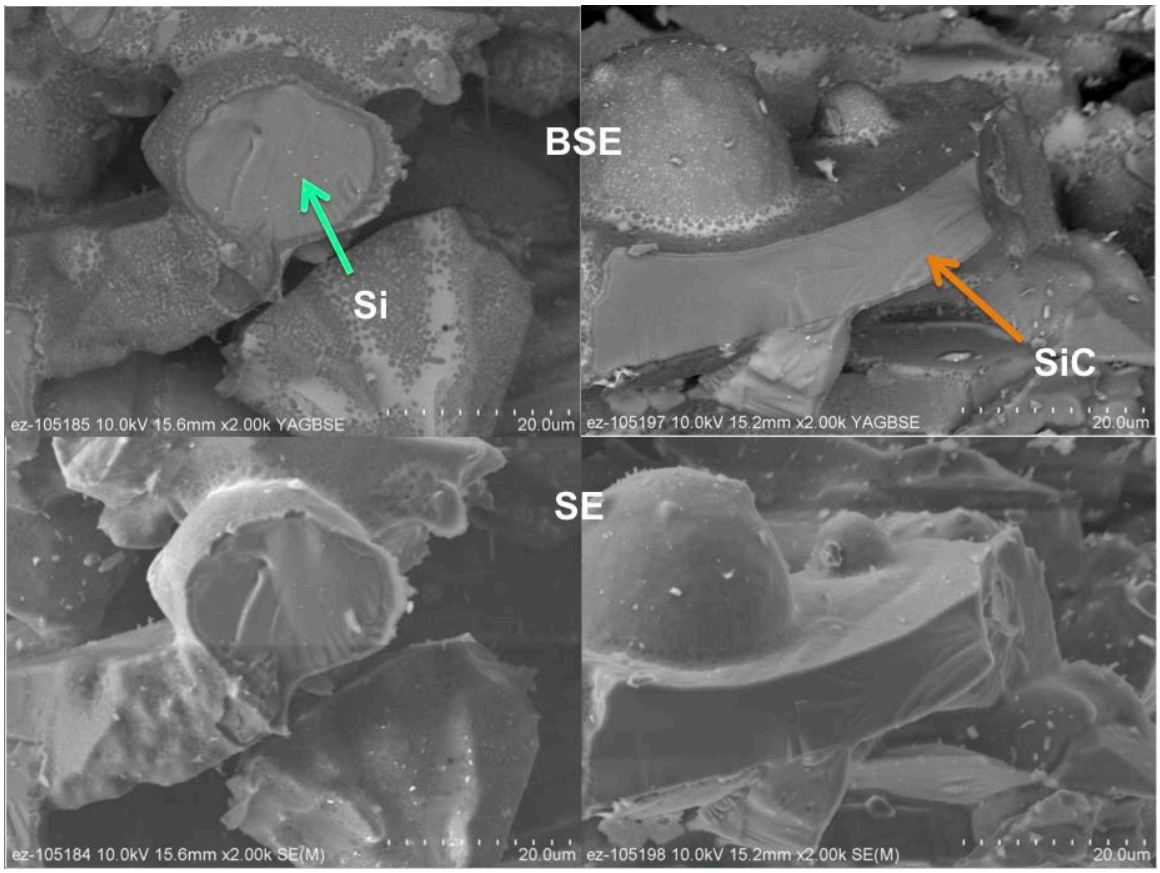

Figure 7 – The fracture surface of a SiC-based DPF double torsion specimen tested at 900°C. Again, an example Si-rich nodule is indicated by the green arrow.

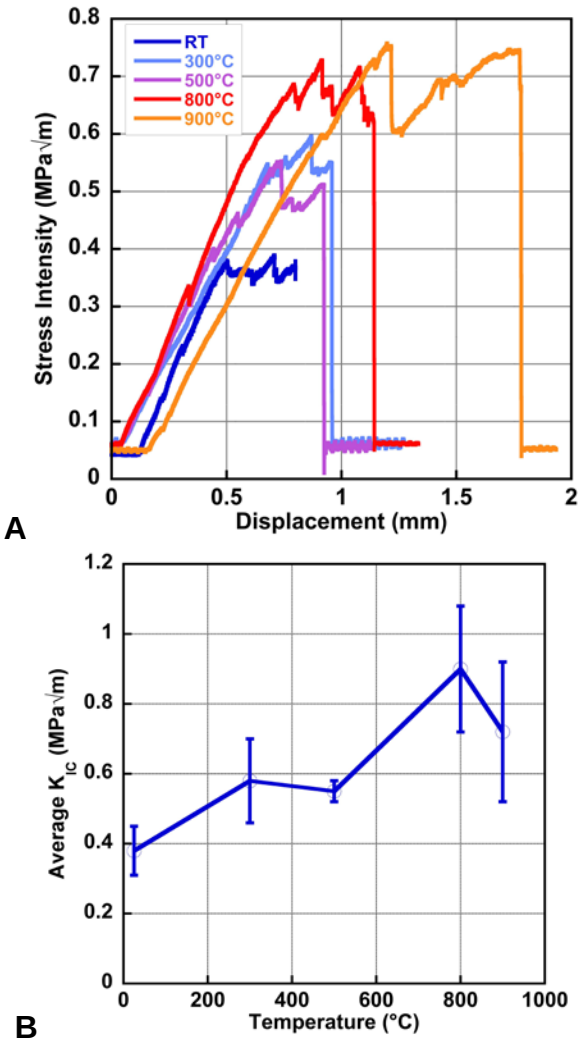

Figure 8 – A.) Typical stress intensity as a function of displacement for double torsion samples of silicon carbide based DPF materials, B.) The average fracture toughness as a function of temperature for the silicon carbide based DPF materials. The standard deviation of the K_{IC} measurements is plotted with the error bars.

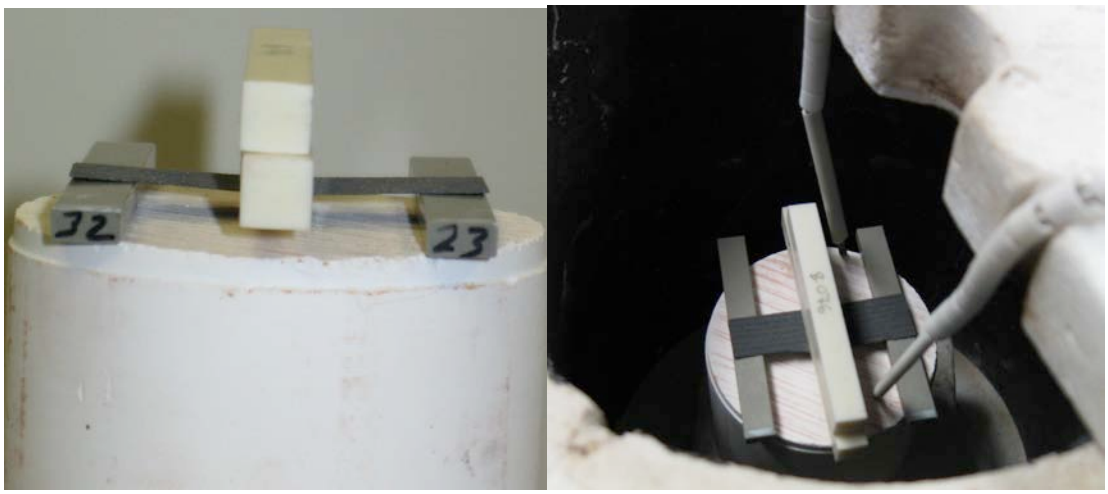

Figure 9 – One half of a double torsion sample (fractured at ambient) is dead loaded (~17 g) for 24 hours at 900°C.

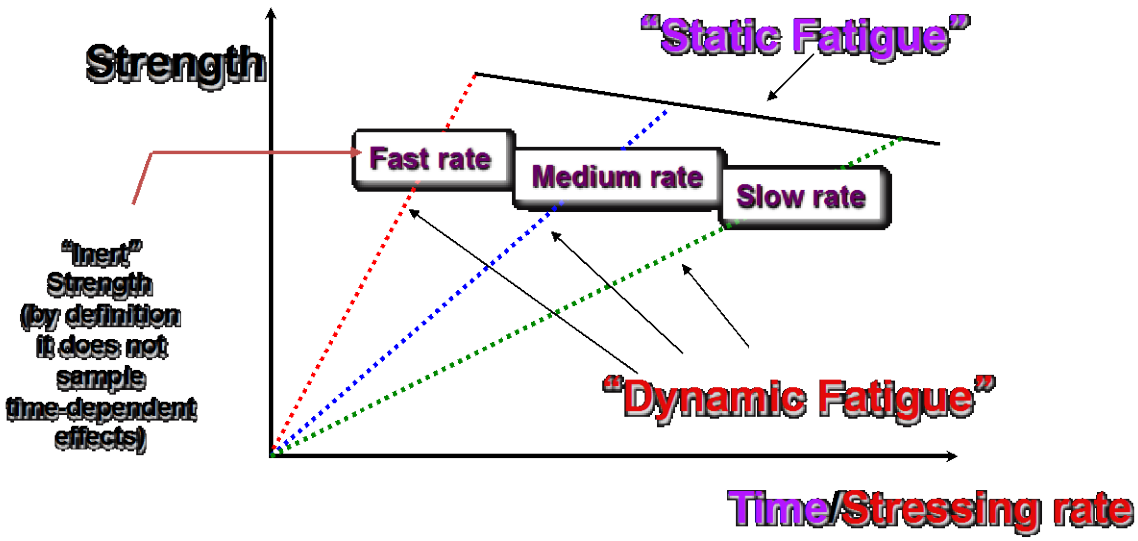

Figure 10 – A schematic comparing dynamic and static fatigue. Purple lettering refers to static fatigue and red dynamic.

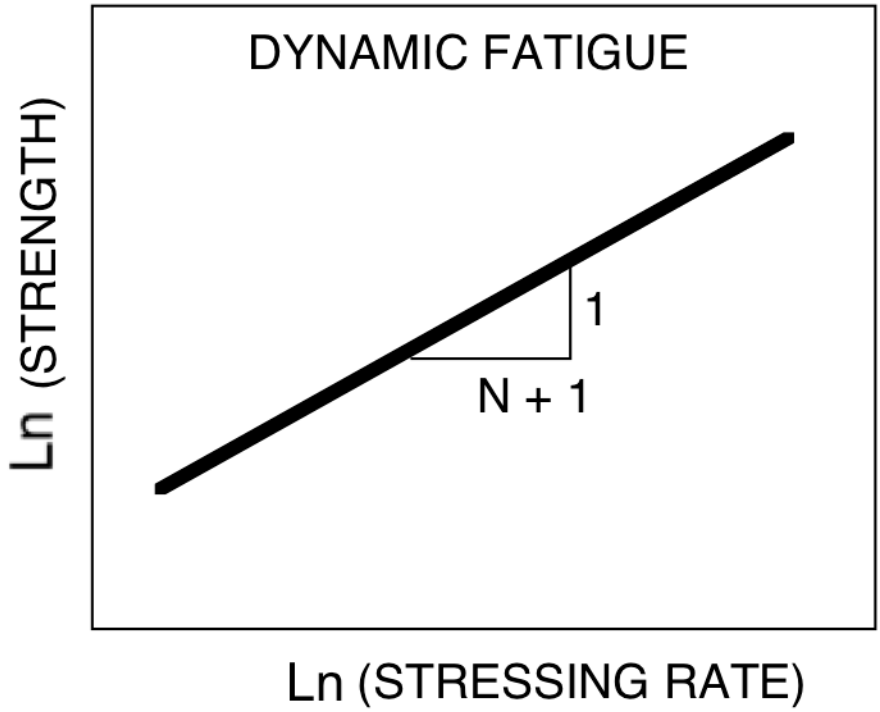

$$\ln(\sigma_f) = 1/(N+1)\ln(\dot{\sigma}) + C''$$

Figure 11 – A schematic of a dynamic fatigue curve, where σ_f, $\dot{\sigma}$, N and C" are the failure strength, stressing rate and environmentally dependent constants, respectively.

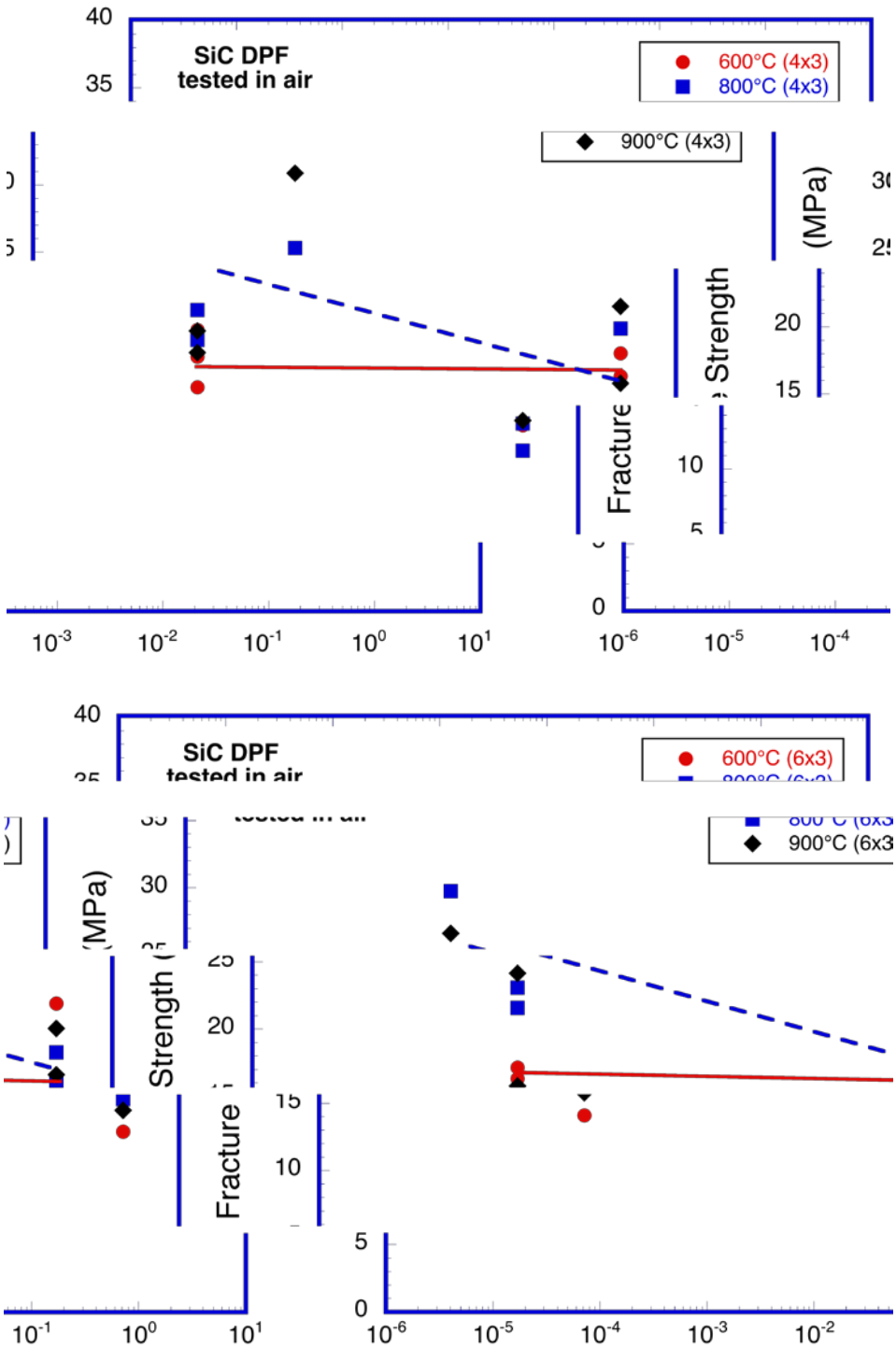

Figure 12 – The flexural strength of SiC DPF materials as a function of stressing rate (time), temperature and cross-sectional size.

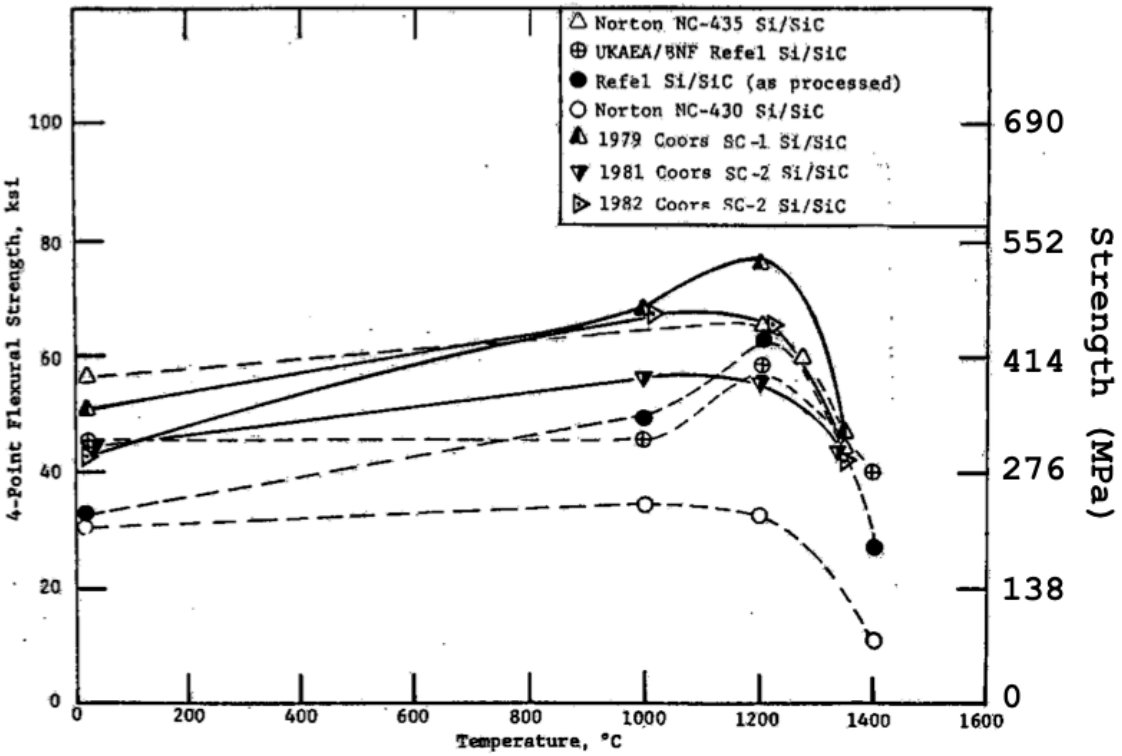

Figure 13 – Flexural strength of siliconized SiC as a function of temperature. [After Larson and Adams, AFWAL-TR-83-4141, 1983.[19]]

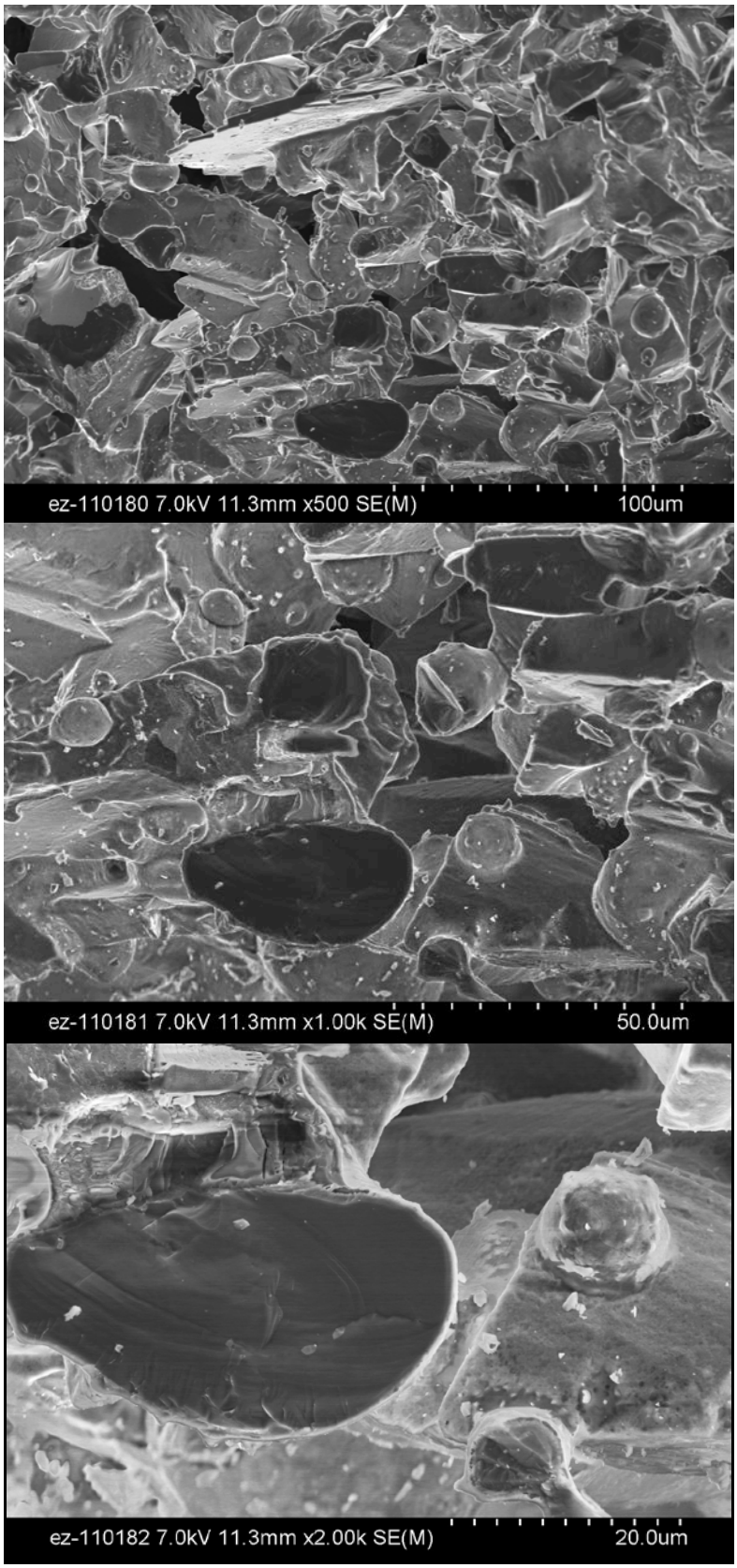

Figure 14 – Fracture surfaces of the samples tested at 600°C and 0.003MPa/s.

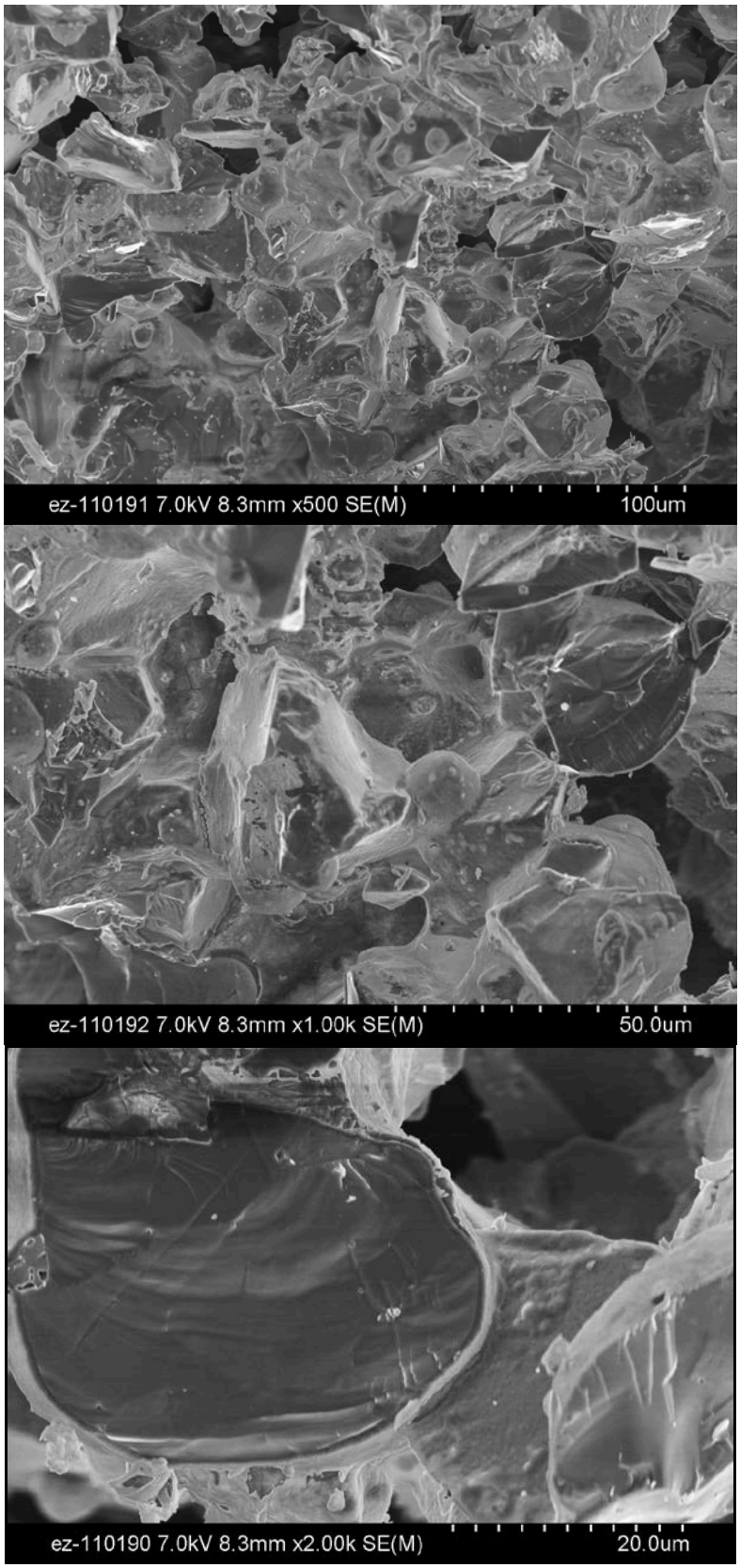

Figure 15 – Fracture surfaces of the samples tested at 900°C and 0.003MPa/s.

Agreement 10635: Catalysis by First Principles

C. Narula, M. Moses DeBusk, Xiaofan Yang
Oak Ridge National Laboratory

Objective/Scope

This research focuses on an integrated approach between computational modeling and experimental development, design and testing of new catalyst materials, that we believe will rapidly identify the key physiochemical parameters necessary for improving the catalytic efficiency of these materials. The results will have direct impact on the optimal design, performance, and durability of supported catalysts employed in emission treatment; e.g., lean NO_x catalyst, three-way catalysts, oxidation catalysts, and lean NO_x traps etc.

The typical solid catalyst consists of nano-particles on porous supports. The development of new catalytic materials is still dominated by trial and error methods, even though the experimental and theoretical bases for their characterization have improved dramatically in recent years. Although it has been successful, the empirical development of catalytic materials is time consuming and expensive and brings no guarantees of success. Part of the difficulty is that most catalytic materials are highly non-uniform and complex, and most characterization methods provide only average structural data. Now, with improved capabilities for synthesis of nearly uniform catalysts, which offer the prospects of high selectivity as well as susceptibility to incisive characterization combined with state-of-the science characterization methods, including those that allow imaging of individual catalytic sites, we have compelling opportunity to markedly accelerate the advancement of the science and technology of catalysis.

Computational approaches, on the other hand, have been limited to examining processes and phenomena using models that had been much simplified in comparison to real materials. This limitation was mainly a consequence of limitations in computer hardware and in the development of sophisticated algorithms that are computationally efficient. In particular, experimental catalysis has not benefited from the recent advances in high performance computing that enables more realistic simulations (empirical and first-principles) of large ensemble atoms including the local environment of a catalyst site in heterogeneous catalysis. These types of simulations, when combined with incisive microscopic and spectroscopic characterization of catalysts, can lead to a much deeper understanding of the reaction chemistry that is difficult to decipher from experimental work alone.

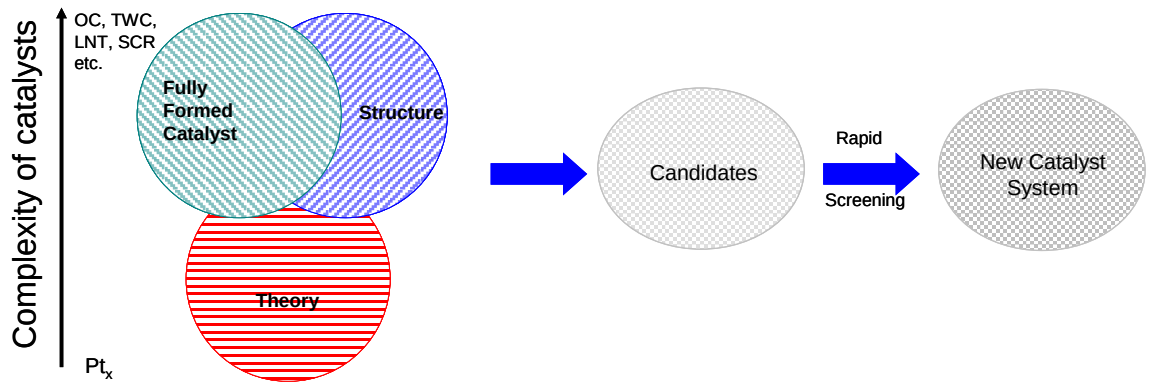

Thus, a protocol to systematically find the optimum catalyst can be developed that combines the power of theory and experiment for atomistic design of catalytically active sites and can translate the fundamental insights gained directly to a complete catalyst system that can be technically deployed.

Although it is beyond doubt computationally challenging, the study of surface, nanometer-sized, metal clusters may be accomplished by merging state-of-the-art, density-functional-based, electronic-structure techniques and molecular-dynamic techniques. These techniques provide accurate energetics, force, and electronic information. Theoretical work must be based on electronic-structure methods, as opposed to more empirical-based techniques, so as to provide realistic energetics and direct electronic information.

A computationally complex system, in principle, will be a model of a simple catalyst that can be synthesized and evaluated in the laboratory. It is important to point out that such a system for experimentalist will be an idealized simple model catalyst system that will probably model a “real-world” catalyst. Thus it is conceivable that “computationally complex but experimentally simple” systems can be examined by both theoretical models and experimental work to forecast improvements in catalyst systems.

We have focused on the oxidation catalyst and SCR catalyst to develop and demonstrate catalyst by design protocol as a prelude to developing catalyst by design protocols for complex emission treatment catalysts; e.g., TWCs, NO_x traps, and HC-SCR catalysts. Our goals are as follows:

- Our theoretical goal is to carry out the calculation and simulation of realistic supported Pt nanoparticle systems (i.e., those equivalent to experiment), in particular by addressing the issues of complex cluster geometries on local bonding effects that determine reactivity. As such, we expect in combination with experiment to identify relevant clusters, and to determine the electronic properties of these clusters. In addition, we plan to study zeolite structures with a view to develop an insight on the mechanistic aspects of catalytic process to enable us to develop better catalysts.
- Our experimental goal is to synthesize metal carbonyl clusters, decarbonylated metal clusters, sub-nanometer metal particles, and metallic particles (~5 nm) on

alumina (commercial high surface area, sol-gel processed, and mesoporous molecular sieve), characterize them employing modern techniques including Aberration Corrected Electron Microscope (ACEM), and evaluate their CO, NO_x, and HC oxidation activity. Furthermore, guided by theoretical studies we plant to synthesize new zeolites and characterize them.

- This approach will allow us to identify the catalyst sites that are responsible for CO, NO_x, and HC abatement. We will then address design of new durable catalysts systems that can withstand the prolonged operations.

Technical Highlights

Until recently, our theoretical studies have focused on supported noble metals. We have shown that single platinum atoms supported on θ-alumina slab are in the zero oxidation state. This result is very different from that reported in literature on single platinum atoms supported on α-alumina or simplified models of γ-alumina where a platinum atom generally has an unpaired electron. This also means that the mechanism of CO, NO_x, or HC oxidation on Pt(0) will be different from that on Pt(I) or Pt(II). We plan to carry out first principle studies of CO oxidation on Pt atoms supported on θ-alumina slab.

Since our experimental work has already shown that the distribution of platinum on γ-alumina and θ-alumina is almost identical, and the surface properties and CO oxidation of both catalysts are identical, we propose that Pt supported on θ-alumina is a better model for Pt supported on γ-alumina than Pt supported on α-alumina or simplified models of γ-alumina.

We have also shown that incorporation of palladium in platinum particles at sub-nanometer scale is quite ineffective in improving the durability, however, large Pt-Pd nanoparticles tend to be more hydrothermally durable than pure Pt particles. While efforts are in progress to prepare sub-nanometer Pt-Pd particles to validate the results of theoretical studies, we have initiated theoretical studies of SCR-zeolite-catalysts.

In the previous quarter report, we also presented our results on the theoretical and experimental studies of CO oxidation on single atoms. We provide additional data in this report and summarize our results on agglomeration of Pt atoms supported on alumina..

CO Oxidation on Pt/θ-alumina (010) surface

Previously, we described the proposed pathway to CO oxidation on single Pt atoms supported on θ-alumina. The theoretical models show that the pathway is very similar to the one on $(Ph3P)_2Pt$, an organometallic complex, and bridges homogenous and heterogeneous catalysis. The energy barrier calculations are in progress and will be reported in the next quarter. We also synthesized the samples with 0.18% and 1.0% Pt loading and carried out EXAFS and XANES analysis. Commensurate with EXFAS results, the electron microscopic images, obtained on ACEM, show single atom distribution on 0.18% sample and 10-20 atom agglomerates in 1.0% sample [Figure 1]. The EXFAS data also suggest that 10-20 agglomerates are prone to sintering even under relatively mild reducing conditions.

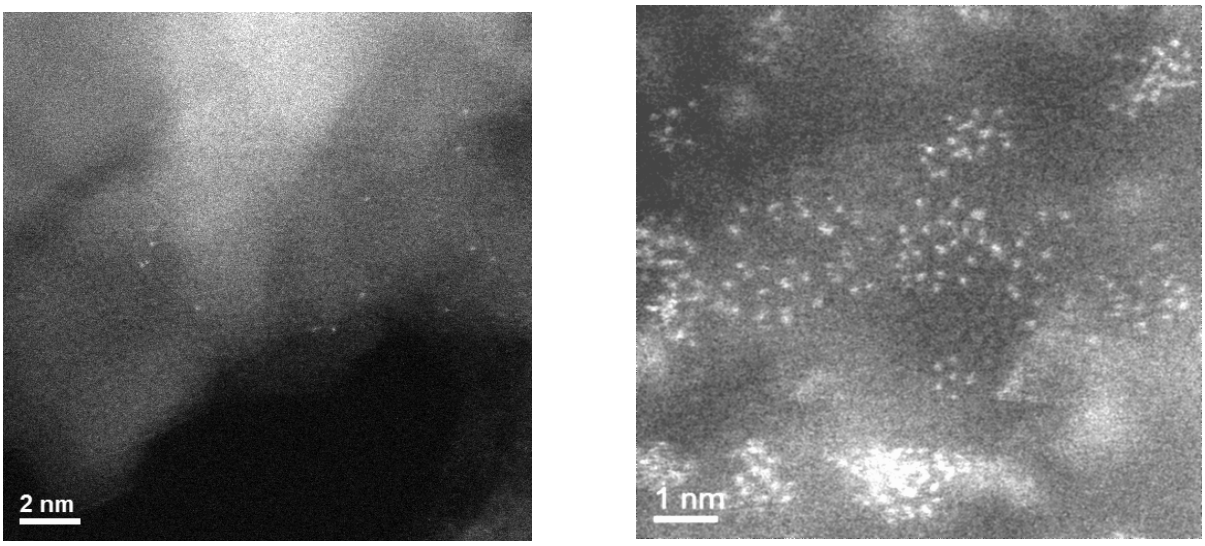

Figure 1: ACEM images of 0.18% Pt/θ-Al_2O_3 (left) and 1.0% Pt/θ-Al_2O_3 (right)

The CO absorption studies were carried out on a DRIFTS instrument [Figure 2]. First, the samples were heated under a flow of helium to remove surface impurities and then were exposed to a flow of CO at room temperature and at 170ºC. The 0.18% Pt/θ-Al_2O_3 exhibits a broad absorption for CO at room temperature while 1.0% Pt/θ-Al_2O_3 shows features for CO adsorbed in terminal and bridging mode (1850 cm^{-1}). The presence of bridging CO adsorption mode suggests the presence of Pt-Pt bonds in this sample.

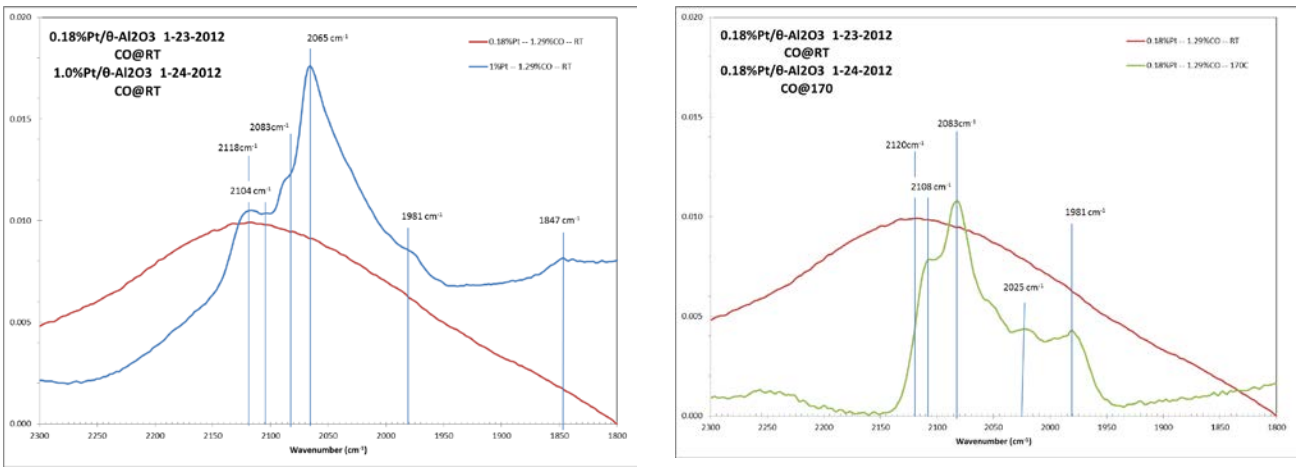

Figure 2: IR of CO adsorption on 0.18% Pt/θ-Al_2O_3 and 1.0% Pt/θ-Al_2O_3 at RT (left) and on 0.18% Pt/θ-Al_2O_3 at RT and 170°C (right)

The 0.18% Pt/θ-Al_2O_3 sample does show features for terminal adsorption of CO at 175ºC but no features for CO in bridging mode. The absence of CO adsorption in bridging mode is indicative of absence of Pt-Pt bonds in conjunction with the results of EXAFS and ACEM data only.

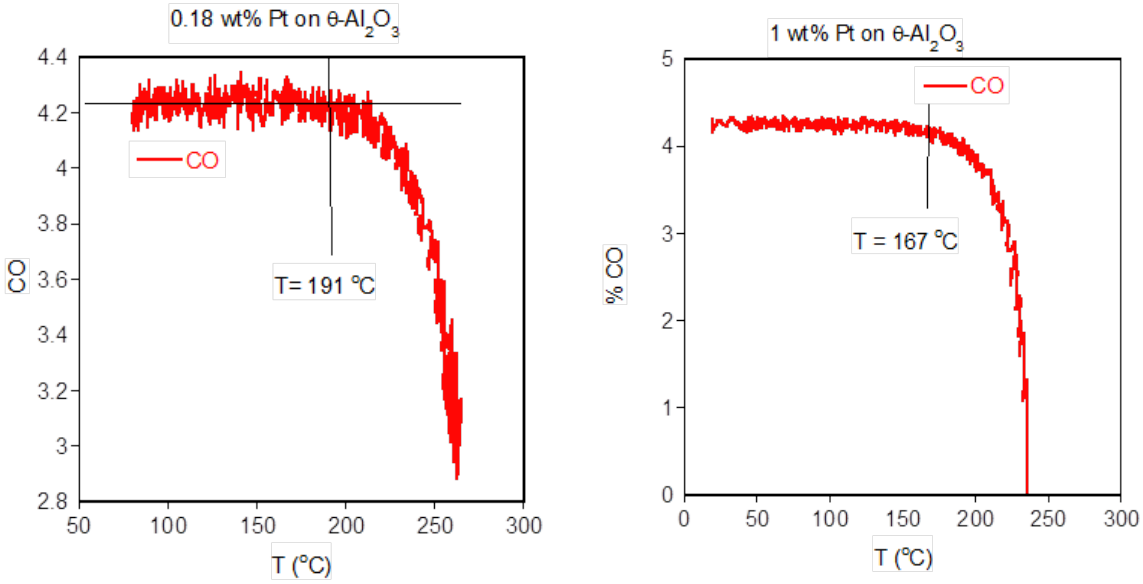

Figure 3: CO oxidation on 0.18% Pt/θ-Al_2O_3 (left) and 1.0% Pt/θ-Al_2O_3 (right)

The light-off of CO oxidation on 0.18% Pt/θ-Al_2O_3 is at 191ºC and that on 1.0% Pt/θ-Al_2O_3 is at 167ºC [Figure 3]. This experiment clearly shows that single Pt atoms are catalytically active.

As indicated above, the calculations of energy barriers between various intermediates in proposed CO oxidation mechanism are in progress. We are writing a manuscript to describe these results. Since this will be the first example of CO oxidation on single atoms without support involvement, we expect the acceptance of manuscript in a high impact journal.

Sintering of Pt atoms on Pt/θ-alumina (010) surface

The sintering of platinum particles has been extensively studies and some of the models developed for Pt particles also apply to Pt nanoparticles. Theoretical studies point to structures of various small clusters and show that oxidized Pt is more prone to sintering. However, the reasons for facile sintering of Pt particle are not well understood. It is in this context we started our work to understand the reason for sintering with the expectation that insights will help us design the catalyst materials that are less susceptible to sintering. We have completed the study of 2 and 3-atom systems. We find that there is no significant difference between binding energy of two atom clusters and two independent atoms. For three-atom clusters, the clusters are more energetically favored over three independent atoms. **These results show that**

increased stability of clusters over supported independent atoms provides the driving force for sintering. The results are summarized below:

Two-atom clusters: The total energy of two independent atoms on 010 surface of θ-Al_2O_3 is -3047.5495 eV. There are two possible locations of two atom Pt clusters are shown in Figure 4 (middle and right).

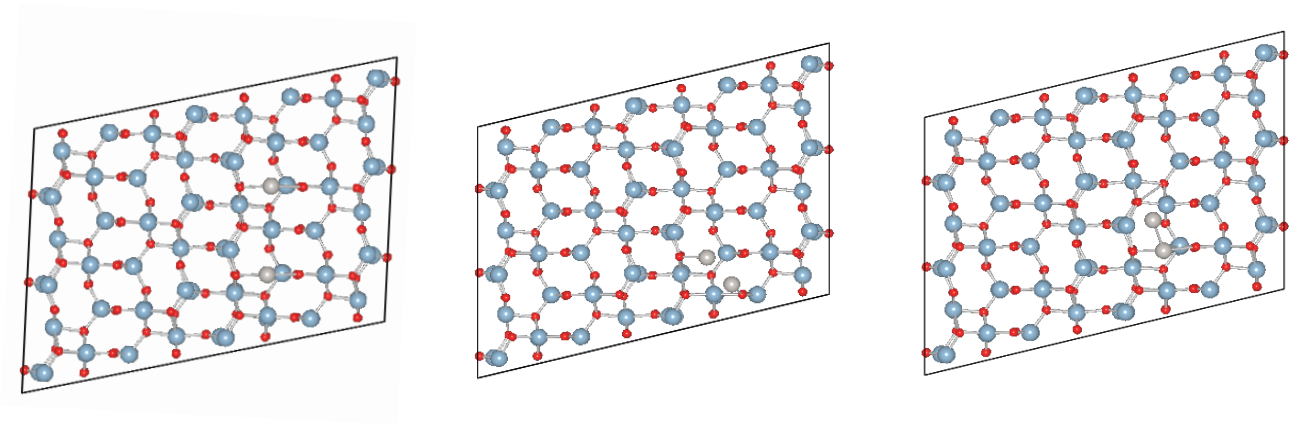

Figure 4: Two Pt atoms (left) and two atom clusters (middle & right) on 010 surface of θ-Al_2O_3

The energy of the two atom clusters shown in Figure 4 is -3047.8793 and -3047.7091 eV, respectively. This suggests that 2 atom clusters are energetically favored by 7.6 and 3.86 Kcal/mole. Although difference in energy of independent atoms and 2-atom clusters is low, the results do point to the fact that there is no significant barrier to sintering of Pt when distributed atomically on alumina surface.

Three atom clusters: The total energy of three independent atoms on 010 surface of θ-Al_2O_3 is -3051.1554 eV. There are two possible locations of three atom Pt clusters are shown in Figure 5 (middle and right).

The energy of the three atom clusters shown in Figure 5 is -3052.2214 and -3053.0851 eV, respectively. This suggests that 3 atom clusters are energetically favored by 24.59 and 44.51 Kcal/mole. The significant differences in energy of independent atoms and 3-atom clusters clearly show that the driving force for sintering is the energetics of clusters which is apparent even for a 3-atom system.

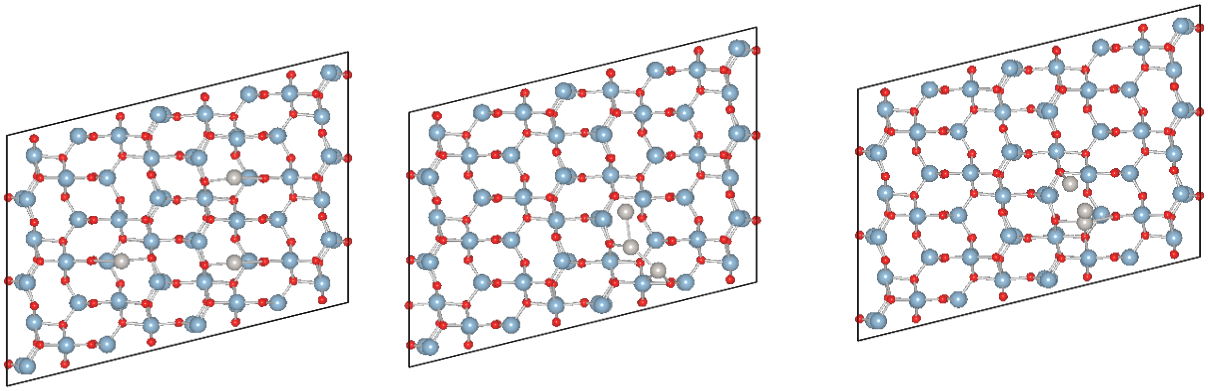

Figure 5: Three Pt atoms (left) and three atom clusters (middle & right) on 010 surface of θ-Al_2O_3

The detailed analysis of these structures will be presented in the next report.

Status of FY2012 Milestones:

1. We will complete theoretical modeling of large supported Pt clusters by Sept 2012 resulting in a thorough understanding of subnanometer Pt and Pt clusters supported on alumina.

   We have completed modeling of 2 and 3 atom clusters and larger cluster analysis is in progress.

2. This information will be used to initiate mechanistic studies of CO oxidation are nearing completions. The NO_x and HC oxidation on Pt/alumina and heterobimetallic zeolites will be initiated in the next quarter.

Communication/Visits/Travel

We have published a manuscript titled "Ab Initio Density Functional Calculations of Adsorption of Transition Metal Atoms on θ-Al_2O_3(010) Surface" Journal of Physical Chemistry, C

Problems Encountered

None

Publications

1. C.K. Narula, M.G. Stocks, "Ab Initio Density Functional Calculations of Adsorption of Transition Metal Atoms on θ-Al_2O_3(010) Surface" J. Phys. Chem,. C, 2012, 116, 5628.

2. C.K. Narula, “Catalyst by Design – Bridging the Gap between Theory and Experiments at Nanoscale Level” Encyclopedia of Nanoscience and Nanotechnology, Vol. II, Taylor & Francis, New York, 2008, pp 771-782 (invited).
3. C.K. Narula, L.F. Allard, D.A. Blom, M. Moses-DeBusk, “Bridging the Gap between Theory and Experiments – Nano-structural Changes in Supported Catalysts under Operating Conditions” SAE-2008-01-0416, SAE Int. J. Mater. Manu., 1(2008) 182-188.
4. C.K. Narula, L.F. Allard, D.A. Blom, M.J. Moses, W. Shelton, W. Schneider, Y. Xu, "Catalysis by Design - Theoretical and Experimental Studies of Model Catalysts", SAE-2007-01-1018 (invited).
5. C.K. Narula, M.J. Moses, L.F. Allard, “Analysis of Microstructural Changes in Lean NO_x Trap Material Isolates Parameters Responsible for Activity Deterioration” SAE 2006-01-3420.
6. Y. Xu, W.A. Shelton, and W.F. Schneider, “The thermodynamic equilibrium compositions, structures, and reaction energies of Pt*x*O*y* (*x* = 1-3) clusters predicted from first principles,” *Journal of Physical Chemistry B,* 110 (2006) 16591.
7. Y. Xu, W. A. Shelton, and W. F. Schneider, “Effect of particle size on the oxidizability of platinum clusters,” *Journal of Physical Chemistry A*, 110 (2006) 5839.
8. C.K. Narula, S. Daw, J. Hoard, T. Hammer, “Materials Issues Related to Catalysts for Treatment of Diesel Exhaust,” *Int. J. Amer. Ceram. Tech*., 2 (2005) 452 (invited).

<u>Presentations (last 12 months)</u>

1. Narula, C.K. Stocks, G.M., Density Functional Studies of Adsorption of Transition Metal Atoms on θ-Al_2O_3(010) Surface” American Chemical Society Meeting, Denver, CO, August 28, 2011.
2. Narula, C.K.; Stocks, M. G.; First-principles studies of the structure and bonding of metal atoms supported on θ-alumina, American Chemical Society Meeting, San Francisco, March 2010.
3. Narula, C.K.; Chen, X.; Stocks, G.M., DeBusk, M.M.; Allard, L.F.; “First-Principles and Experimental Studies of the Sub-Nanomenter Platinum Atoms Supported on θ-Alumina” 230th American Chemical Society Meeting, Boston, MA, August 22-26, 2010

References

1. Cheng, P.T.; Cook, C.D., Nyburg, S.C., Wan, K.; Can. J. Chem., 49 (1971) 3772.
2. Scholz, S.; Lerner, H.W.; Bolte, M. Acta Cryst E62 (2006) m312-m313. Gregg, M.R.; Powell, J.; Sawyer, J.F.; Acta. Crystal. C44 (1988) 43-46
3. Qiao, B; Wagn, A.; Yang, X.; Allard, L.F.; Jiang, Z.; Cui, Y.; Liu, J.; Li, J.; Zhang, T.; Nature Chem., 3 (2011) 634

Agreement 19214: Effects of Biodiesel Fuel on Diesel Particulate Filter Materials

M. J. Lance, B. J. Bunting, A. A. Wereszczak, M. K. Ferber, E. E. Fox, and T. J. Toops
Oak Ridge National Laboratory

Objective/Scope

To characterize changes in the microstructure and material properties of diesel particulate filters (DPFs) in exhaust gas produced by biodiesel blends.

Technical Highlights

Finite element analyses were conducted with the completed biaxial flexure test data to estimate average tensile failure stresses and their results are summarized in Table I.

Table I. Summary of the estimated elastic modulus and average maximum tensile failure stress for biaxial flexure specimens harvested from the center of four different types of DPF ceramics. Nominal disk thickness is 1.5 mm. Ring diameters are 6.75 and 16 mm. Values in parenthesis are one standard deviation.

Material	Secant Elastic Modulus (GPa)	Average Maximum Tensile Failure Stress (MPa)
Cordierite C611-HG 59% Porosity	5.3	3.6 (± 0.5)
Cordierite C611 59% Porosity	2.7	2.9 (± 0.4)
SiC MSC-111 53% Porosity	11	11.6 (± 1.7)
SiC MSC-14 58% Porosity	11	10.4 (± 1.7)

Efforts are underway to develop a tensile test method for DPFs as well as a suitable specimen geometry. There are several advantages to tensile testing over other (bend or compression) test methods. Coupled with the measurement of tensile elongation, the

sought-after tensile testing will enable the measurement of a continuous tensile stress - tensile strain curve. Such definitive data will allow for the interpretation of non-linear tensile response, and provide critical information on the (continuous or tangent) elastic modulus as a function of tensile strain. The first sets of data shall be reported on in Q3.

Using the gen-set that was installed and tested in Q1, a standard test was devised to simulate regeneration of a DPF in s short amount of time and is shown in Fig. 1. Thermal cycling of the DPF is done by a combination of gen-set load and exhaust fuel injection and can reach temperatures up to 1200ºC in a 15 minute cycle. The maximum temperature gradient measured in the DPF approaches ~100°C at the outlet of the DPF between the center and the circumference. This test was performed with ultra-low sulfur diesel but future tests will be performed using B20 dosed with Na and/or K in order to simulate long-term operation under biodiesel conditions.

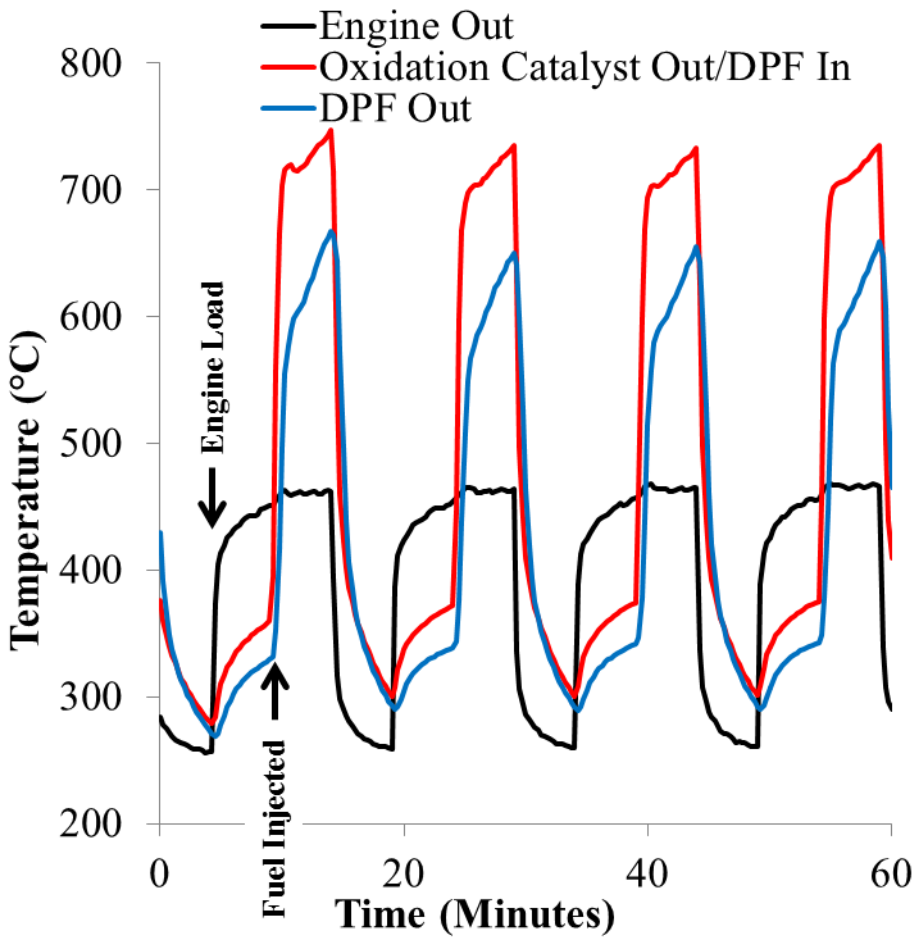

Figure 1. First DPF tested for 106 cycles using gen-set and ULSD fuel.

SiC DPF samples were also acquired from the National Renewable Energy Lab (NREL) which is a member of an industry-led team investigating the effects of biodiesel operation on emission control technologies. NREL is aging full production exhaust systems from a 2011 Ford F250 pickup using four separate fuels: ULSD, B20 + 14ppm

Na, B20 + 14ppm K and B20 + 14ppm Ca in order to simulate 150,000 miles of operation using a 100-hr test. The test protocol consisted of a three-mode, one-hour test cycle that was developed for catalyst aging: 15 minutes @ 200°C, 15 minutes @ 340°C, and 30 minutes @ 700°C. Cores were extracted from each DPF and mounted in epoxy in order to analyze the location and composition of the ash produced in this run. Preliminary images (see Fig. 2) did not reveal penetration of the ash into the SiC substrate; however, extraneous material from upstream found its way into the DPF including alumino-silicate fibers from the intumescent padding and ZrO_2 particles from the diesel oxidation catalyst. Electron microprobe and mechanical properties measurements are being conducted on these samples in order to determine if any degradation has occurred that would reduce the lifetime of SiC filters under biodiesel operation.

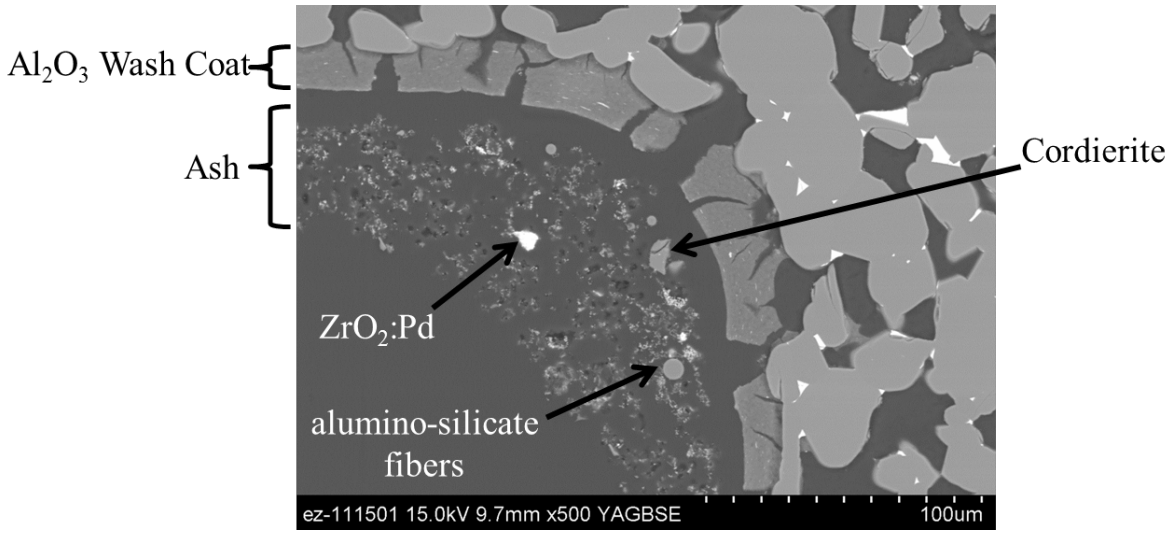

Figure 2. Cross-section of B20 + Na additive sample after simulated 150,000 miles (1 cm from outlet)

<u>Status of FY2012 Milestones</u>

1. Establish baseline mechanical testing of DPFs by measuring the elastic modulus and fracture strength of both the skin and interior of the DPF of both SiC (with 52 and 58% porosity) and cordierite (13 and 18 µm pore size) materials with at least 12 samples so as to determine fracture (Weibull) statistics. **(12/11)** *Completed.*
2. Age filter samples with Na and K doping in order to simulate long-term biodiesel exposure as dictated by the ASTM D6951 to 5 ppm and measure degradation using testing procedure developed in Milestone 1. **(9/12)** *On Schedule*

<u>Communications/Visits/Travel</u>

Lance, Wereszczak, and Fox attended the 36th International Conference on Advanced Ceramics and Composites, Daytona Beach, FL, January 23-26, 2012.

<u>Problems Encountered</u>

None

Publications/Presentations/Awards:

A. A. Wereszczak gave a presentation to the C28 Advanced Ceramics Committee on the DPF mechanical test coupons developed in this project, Daytona Beach, FL, January 22, 2012.

E. E. Fox, A. A. Wereszczak, M. J. Lance, and M. K. Ferber, “Failure Stress and Stiffness Analysis of Ceramic From a 25-mm Diameter Diesel Particulate Filter,” presented at the 36th International Conference and Exposition on Advanced Ceramics and Composites, Daytona Beach, FL, January 23-26, 2012, and accepted for publication as a proceedings paper.

References

None

Agreement 20091: Electrically Assisted DPF Material

M. J. Lance, J. E. Parks, A. A. Wereszczak, R. M. Connatser, V. Prikhodko, W. P. Partridge, E. E. Fox, and M. K. Ferber
Oak Ridge National Laboratory

Objective/Scope

In this CRADA project with General Motors (GM), two research objectives are being pursued:

1. Measure of substrate temperatures during DPF regeneration with optically based techniques that are not susceptible to conductive interferences that are problematic for common thermocouple technologies.
2. Analysis of diesel particulate filter (DPF) substrate materials to understand crack and failure mechanisms and resolve current differences in simulation and experimental results.

Technical Highlights

Experimental studies aimed at measuring the substrate temperature of the DPF during regeneration began in Q2 and are expected to continue into Q3. The experiments were conducted on the 1.9-liter diesel engine platform at ORNL on a 5.66” diameter by 6” long DPF cordierite substrate. The substrate temperatures were measured using fiber optics inserted into the exit channels of the DPF. An angled tip polished into the fiber end allowed collection of the blackbody radiation emitted from the substrate during DPF regeneration, and the corresponding light emitted in the 600 to 800 nm wavelength region was analyzed to determine the substrate temperature. A picture showing the fiber optics inserted into the DPF is shown in **Figure 1**.

Substrate temperatures were recorded during the DPF regeneration in conjunction with gas temperatures measured by standard thermocouples in similar positions throughout the DPF. Analysis of the data is in progress, but preliminary data shown in **Figure 2** demonstrates the measured substrate temperatures for a highly loaded DPF where large exotherms occur from particulate matter oxidation during the regeneration process. The data shows that the particulate on the DPF or “soot cake” oxidizes from the most upstream point to the downstream side of the DPF. The highest peak substrate temperatures observed occurred toward the latter half of the DPF at the 5” depth position.

Analysis of the data is continuing. Experiments were conducted with different particulate loading levels to better understand the exotherms produced by the particulate. During analysis, the substrate wall temperature data will be compared to the gas temperatures measured with the thermocouples to better understand the flow of heat in the DPF during the regeneration process.

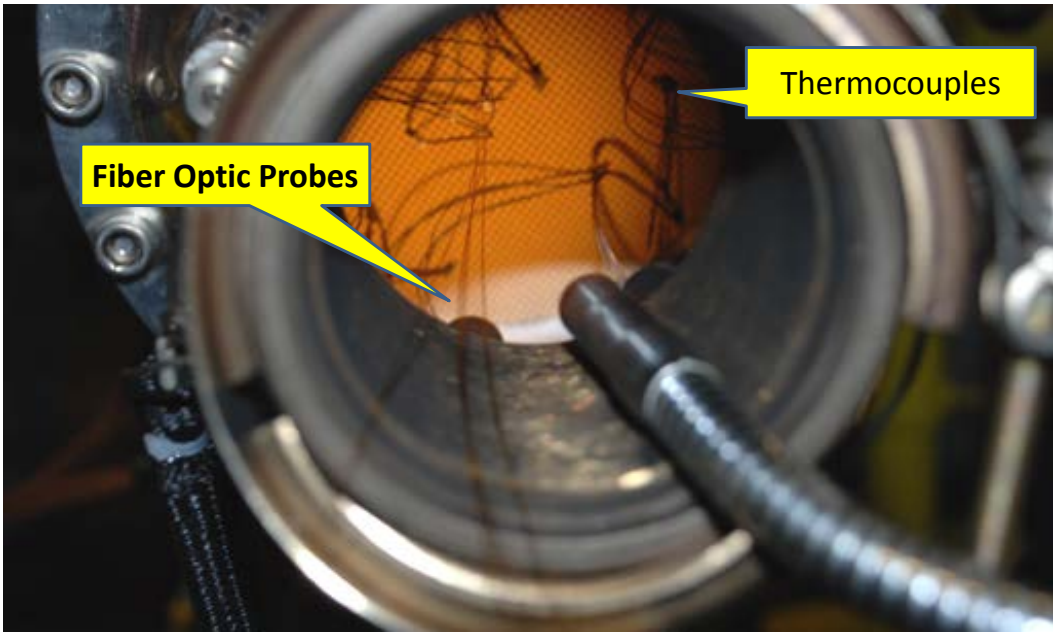

Figure 1. Picture of fiber optics inserted into downstream side of DPF exit flow channels.

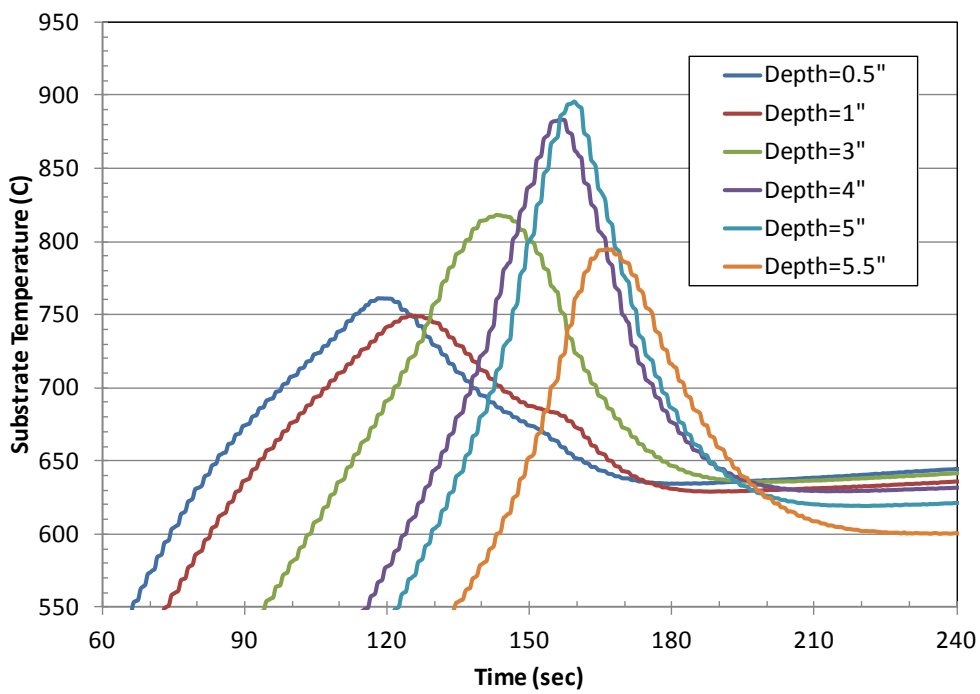

Figure 2. Substrate temperature as a function of time during a DPF regeneration as measured with the blackbody radiation fiber optic probe technique; data is shown for positions along the flow axis at different depths into the DPF.

In addition to the temperature studies on the engine platform, thermomechanical modeling efforts are underway to combine arbitrary estimates of the service conditions of a regenerating DPF with cordierite's measured mechanical properties to predict reliability and establish general rules of design.

Status of FY 2012 Milestones

(1) Measurement of the wall temperature of the DPF at 8 different locations with a spatial resolution of 1 mm and temperature accuracy of +/- 10°C during regeneration at typical operating conditions (600-800°C) using a fiber optic technique. (09/2012) *On Schedule*

(2) Creation of DPF samples with a temperature exposure history equivalent to 15000 miles of operation on a light-duty vehicle for analysis by the MST team. (09/2012) *On Schedule*

(3) Measure retained strength of laboratory-exposed DPF specimens (provided by FEERC Team from Milestone 2) and extrapolate to the degradation expected from a lifetime of electrically-assisted regenerations (~700 cycles) in order to determine if the improvement in engine efficiency from this technology is worth the potential decrease in substrate lifetime. (09/2012) *On Schedule*

Communications/Visits/Travel

A conference call was held with General Motors's Gene Gonze on February 9, 2012. DPF properties were reviewed, along with engine work, and other miscellaneous topics discussed.

Problems Encountered

None.

Publications/Presentations/Awards

A. A. Wereszczak gave a presentation to the C28 Advanced Ceramics Committee on the DPF mechanical test coupons developed in this project, Daytona Beach, FL, January 22, 2012.

A. A. Wereszczak, E. E. Fox, M. J. Lance, and M. K. Ferber, “Failure Stress and Apparent Elastic Modulus of Diesel Particulate Filter Ceramics,” manuscript to be published and presented at the SAE 2012 World Congress, Detroit, MI, April 24-26, 2012.

References

None.

Agreement 9105: Characterization of Catalyst Microstructures

L. F. Allard, C K. Narula, W. C. Bigelow, M. B. Katz, X. Pan, G. W. Graham, D. P. Nackashi and J. Damiano
Oak Ridge National Laboratory

Objective/Scope

The objective of the research is to understand fundamental processes in catalytic systems with applications to transportation technologies, such as those used for the treatment of NO_X emissions, and for the production of biomass-derived liquid fuels. The research heavily utilizes new capabilities and techniques for ultra-high resolution transmission electron microscopy with the HTML's aberration-corrected electron microscope (ACEM). The research is ultimately focused on understanding the effects of reaction conditions on the changes in morphology of heavy metal species on "real" catalyst support materials (e.g. oxides and carbon materials), and the understanding of the structures of model mono-, bi- and multi-metallic catalyst systems of known particle composition. A major thrust of these studies has been to develop methods of *in situ* microscopy at elevated temperatures and under controlled gas compositions. We have worked for some time with Protochips Inc. (Raleigh, NC), which provides a novel heating technology utilizing MEMS-based heating devices that we have shown to be stable enough to provide sub-Ångström imaging capabilities at high temperature in the ACEM. The devices have permitted the recent development of a closed-cell gas reaction holder that allows heating under controlled gas compositions up to a full atmosphere, with the ability to image atomic structure under these conditions. Methods using the new reactor (now called simply the "gas-cell holder") are currently being employed in a new study of "intelligent catalysts" for automotive emission control applications, based on the reported self-regenerative phenomenon of heavy metal species such as Pd and Rh in Ca- and La-based perovskite crystal structures. This work is being conducted in collaboration with Prof. Xiaoqing Pan of the University of Michigan, and his student Michael Katz and colleague George Graham, with further collaboration with Ford Research Laboratory colleague Dr. Andrew Drews.

Technical Progress

Gas-cell experiments in the present quarter involving work on the Daihatsu "intelligent catalyst" system with the University of Michigan/Ford Research collaborators was limited by a series of significant electronics problems on the JEOL ACEM, that led to instrument down-time for more than half of the time over the quarter. But we had the opportunity to begin developing the capability to do "flowing gas" experiments with the gas-cell holder, which is provided with a capillary tube system for return gas flow from the reaction cell out to a compression fitting on the handle of the holder. The critical problem with flowing gas through a tiny volume of the cell itself (1.55 mm^3) is to be able to control the total flow so that a reasonable number of gas changes per unit time are achieved. It is also necessary to provide a return reservoir that is as much lower pressure than the gas cell system, so flow will proceed from the cell to the reservoir. We therefore needed to modify the first generation gas handling manifold to allow

appropriate valving operations to be done, and a second 2.25 liter stainless-steel reservoir tank had to be installed to receive the return gas.

The gas in the generation 1 manifold assembly is fed to the microscope column through nominal 3/16" ID PE tubing, and it then runs to the cell through about 80 cm of 175 micron ID stainless steel tubing. This same diameter of tubing runs the length of the specimen rod on the return gas side of the cell, and for all of our early experiments that were run in a "static gas" mode, the return capillary was simply plugged at the exterior fitting on the handle of the rod. Figure 1 shows the system schematic for the static gas configuration of the manifold system.

Figure 2 shows the manifold schematic with the modifications to allow a return flow operation. Stainless steel capillary is added to connect the rod to the flange on the inside of the "clamshell" that surrounds the specimen rod when it is inside the column. Gas flow to the manifold returns through similar 3/16" ID PE tubing as on the supply side. At the manifold, we have provided a connection through a final tubing connection that is made to a length of PEEK tubing with a smaller internal diameter (we have diameters of 25 and 50 microns for initial trials), which will be fitted as appropriate, when we determine the primary geometries to control the flow at various pressures and with various gas compositions. Figure 2 also shows the additional valves and stainless steel tubing that has been added to the manifold, as well as the return gas cylinder, and a second MKS Baratron capacitance manometer vacuum gauge with a pressure range up to 1000 Torr. This additional gauge allows us now to control the pressure in the cell easily up to a full atmosphere (750 Torr), not previously possible because of the limited upper range of the first Baratron gauge we built in to the manifold.

The new capabilities for flowing gas through the gas-cell heating holder for the ACEM will allow us to add an extra dimension to our catalyst reaction experiments, especially since we can presumably more readily match the in situ microscopy experiments with catalyst reaction experiments done on bulk materials in bench-top reactors.

Status of Milestones

On schedule

Communications/Visits/Travel

Larry Allard has begun negotiations with colleagues at BASF Co., Iselin, NJ, to collaborate on new catalyst projects, ultimately involving ORNL's unique capabilities for *in situ* gas reaction studies at high resolution using the aberration-corrected JEOL electron microscope. Contacts are Dr. George Munsing, Dr. Weiling Wang, and Dr. Xiaofang Yang

Publications

"Novel MEMS-based Gas-Cell/Heating Specimen Holder Provides Advanced Imaging Capabilities for *In Situ* Reaction Studies," **L. F. Allard**, S. H. Overbury, W. C. Bigelow, M. B. Katz, D. P. Nackashi and J. Damiano; submitted to *Microscopy and Microanalysis*, Jan. 2012**.**

“Innovative Closed-Cell Reactor Permits *In Situ* Heating and Gas Reactions with Atomic Resolution at Atmospheric Pressure,” **L.F. Allard**, S.H. Overbury, M.B. Katz, W.C. Bigelow, D.P Nackashi and J. Damiano; 2-page abstract accepted for presentation at 2012 Microscopy Society of America meeting, Phoenix, AZ.

“Single-Atom Catalysis: Pt_1/FeO_x for CO Oxidation and Preferential Oxidation of CO in H_2,” B. Qiao, A. Wang, X. Yang, **L. F. Allard**, Z. Jiang, Y. Cui, J. Li,[2] T. Zhang[1] and J. Liu; 2-page abstract accepted for presentation at 2012 Microscopy Society of America meeting, Phoenix, AZ.

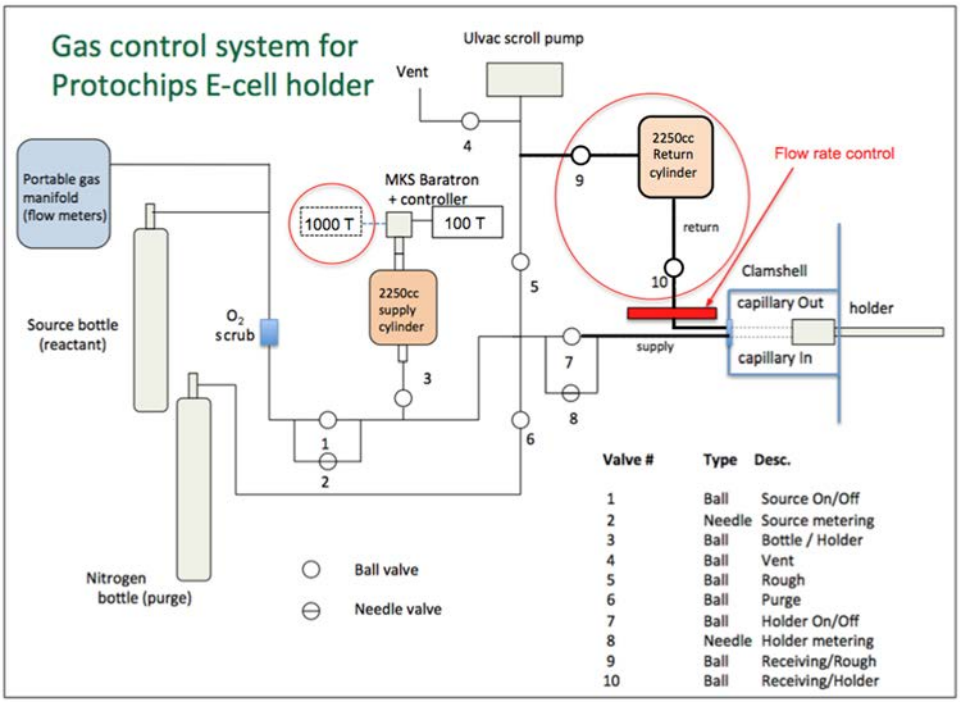

Fig. 1. Schematic of original gas-handling manifold for the Gen 3 Protochips gas-cell specimen holder. The manifold in this configuration supports only “static gas” reaction conditions.

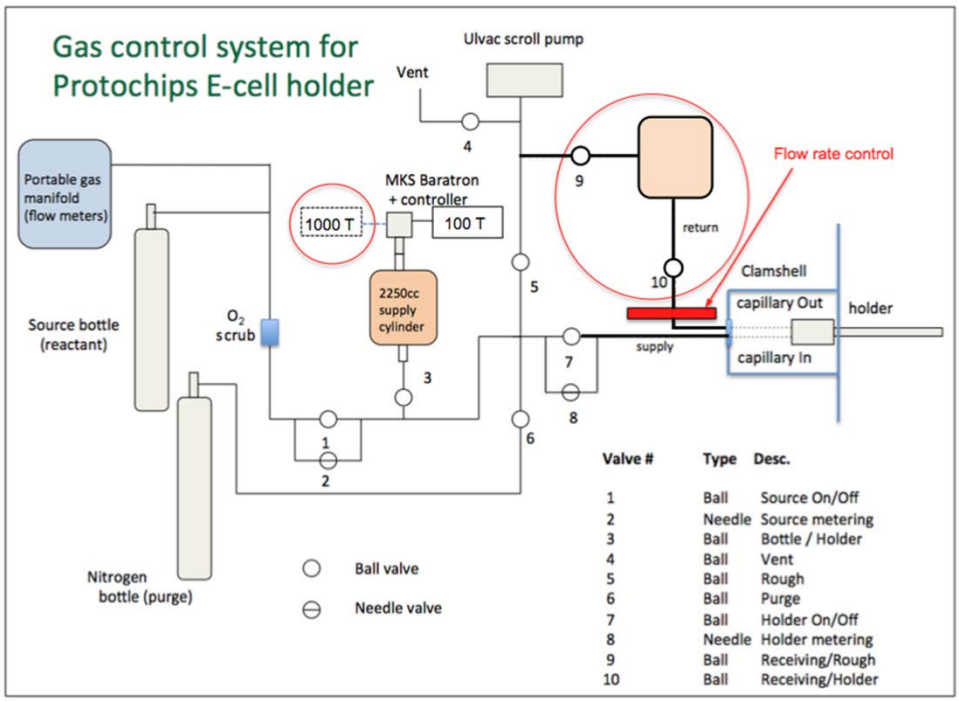

Fig. 2. Schematic of upgraded gas-handling manifold system, with additional valves to allow evacuation of a newly installed 2.25 liter “receiving tank,” and an additional Baratron capacitance manometer gauge to permit control of gas pressure in the “supply tank” up to 1000 Torr. The new configuration of the manifold allows “flowing gas” reactions to be conducted, for the first time.

Fig. 3. Views of the gas-handling manifold before (left) and after (right) modification to permit flowing gas reaction experiments in the Protochips gas-cell specimen holder.

Agreement 14957: High Temperature Thermoelectrics

A. A. Wereszczak and H. Wang
Oak Ridge National Laboratory
and
A. Thompson, R. McCarty, and J. Sharp
Marlow Industries, Inc.

Objective/Scope

Two-thirds of the chemical energy in automotive fuel is rejected to the atmosphere as waste heat. Thermomechanical stresses must be managed and TE material strength must be improved to fully exploit TE devices for waste heat recovery. Toward that, needed thermomechanical and thermophysical properties of candidate thermoelectric (TE) materials are measured in this project and then used with established probabilistic reliability and design models to optimally design automotive and heavy vehicle TE modules. Thermoelectric materials under candidacy for use in TE modules tend to be brittle, weak, and have a high coefficient of thermal expansion (CTE); therefore, they can be quite susceptible to mechanical failure when subjected to operational thermal gradients. A successfully designed TE module will be the result of the combination of temperature-dependent thermoelastic property and strength distribution data and the use of the method of probabilistic design developed for structural ceramics.

Technical Highlights

Mechanical Properties and Supportive Testing

Coefficient of thermal expansion testing of a candidate metallization layer was completed using (thin) stand-alone test coupons with high-temperature x-ray diffraction. Conventional dilatometry could not be used because the available material was too thin and had insufficient mechanical stiffness for use in the dilatometer's sample holder.

In preparation for greater emphasis on the evaluation of device reliability, an ultrasonic tester (scanning acoustic microscope) and a shear tester were installed during Q2 and training provided. Both are shown in Fig. 1 and will be used in FY12 to evaluate the metallization joints between device substrates and thermoelectric legs. Marlow is providing customized test coupons and their testing will occur in Q3.

Sintered bulk polycrystalline Si billets were processed using high purity silicon in a controlled environment. Their electrical resistivity, Seebeck coefficient, coefficient of thermal expansion, and thermal diffusivity were measured as a function of temperature. The room temperature thermal conductivity was estimated using thermal diffusivity data, density, and heat capacity and was less than 10 W/mK.

Figure 1. Ultrasonic (left) and shear testers (right) will be used to evaluate metallization joint strength.

Transport Property Measurements and IEA Activities

Thermal diffusivity of skutterudites prepared by melt-spin and hot pressing were evaluated. With new access to a Netzsch thermal diffusivity system and to an existing TA/Anter systems at ORNL, thermal diffusivity was measured using both systems to compare their results. An unusual up-turn in thermal diffusivity in the TA system led to more detailed investigation of the cause. Preliminary study showed the TA system could subject the samples to additional heating through electrical ground loops. This condition may only affect the test results on materials with large Seebeck coefficient, therefore its effect is not detectable when running standard references such as graphite and stainless steel.

Samples were prepared for a new round-robin effort in support of IEA-AMT Annex VIII on thermoelectric whose testing will cover the automobile exhaust temperature range from 20-500°C. The initial materials, n-type PbTe, were provided by ZT-PLUS. Testing samples were machined at ORNL and Marlow Industries. The difficulty to machine small disk samples (4 mm in diameter) for specific heat testing, has led the annex to switch to a new material made by GMZ. The materials will be circulated to the round-robin participants in Q3-Q4 of FY12.

<u>Status of FY 2012 Milestones</u>

1. Measure mechanical, thermoelastic, and thermoelectric properties of Marlow-fabricated TE materials to enable reliable operation up to 500°C. [Sep12] *On schedule.*
2. Process and engineer sintered bulk polycrystalline Si to reduce its thermal conductivity to less than 10 W/mK. [Sep12] *Completed.*
3. Complete report of international round-robin test results on Marlow bismuth telluride to IEA-AMT and initiate a new high temperature thermoelectric round-robin measurements on PbTe or skutterudite ranging between 20-500°C. *On schedule.*

Communications/Visits/Travel:
Wang attended the Third Thermoelectric Application Workshop, Baltimore, MD, March 20-22, 2012. Wang gave a presentation, was a co-author on another, and chaired a technical session.

Problems Encountered:
A one-year extension for the CRADA between ORNL and Marlow has encountered several administrative delays; however, its full authorization should occur in early Q3.

Publications/Presentations/Awards:
H. Wang, et al., "International Round-robin on Transport Properties of Bismuth Telluride", Third Thermoelectric Application Workshop, Baltimore, MD, March 20-22, 2012.

J. R. Salvador, et al., H. Wang, and A. A. Wereszczak, "Exploration of Melt Spinning as a Route to Large Volume Production of Skutterudite Thermoelectric Materials," Third Thermoelectric Application Workshop, Baltimore, MD, March 20-22, 2012.

References
None

Agreement 16308: MBD Thermoelectrics Theory and Structure

David J. Singh
Oak Ridge National Laboratory

Objective/Scope

We will use modern science based materials design strategies to find ways to optimize existing thermoelectric materials and to discover new families of high performance thermoelectrics for waste heat recovery and vehicular cooling applications in vehicles. The emphasis will be on the thermoelectric figure of merit at temperatures relevant to waste heat recovery and vehicular cooling and on other properties important for applications, especially anisotropy, cost and mechanical properties.

Technical Highlights

Vehicular applications of thermoelectric materials for waste heat recovery, as well as room-temperature passenger cooling (necessary for the performance of hybrid electric vehicles) depend on the identification of high performance practical materials. These materials must have the contradictory properties of good electrical conductivity and high Seebeck coefficient, and low thermal conductivity but high electrical conductivity. In an attempt to find materials with such properties, we have been guided by recent work, where it was found that a mixture of light and heavy bands (active in the transport) yields favorable thermoelectric performance. We found that the tetragonal chalcopyrite structure $AgGaTe_2$ (see figure at left), which has already shown a ZT of 0.9 at high temperature with only minimal optimization, may show excellent thermoelectric performance (ZT substantially larger than 1) at high temperatures, and that this transport would be essentially isotropic, a substantial advantage for applications. While this material is not likely to be used in widespread applications due to the high element cost, it is representative of a larger class of chalcopyrite structure materials (see Figure 3) which all can be expected to have favorable thermoelectric properties if their lattice thermal conductivity can be reduced by alloying, or by the type of “bulk” nano[-structuring described in our recent publication on hole-doped Bi_2Se_3 [2].

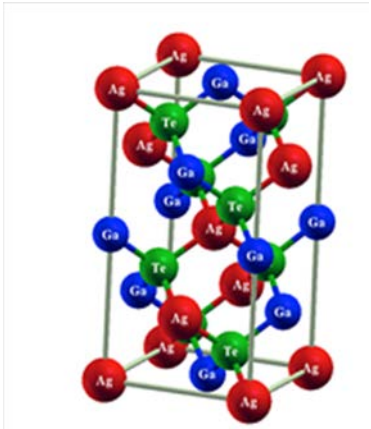

Figure 1. The chalcopyrite crystal structure of $AgGaTe_2$, which is the same as that of $ZnSiAs_2$.

These conclusions are based on detailed technical analyses (performed using the first principles electronic structure and the in-house developed transport code BoltzTrap [3]) of the thermoelectric performance of $AgGaTe_2$ and related chalcopyrite structure materials.

In this context the insight that our first principles calculations provide, namely at what temperatures and dopings optimal performance may be found, is expected to be most helpful to experimental groups attempting to optimize this material. Presented in Figure 2 is a plot of the Seebeck coefficient for $AgGaTe_2$ at the temperatures of 700 and 900 K where performance is expected to be optimal (note that these temperatures are at the upper end of waste heat recovery operating temperatures). At the comparatively heavy doping of 10^{20} cm^{-3} both the 700 and 900 K Seebeck coefficients are above 200 μV/K, a value compatible with excellent thermoelectric performance (note also the near isotropic nature of the thermopower). We identified the optimal doping ranges for this material to be between 2 x 10^{19} and 10^{20} cm^{-3} at 700 K and between 4 x 10^{19} and 2 x 10^{20} cm-3, and look forward to experimental efforts to dope this material appropriately.

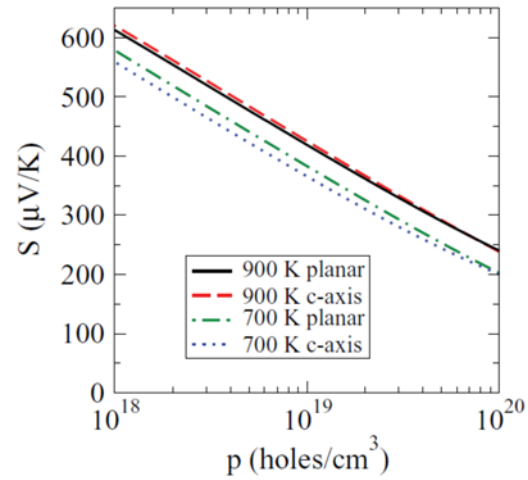

Figure 2. Calculated thermopower of hole doped $AgGaTe_2$ at temperatures of 700 K and 900 K.

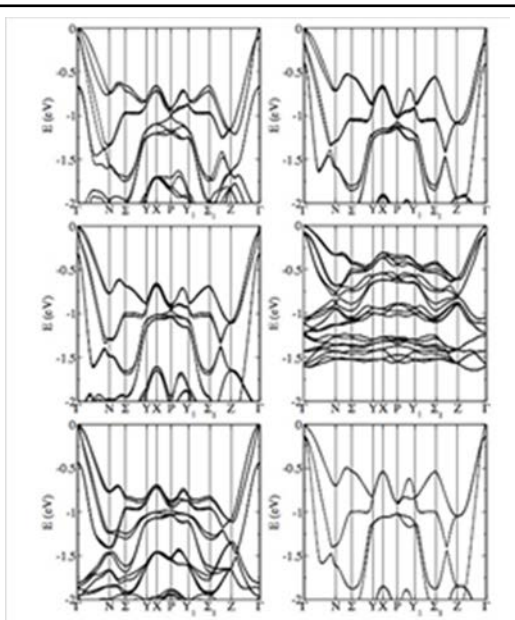

Figure 3. Calculated electronic band structures of (clockwise from top left) $AgGaTe_2$, $CdGeAs_2$, $CuInS_2$, $ZnSiAs_2$, $CuInTe_2$ and $CdSnAs_2$ as obtained by the general potential linearized augmented planewave method.

As mentioned, we used electronic structure calculations to screen related materials and thereby identified a number of other chalcopyrite structure semiconductors with very similar electronic structures to that of $AgGaTe_2$, in particular the mixture of heavy and light bands. This is important to address cost and practicality barriers for vehicular use. In Figure 3 we depict the calculated band structure, within the tetragonal Brillouin zone, of six of these materials (including $AgGaTe_2$, top left). Most of these materials form as p-type semiconductors, and to the extent that the dispersive energy scales of the top valence bands of these materials are similar to those of $AgGaTe_2$, they should show similarly large Seebeck coefficients. For this class of materials the ultimate performance will depend on what degree of thermal conductivity reduction can be achieved through the aforementioned alloying and bulk nanostructuring techniques. Importantly, one of the materials that this screen

identified as promising is $ZnSiAs_2$, which is a low cost material that does not include the undesirable element Pb.

Status of FY 2012 Milestones

We are making progress towards our milestone of successfully predicting new thermoelectric compositions. We plan to explore the potential thermoelectric performance of the kesterite materials $Cu_2ZnSnSe_4$ and Cu_2ZnSnS_4, both composed of inexpensive and abundant elements, as well as the zinc antimonide ZnSb.

Problems Encountered

No significant problems encountered this quarter.

Publications/Presentations/Awards

1. D. Parker and D.J. Singh, "Thermoelectric properties of $AgGaTe_2$ and related chalcopyrite structure materials", Phys. Rev. B **85**, 125209 (2012).
2. D. Parker and D.J. Singh, "Very heavily electron-doped CrSi2 as a high-performance high-temperature thermoelectric material", New Journal of Physics **14**, 033045 (2012)."
3. D. Parker, "Thermoelectric Materials for Automotive Applications", invited talk at the Thermoelectric Applications Workshop, Baltimore MD, March 21, 2012.
4. D.J. Singh, "Transport in Old and New Thermoelectric Materials", invited talk, American Physical Society March Meeting, Boston, MA February 28, 2012.
5. D. Parker, "Potential Thermoelectric Performance from Optimization of Hole-Doped Bi_2Se_3", contributed talk, American Physical Society March Meeting, Boston, MA February 28, 2012.

References:

1. A.F. May, D.J. Singh and G.J. Snyder, "Effect of Band Structure on the Large Thermoelectric Performance of Lanthanum Telluride", Phys. Rev. B **79**, 153101 (2009).
2. D. Parker and D.J. Singh, "Potential thermoelectric performance from optimization of hole-doped Bi_2Se_3", Phys. Rev. X **1**, 021005 (2011).
3. G.K.H Madsen and D.J. Singh, "BoltzTraP: a code for calculating band-structure dependent quantities", Computer Physics Commun. **175**, 67 (2006).